

AD-A159 458

INCLUSION EFFECTS ON STRESS GAGE MEASUREMENTS IN ROCK  
AND SOIL(U) SRI INTERNATIONAL MENLO PARK CA  
A L FLORENCE ET AL. 01 MAY 84 DNR-TR-84-210

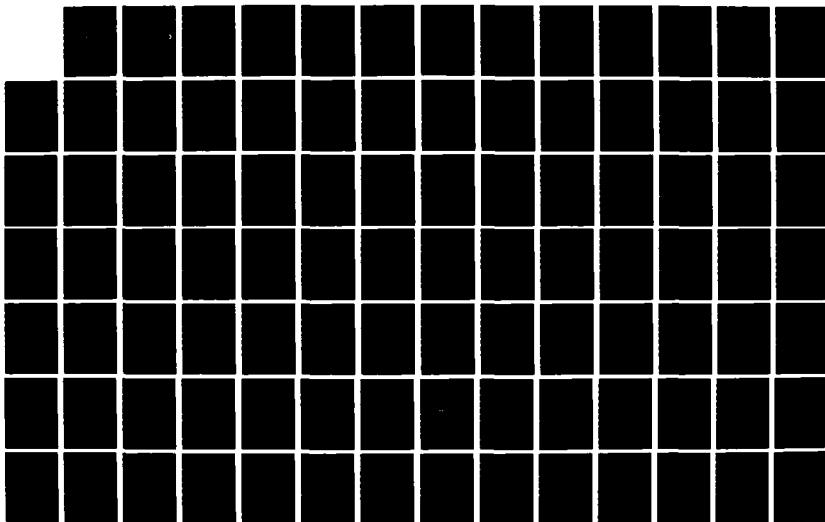
1/2

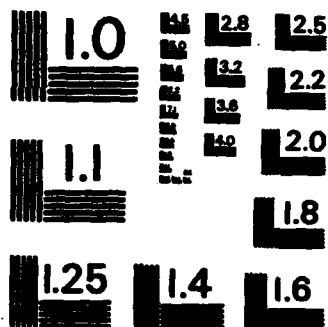
UNCLASSIFIED

DNR001-83-C-0279

F/G 8/7

NL





MICROCOPY RESOLUTION TEST CHART  
NATIONAL BUREAU OF STANDARDS-1963-A

AD-A159 458

DNA-TR-84-210

# INCLUSION EFFECTS ON STRESS GAGE MEASUREMENTS IN ROCK AND SOIL

A.L. Florence  
T. Cooper  
D.D. Keough

L.E. Schwer  
J.T. Rosenberg

SRI INTERNATIONAL  
333 Ravenswood Avenue  
Menlo Park, CA 94025-3434

1 May 1984

Technical Report

DTIC  
ELECTE  
OCT 1 1985  
S D  
B

CONTRACT No. DNA 001-83-C-0279

APPROVED FOR PUBLIC RELEASE;  
DISTRIBUTION IS UNLIMITED.

THIS WORK WAS SPONSORED BY THE DEFENSE NUCLEAR AGENCY  
UNDER RDT&E RMSS CODE B345083466 J11AMXJI00032 H2590D.

Prepared for  
Director  
DEFENSE NUCLEAR AGENCY  
Washington, DC 20305-1000

85 8 9 078

DTIC FILE COPY

Destroy this report when it is no longer needed. Do not return to sender.

PLEASE NOTIFY THE DEFENSE NUCLEAR AGENCY,  
ATTN: STTI, WASHINGTON, DC 20306-1000, IF YOUR  
ADDRESS IS INCORRECT, IF YOU WISH IT DELETED  
FROM THE DISTRIBUTION LIST, OR IF THE ADDRESSEE  
IS NO LONGER EMPLOYED BY YOUR ORGANIZATION.



UNCLASSIFIED

SECURITY CLASSIFICATION OF THIS PAGE

AD-A157458

## REPORT DOCUMENTATION PAGE

1a. REPORT SECURITY CLASSIFICATION UNCLASSIFIED		1b. RESTRICTIVE MARKINGS	
2a. SECURITY CLASSIFICATION AUTHORITY		3. DISTRIBUTION/AVAILABILITY OF REPORT Approved for public release; distribution is unlimited.	
2b. DECLASSIFICATION/DOWNGRADING SCHEDULE N/A since UNCLASSIFIED			
4. PERFORMING ORGANIZATION REPORT NUMBER(S) SRI PYU-5877		5. MONITORING ORGANIZATION REPORT NUMBER(S) DNA-TR-84-210	
6a. NAME OF PERFORMING ORGANIZATION SRI International	6b. OFFICE SYMBOL (If applicable)	7a. NAME OF MONITORING ORGANIZATION Defense Nuclear Agency	
6c. ADDRESS (City, State and ZIP Code) 333 Ravenswood Avenue Menlo Park, CA 94025-3434		7b. ADDRESS (City, State and ZIP Code) Washington, D.C. 20305-1000	
8a. NAME OF FUNDING/SPONSORING ORGANIZATION	8b. OFFICE SYMBOL (If applicable)	8. PROCUREMENT INSTRUMENT IDENTIFICATION NUMBER DNA 001-83-C-0279	
8c. ADDRESS (City, State and ZIP Code)		10. SOURCE OF FUNDING NOS.	
		PROGRAM ELEMENT NO. 62175H	PROJECT NO. J11AMXJ
		TASK NO. I	WORK UNIT NO. DH007050
11. TITLE (Include Security Classification) INCLUSION EFFECTS ON STRESS GAGE MEASUREMENTS IN ROCK AND SOIL			
12. PERSONAL AUTHOR(S) A. L. Florence, L. E. Schwer, T. Cooper, J. T. Rosenberg, and D. D. Keough			
13a. TYPE OF REPORT Technical Report	13b. TIME COVERED FROM 830427 TO 840426	14. DATE OF REPORT (Yr., Mo., Day) 1984 May 01	15. PAGE COUNT 118
16. SUPPLEMENTARY NOTATION This work was sponsored by the Defense Nuclear Agency under RDT&E RMSS Code B345083466 J11AMXJI00032 H2590D			
17. COSATI CODES		18. SUBJECT TERMS (Continue on reverse if necessary and identify by block number)	
FIELD 8	GROUP 7	Stress Gage Rock Stress Waves	
20	11	Inclusion Tuff Ytterbium	
		Borehole Grout Piezoresistance	
19. ABSTRACT (Continue on reverse if necessary and identify by block number)  One of the main difficulties in measuring stress in rocks and soils is that the stress gage and installation disturb the stress field to be measured. Another difficulty is to relate the behavior of a sensing foil embedded within a stress gage package to the stress field surrounding the gage.  The work reported is the first phase of a combined theoretical and experimental program to investigate problems of in-situ stress measurement.  Finite element calculations were performed on a grout-filled borehole in tuff to show how the relationship between the free-field and gage plane stresses are influenced by mismatch of fill and medium properties, load level, and slip and separation along the interface. Calculations also show the formation of a residual stress field in the borehole fill.			
20. DISTRIBUTION/AVAILABILITY OF ABSTRACT UNCLASSIFIED/UNLIMITED <input checked="" type="checkbox"/> SAME AS RPT. <input type="checkbox"/> DTIC USERS <input type="checkbox"/>		21. ABSTRACT SECURITY CLASSIFICATION UNCLASSIFIED	
22a. NAME OF RESPONSIBLE INDIVIDUAL Betty L. Fox		22b. TELEPHONE NUMBER (Include Area Code) 202-325-7042	22c. OFFICE SYMBOL DNA/STTI

DD FORM 1473, 83 APR

EDITION OF 1 JAN 73 IS OBSOLETE.

UNCLASSIFIED

SECURITY CLASSIFICATION OF THIS PAGE

UNCLASSIFIED

SECURITY CLASSIFICATION OF THIS PAGE

19. ABSTRACT (Continued)

Similar calculations were performed on a typical flatpack stress gage design to relate the free-field stresses, the stresses on the package, and the stresses acting on the plane of the piezoresistive sensing foil.

Finite difference calculations were performed to obtain the response to shock loading of an ytterbium sensing foil embedded in PMMA. This work is part of a coordinated research effort with other DMA contractors on piezoresistive/mechanical properties of ytterbium appropriate to stress measurement environments.

A triaxial static experiment was designed and constructed for future investigations on borehole fill inclusions, including comparisons with theoretical predictions.

A 2-foot-diameter flyer plate experiment was designed for future application to dynamic loading and unloading of stress gage package in a known environment.

Accession For	
NTIS GRA&I	<input checked="checked" type="checkbox"/>
DTIC TAB	<input type="checkbox"/>
Unannounced	<input type="checkbox"/>
Justification	
By	
Distribution/	
Availability Codes	
Dist	Avail and/or Special
A-1	



UNCLASSIFIED

SECURITY CLASSIFICATION OF THIS PAGE

## SUMMARY

The measurement of in-situ stress is important to many DNA ground motion and structures programs. Recent results from field tests have shown that long duration, reproducible records can be obtained with armored gages over a very large range of stress and in severe mechanical and EM environments. However, reduction of the records to stress data requires that the relationship between free-field stress and stress in the gage and its immediate surroundings (borehole) be established for the variety of geologic materials, borehole fillers, and stress ranges encountered in DNA field tests. Although such relationships have been investigated both analytically and experimentally for elastic response of materials, the elastic-plastic and plastic response regimes have received little, if any, attention. These regimes are of particular importance in DNA programs because the yield behavior of in-situ geologic materials subjected to particular strain paths is largely unknown and is difficult to determine in the laboratory. Recent advances in finite difference and finite element calculational simulations have provided new tools for investigating the required stress relationships.

SRI is conducting a theoretical, calculational, and experimental program to determine the relationships between inclusion (gage, borehole) stress and free-field (medium) stress for materials, geometries, and stress ranges encountered in in-situ measurement programs and to provide criteria for gage design and installation. The program consists of two complementary efforts: (1) finite element calculations with supporting analytical computations and static triaxial compression experiments, and (2) finite difference calculations with supporting shock wave experiments to examine dynamic effects. In the first effort, we are addressing conditions encountered when stresses of wavelengths that are large compared with inclusion dimensions are to be measured,

and in the second, we are addressing stresses of wavelength comparable to the inclusion dimension.

We have performed preliminary biaxial plane strain, finite element calculations to determine the stress distribution normal to gage planes in a borehole, in tuff, filled with a matching grout and loaded proportionally. We have investigated the effect of material property mismatch, grout-tuff bonding (including separation), and unloading (residual stress) on stress distribution and ratio of borehole stress to free-field stress. The preliminary calculations were restricted to elastic free-field loading, but they allowed plastic behavior in the inclusion and in the medium next to the inclusion. These results indicated that:

- (1) The distribution of stresses normal to the radial and tangential stress measurement planes in the borehole is nonuniform. The nonuniformity is a strong function of applied load and interface bonding.
- (2) Over the central portion of the radial measuring plane (50% of borehole diameter), the distribution is uniform within  $\pm 10\%$  for bonded, frictional, and unbonded interfaces, but the ratio of borehole stress to free-field stress is closer to unity for bonded and frictional interfaces.
- (3) The stress distributions on the tangential measuring plane were more uniform for the bonded interface; however, the stress ratio depended on the free-field stress amplitude.
- (4) Separation at the interface caused nonuniform stress distributions similar to those caused by slip.
- (5) Residual stress remained in the borehole after unloading of the free-field stress. The magnitude and distributions were dependent on the boundary conditions, matching of properties, and orientation of the measurement plane. The least residual stress and most uniform distribution occurred for the radial measurement plane and frictional boundary. The bonded boundary produced large residual stress and large variations in distribution if the properties were not well matched; therefore, the bonded boundary was best for loading but poor upon unloading if the properties are not well matched.



We have also performed elastic analyses of stresses in elliptic and circular inclusions under plane strain loading to validate the finite element code and facilitate parametric investigations in the elastic regime. The analyses addressed a bonded general ellipse, a bonded slender ellipse, a bonded and unbonded circle, circular interface separation, a rigid line inclusion, and residual stress in a bonded circle. Of particular interest is the result of the rigid line inclusion, which showed that the line (gage) should not be bonded to the medium.

A finite element analysis was made of a typical flatpack stress gage embedded in grout. Results showed that the thin sensing element was subjected to the free-field stress if the element occupied less than 60% of the central midplane of the plastic within the steel armor.

We designed and constructed a static loader for subjecting borehole inclusions in 10 x 10 x 22 inch samples to triaxial loads with a maximum stress difference of  $\sim 1/2$  kbar at a hydrostatic pressure of  $\sim 1$  kbar. Sensors for these experiments have been examined for suitability (minimizing inclusion effects and monitoring interface behavior).

We also performed a numerical simulation of the dynamic (shock) loading of an ytterbium foil in PMMA (experiments conducted by Y. M. Gupta at Washington State University). The simulation generated the stress and strain states in the foil during the load/unload process. The results indicated that:

- (1) The material models used for PMMA and ytterbium and the piezoresistance formulation of Gupta led to a resistance change versus axial stress profile in fair agreement with Gupta's experiment that measured the rising and peak stress portions of the loading.
- (2) Separation between foil and PMMA on unloading resulted from the geometry of the foil and material model (yielding) of PMMA. A change in foil geometry on separation produced a residual resistance in the foil.
- (3) The calculational method of determining the scalar resistance change in the deformed foil should be examined further.

- (4) Additional comparisons should be made between calculated and measured response at other stresses because adjustments in plastic work terms in the piezoresistance formulation were required to obtain quantitative agreement between measured and calculated responses.

Finally, we examined the feasibility of using the 4-inch-diameter gas gun and reduced-scale flatpack gages to investigate the relationship between a known free-field stress history and gage stress history. The latter was examined by performing one-dimensional calculational simulations of a gage in PMMA. Results indicated that gage-medium equilibrium could be obtained during loading durations achievable in the 4-inch-diameter gun only if the steel armor of the gage were reduced to very thin foils. Because this reduction would alter gage response, it was concluded that longer duration pulses than are achievable in the 4-inch-diameter gun would be required. This conclusion evoked the idea of a 2-ft-diameter flyer plate for the dynamic experiments. The design of this facility is presented in this report.

## PREFACE

This research was conducted under Contract DNA001-83-C-0279 in support of the DNA stress measurement program. The technical monitor of the research was Michael J. Frankel.

The authors are indebted to the personnel at SRI International who contributed directly to the research program. In particular, appreciation is extended to G. Nagy for supervising the proof-testing of the static loader, to Y. Murray for design calculation on the flyer plate facility, to R. W. Blumenkamp for interface gage development, to K. Stepleton for miniature stress gage development, and to G. R. Greenfield, G. S. Cartwright, and T. S. Lovelace for invaluable technical support.

Conversion factors for U.S. customary  
to metric (SI) units of measurement.

To Convert From	To	Multiply By
angstrom	meters (m)	1.000 000 X E -10
atmosphere (normal)	kilo pascal (kPa)	1.013 25 X E +2
bar	kilo pascal (kPa)	1.000 000 X E +2
barn	meter <sup>2</sup> (m <sup>2</sup> )	1.000 000 X E -28
British thermal unit (thermochemical)	joule (J)	1.054 350 X E +3
cal (thermochemical)/cm <sup>2</sup> §	mega joule/m <sup>2</sup> (MJ/m <sup>2</sup> )	4.184 000 X E -2
calorie (thermochemical)§	joule (J)	4.184 000
calorie (thermochemical)/g§	joule per kilogram (J/kg)*	4.184 000 X E +3
curies	giga becquerel (GBq)†	3.700 000 X E +1
degree Celsius‡	degree kelvin (K)	$t_K = t_C + 273.15$
degree (angle)	radian (rad)	1.745 329 X E -2
degree Fahrenheit	degree kelvin (K)	$t_K = (t_F + 459.67)/1.8$
electron volt§	joule (J)	1.602 19 X E -19
erg§	joule (J)	1.000 000 X E -7
erg/second	watt (W)	1.000 000 X E -7
foot	meter (m)	3.048 000 X E -1
foot-pound-force	joule (J)	1.355 818
gallon (U.S. liquid)	meter <sup>3</sup> (m <sup>3</sup> )	3.785 412 X E -3
inch	meter (m)	2.540 000 X E -2
jerk	joule (J)	1.000 000 X E +9
joule/kilogram (J/kg) (radiation dose absorbed)§	gray (Gy)*	1.000 000
kilotons§	terajoules	4.183
kip (1000 lbf)	newton (N)	4.448 222 X E +3
kip/inch <sup>2</sup> (ksi)	kilo pascal (kPa)	6.894 757 X E +3
ktap	newton-second/m <sup>2</sup> (N-s/m <sup>2</sup> )	1.000 000 X E +2
micron	meter (m)	1.000 000 X E -6
mil	meter (m)	2.540 000 X E -5
mile (international)	meter (m)	1.609 344 X E +3
ounce	kilogram (kg)	2.834 952 X E -2
pound-force (lbf avoirdupois)	newton (N)	4.448 222
pound-force inch	newton-meter (N-m)	1.129 848 X E -1
pound-force/inch	newton/meter (N/m)	1.751 268 X E +2
pound-force/foot <sup>2</sup>	kilo pascal (kPa)	4.788 026 X E -2
pound-force/inch <sup>2</sup> (psi)	kilo pascal (kPa)	6.894 757
pound-mass (lbm avoirdupois)	kilogram (kg)	4.535 924 X E -1
pound-mass-foot <sup>2</sup> (moment of inertia)	kilogram-meter <sup>2</sup> (kg-m <sup>2</sup> )	4.214 011 X E -2
pound-mass/foot <sup>3</sup>	kilogram-meter <sup>3</sup> (kg-m <sup>3</sup> )	1.601 846 X E +1
rad (radiation dose absorbed)§	gray (Gy)*	1.000 000 X E -2
roentgen§	coulomb/kilogram (C/kg)	2.579 760 X E -4
shake	second (s)	1.000 000 X E -8
slug	kilogram (kg)	1.459 390 X E +1
torr (mm Hg, 0° C)	kilo pascal (kPa)	1.333 22 X E -1

\*The gray (Gy) is the accepted SI unit equivalent to the energy imparted by ionizing radiation to a mass of energy corresponding to one joule/kilogram.

†The becquerel (Bq) is the SI unit of radioactivity; 1 Bq = 1 event/s.

‡Temperature may be reported in degree Celsius as well as degree kelvin.

§These units should not be converted in DNA technical reports; however, a parenthetical conversion is permitted at the author's discretion.

## CONTENTS

<b>SUMMARY .....</b>	<b>1</b>
<b>PREFACE .....</b>	<b>5</b>
<b>CONVERSION FACTORS .....</b>	<b>6</b>
<b>LIST OF ILLUSTRATIONS .....</b>	<b>9</b>
<b>1. INTRODUCTION AND PROGRAM .....</b>	<b>13</b>
1.1 Introduction .....	13
1.2 Program .....	15
Theoretical Investigations .....	15
Experimental Investigations .....	16
<b>2. STATIC CALCULATIONS FOR FILLED BOREHOLE INCLUSIONS .....</b>	<b>18</b>
2.1 Introduction .....	18
2.2 Interface Conditions .....	24
2.3 Material Properties .....	27
2.4 Interface Conditions and Material Properties .....	29
2.5 Unloading and Residual Stress .....	32
Effect of Interface Conditions on Residual Stress .....	34
2.6 Interface Separation .....	37
Interface Separation Formulation .....	37
Stress Distributions .....	39
<b>3. STATIC ANALYSIS OF INCLUSIONS .....</b>	<b>41</b>
3.1 Introduction .....	41
3.2 Bonded Elliptic Inclusions .....	42
3.3 Bonded Slender Elliptic Inclusion .....	44
3.4 Bonded Circular Inclusion .....	46
3.5 Unbonded Circular Inclusion .....	48
3.6 Separation at the Interface .....	52
3.7 Residual Stress in a Bonded Circular Inclusion .....	55
<b>4. STATIC CALCULATIONS OF STRESS GAGE INCLUSIONS .....</b>	<b>62</b>

4.1	Introduction .....	62
4.2	Flatpack Stress Gage Inclusion .....	62
4.3	Line Inclusion .....	65
5.	NUMERICAL SIMULATION OF THE DYNAMIC RESPONSE OF A FOIL INCLUSION .....	68
5.1	Introduction .....	68
5.2	Material Models .....	72
5.3	Results .....	75
5.4	Discussion .....	80
5.5	Conclusions .....	83
6.	EXPERIMENTAL INVESTIGATIONS .....	84
6.1	Introduction .....	84
6.2	Static Experiments .....	85
6.3	Gage Development for Laboratory Experiments .....	85
	Miniature Stress Gage .....	87
	Interface Gage .....	90
6.4	Long-Duration Plane Wave Experiment .....	90
	Flyer Plate/Target Characteristics .....	92
	Launcher Dynamics .....	94
	Structural Design .....	97
	Overall Piston-Target Impact .....	99
	Characteristics of Various Flyer Plate Materials .....	100
	REFERENCES .....	102
	APPENDIX: COMPARISON OF RESISTANCE AVERAGING WITH MECHANICAL AVERAGING FOR CALCULATING THE RESISTANCE CHANGE OF A PIEZORESISTANCE FOIL IN PLANE STRAIN .....	103

# LIST OF ILLUSTRATIONS

<u>Figure</u>		<u>Page</u>
1	In-Situ Stress Gage Emplacement .....	14
2	Circular Inclusion Under Biaxial Stress and Plane Strain .....	19
3	Gage Locations in Borehole .....	21
4	Finite Element Grid .....	22
5	Stress Along Gage Planes for Tuff Inclusion with Slip Interface .....	25
6	Stress Along Gage Planes for Tuff Inclusion with Frictional Interface $\mu = 0.6$ .....	26
7	Stress Along Gage Planes for Grout Inclusion with Bonded Interface .....	28
8	Stress Along Gage Planes for Grout Inclusion with Slip Interface .....	30
9	Stress Along Gage Planes for Grout Inclusion with Frictional Interface $\mu = 0.6$ .....	31
10	Stress Trajectories in a Bonded Grout Inclusion for Von Mises and Tresca Yield Criteria .....	33
11	Residual Stress Along Gage Planes with Tuff Inclusion .....	35
12	Residual Stress Along Gage Planes with Grout Inclusion .....	36
13	Contact/Separation of a Smooth Disk in an Infinite Plate, Analytical and Computational Solutions .....	38
14	Stress Along the Gage Planes for the Uniaxial Compression of a Smooth Elastic Disk in an Infinite Plate .....	40
15	Elliptic Inclusion Under Biaxial Stress .....	43

# LIST OF ILLUSTRATIONS (Continued)

<u>Figure</u>		<u>Page</u>
16	Stress in a Bonded Slender Elliptic Inclusion ( $v_1 = v_2 = 0.3$ ; $\epsilon = 0.1$ ) .....	45
17	Pressure in a Slender Elliptic Fluid Inclusion ( $\epsilon = 0.1$ ) .....	47
18	Stress in a Bonded Circular Inclusion ( $v_1 = v_2 = 0.3$ ) .....	49
19	Stress in an Unbonded Circular Inclusion ( $v_1 = v_2 = 0.3$ ; $\kappa = 0$ ) .....	51
20	Stress in Unbonded 2C4 Grout Circular Inclusion in Tuff (Properties in Table 1; $\mu_1/\mu_2 = 1.63$ ) .....	53
21	Stresses in Bonded and Unbonded Circular Inclusions of 2C4 Grout in Tuff (Properties in Table 1; $\mu_1/\mu_2 = 1.63$ ) .....	54
22a	Unbonded Circular Inclusion Separation Conditions at $\theta = 0^\circ$ ( $v_1 = v_2 = 0.3$ ) .....	56
22b	Unbonded Circular Inclusion Separation Conditions at $\theta = 90^\circ$ ( $v_1 = v_2 = 0.3$ ) .....	57
22c	Bonded Circular Inclusion Separation Conditions at $\theta = 0^\circ$ ( $v_1 = v_2 = 0.3$ ) .....	58
22d	Bonded Circular Inclusion Separation Conditions at $\theta = 90^\circ$ ( $v_1 = v_2 = 0.3$ ) .....	59
23	The Flatpack Stress Gage .....	63
24	Stress Along the Gage Plane for a Gage Package Bonded in a Grout Media .....	64
25	Line Idealization of Flatpack Stress Gage .....	66
26	PMMA Matrix and Blow-Ups Showing the Gage Positions .....	69
27	Ytterbium Gage Foil .....	70
28	Area Modeled in the Computation .....	71
29	Mesh in the Neighborhood of the Foil .....	73



# **LIST OF ILLUSTRATIONS (Concluded)**

<u>Figure</u>		<u>Page</u>
30	Material Boundaries (left) and Mesh (right) Around the Foil at 3.38 $\mu$ s .....	76
31	Relative Resistance Change for the Foil Versus Time .....	78
32	Z Stress Versus Time .....	79
33	Plastic Strain Versus Time .....	81
34	Density Versus Time .....	82
35	Inclusion Apparatus .....	86
36	Loading and Unloading of Piezoresistive Ytterbium Under Various Conditions .....	89
37	Large Flyer Plate Experiment .....	95
A1	Piezoresistant Foil Configurations .....	104
A2	Uniaxial Strain Two-Cell Test Problem .....	108

## SECTION 1

### INTRODUCTION AND PROGRAM

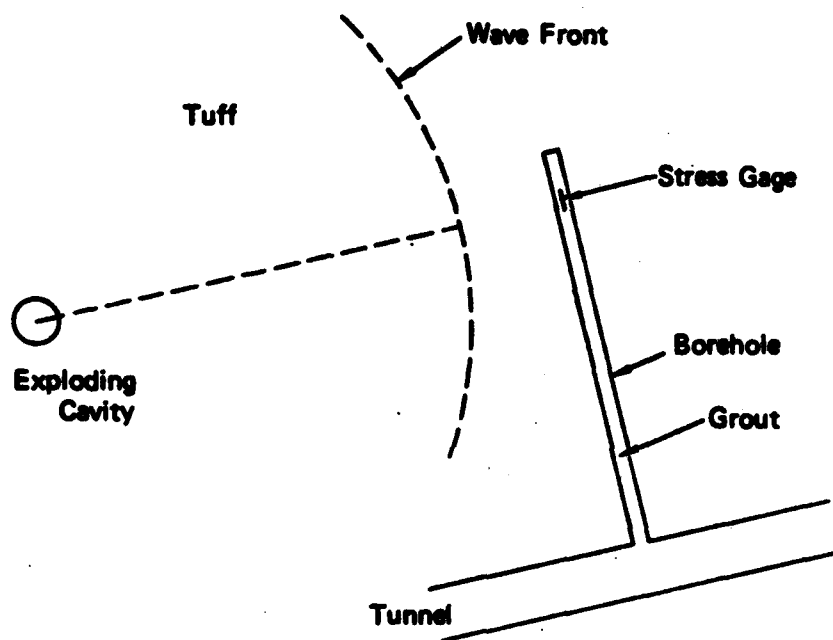
#### 1.1 INTRODUCTION

An important sensor in Department of Defense research and development field experiments is the piezoresistant stress gage. The gage is used to measure the stress waves in rocks and soils resulting from underground nuclear explosions and from high explosive systems that simulate shock and blast effects from surface and aboveground nuclear explosions.

One of the difficulties in measuring stresses in-situ is that the gage package and its immediate surroundings perturb the free field. The gage package may be regarded as an inclusion in a geologic medium. In many cases, the installation procedure introduces an additional inclusion. For example, gages are installed in Nevada Test Site (NTS) tuff by drilling from a tunnel, inserting the gage, and packing the borehole with a rock-matching grout, as illustrated in Figure 1. Because it is impossible to match all the properties of the tuff in the neighborhood of the gage and to ensure perfect bonding with the tuff, the grout forms a cylindrical inclusion. Thus, the gage is in general not subjected to the same stresses as the free-field stresses, and we must determine the relationship between the grout inclusion and geologic medium stress fields.

Our coordinated theoretical and experimental program to investigate the inclusion effects of gages and their installation is described below. This program is regarded as one phase of the overall program on in-situ stress measurement.<sup>1</sup> The overall objective is to guide the development of gage design and installation procedures to ensure that the gage records are useful approximations of the free-field stresses.

The approach is first to perform calculations on current stress gage design concepts and on installation configurations to identify the



JA-317832-8

Figure 1. In-situ stress gage emplacement.

influential parameters with a view to optimizing the stress measurement technique or establishing its limitations. Second, simple static and dynamic experiments are performed to validate predictions and to assist technique development.

## 1.2 PROGRAM

The initial phase of our overall program on in-situ stress measurements consists of the following: (1) finite element code calculations on stress gage inclusions and borehole inclusions, (2) classical analyses of these inclusions at low stresses, (3) finite difference code calculations on the response of an ytterbium sensing element to a planar shock wave, (4) static experiments on gages and boreholes, and (5) a study of experimental designs for providing dynamic loading of stress gages and boreholes. A description of the theoretical and experimental portions of the program follows.

### Theoretical Investigations

Because all stress gage packages form an inclusion in the surrounding medium, it can be expected that the relationship between gage stress and free-field stress will be influenced by the following:

- Bonding of the gage package to the medium.
- Material property differences between the gage package and medium.
- Package/medium separation.
- Residual stress in the gage.
- Gage geometry.

Similarly, if the gage is placed in a borehole, the borehole is an inclusion in the surrounding medium and the stress in the borehole depends on the following:

- Bonding of the borehole filler to the medium
- Filler/medium properties mismatch
- Filler/medium separation conditions
- Orientation of the gage (stress component measurement)

- Filler residual stress
- Borehole geometry.

The sensitivity of the inclusion stresses to the above effects are investigated by finite element code calculation (Sections 2 and 4). For many field applications, the stress gradient is small compared with the inclusion dimensions, so static solutions are appropriate for these cases.

Solutions have been generated by classical analysis for cases where the inclusion and medium remain elastic, except for residual stress cases where the filler (grout) has been allowed to undergo plastic deformation (Section 3). These closed-form solutions are useful for parametric studies and the validation of finite element codes in the low stress regime.

The other main area of theoretical investigation in this program is the response of an ytterbium foil sensing element to shock waves (Section 5). This work has been performed by using a finite difference wave code, and it forms support for the basic experimental and theoretical work on piezoresistance being conducted for DNA by Y. M. Gupta. The calculations correspond to gas gun experiments in which ytterbium foil embedded in PMMA was subjected to a planar shock wave generated by an impacting flyer plate.

#### Experimental Investigations

The experimental program comprises two parts: (1) stress gage package design and performance, and (2) borehole inclusion effects. For the stress gage the work consists of the following:

- Gage design and fabrication
- Loading and unloading of gage in fluid, sand, grout (static), and PMMA (dynamic).

The loading and unloading experiments are designed to provide determine or known stress environments for comparison with the stress gage measurements, including possible residual stresses induced by the gage

inclusion. Appropriate results will be correlated with theoretical predictions.

For the filled borehole inclusion an experiment has been designed and the apparatus constructed, as described in Section 6. In the experiment, a general triaxial principal stress field can be established in a rectangular block of geologic material or rock simulant. A filled borehole can be provided along the major axis of the block so that stress-strain measurements can be compared in three basic cases: (1) no borehole, (2) borehole with bonded grout fill, and (3) borehole with unbonded grout fill. The experiment is also suitable for parametric studies (strengths, loading ratios, separation, geometry, and so forth). Suitable sensors are examined.

Dynamic (gas gun) loading of flatpack gages was investigated by numerical simulation to determine the feasibility of reducing gage dimensions appropriate to the dimensional limitations of the 4-inch-diameter gas gun. Because this investigation showed that the gas gun cannot provide pulses of adequate duration for flatpack gages, the design of a larger flyer plate facility was added to the program (Section 6).

## SECTION 2

### STATIC CALCULATIONS FOR FILLED BOREHOLE INCLUSIONS

#### 2.1 INTRODUCTION

Finite element calculations have been made for the filled borehole inclusion to let us compare the stresses acting normal to the gage planes with the free-field stresses to be measured. We present results for grout fill in tuff that show how this stress comparison is influenced by the following:

- Mismatch of borehole fill and medium properties
- Bonding of the borehole fill to the medium
- Separation of the borehole fill from the medium
- Formation and distribution of residual stresses.

Inclusion effects caused by the gage package are addressed in Section 4.

We have constructed simple, practical examples to illustrate clearly the above inclusion effects on stress measurement. To simplify the example, we made several reasonable assumptions or introduced limitations on the applicability. Our examples are quasi-static and apply to common cases where the rise time of the spherical stress wave is greater than the duration of several wave transits across the borehole diameter. The spherical wave engulfing the borehole is assumed to generate a stress field that can be adequately represented by a biaxial stress-plane strain state, as shown in Figure 2. The compressive stresses  $p_y$  and  $p_x$  represent the radial and circumferential components of the spherical wave. Another simplification was to adopt proportional loading; that is, to keep the stress ratio  $p_x/p_y$  constant. Once the dependency on the proportional loading ratio is understood, the borehole stress histories can be interpreted from more realistic loading paths (spherical wave components). The grout and tuff properties have been approximated in our initial calculations by elastic, perfectly plastic

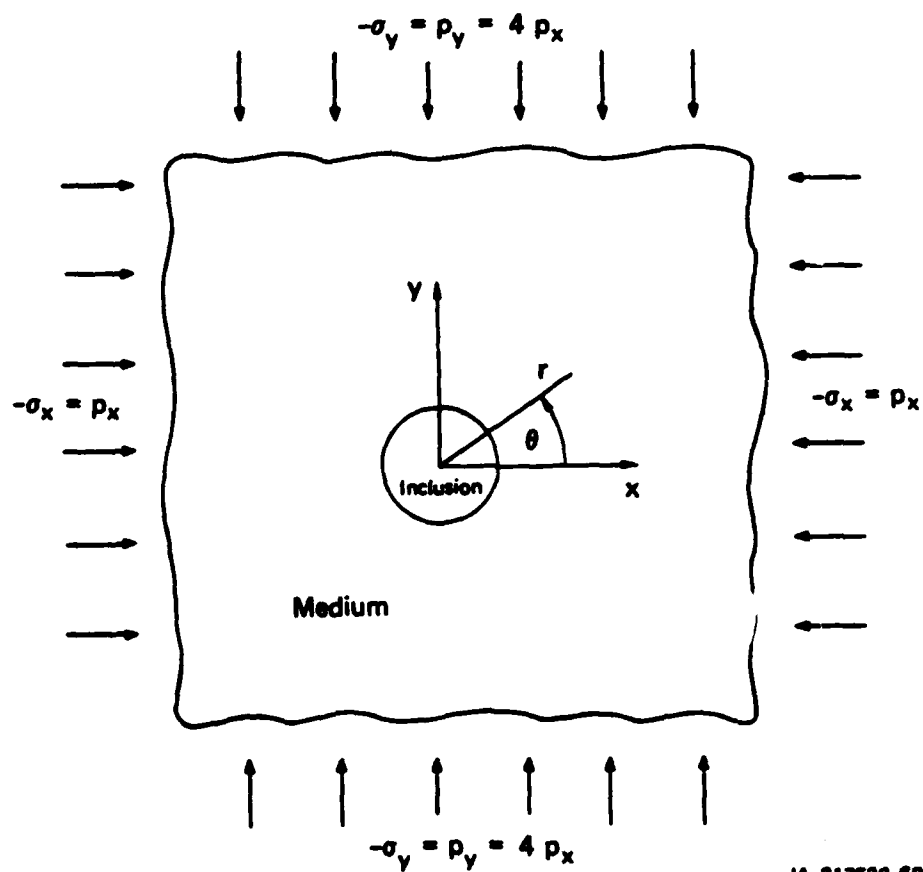


Figure 2. Circular inclusion under biaxial stress and plane strain.



behavior with yielding and plastic deformation according to the Mises yield condition and the associated flow rule. Mohr-Coulomb yielding and irreversible compressibility will be included in a later phase of the program. For the grout chosen, designated 2C4, and for several NTS tuffs, the friction angles are not large, so the Mises criterion is a reasonable approximation. It is probably more important to include plastic compressibility in the future.

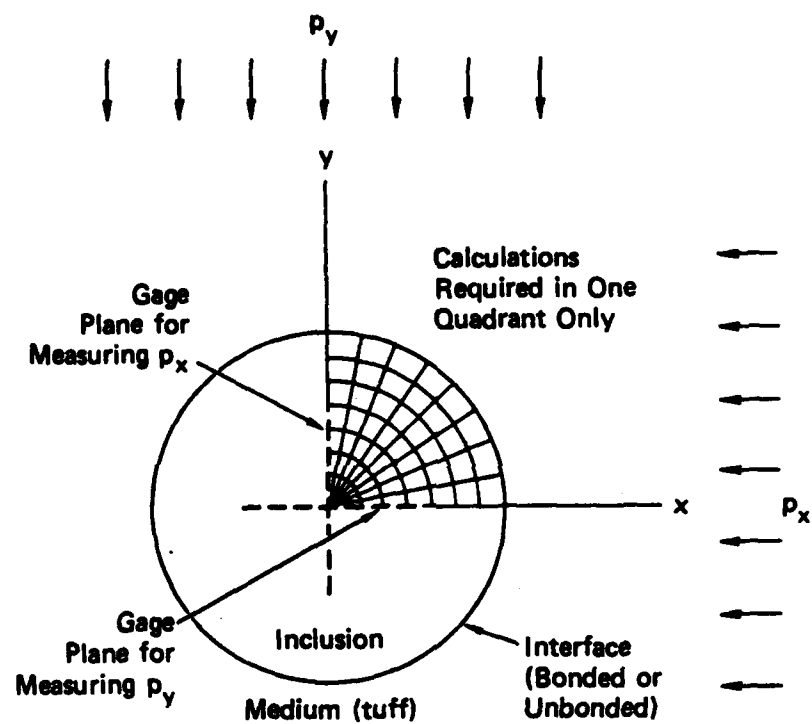
The material properties used in the calculations are listed in Table 1.

Table 1. Material Properties

Material	Young's Modulus, $E$ (psi)	Poisson's Ratio, $\nu$	Shear Modulus, $\mu$ (psi)	Crush Strength, $\sigma_o$ (psi)
Tuff medium	$1.66 \times 10^6$	0.32	$0.63 \times 10^6$	6370
Grout (2C4) fill	$2.64 \times 10^6$	0.28	$1.03 \times 10^6$	3910

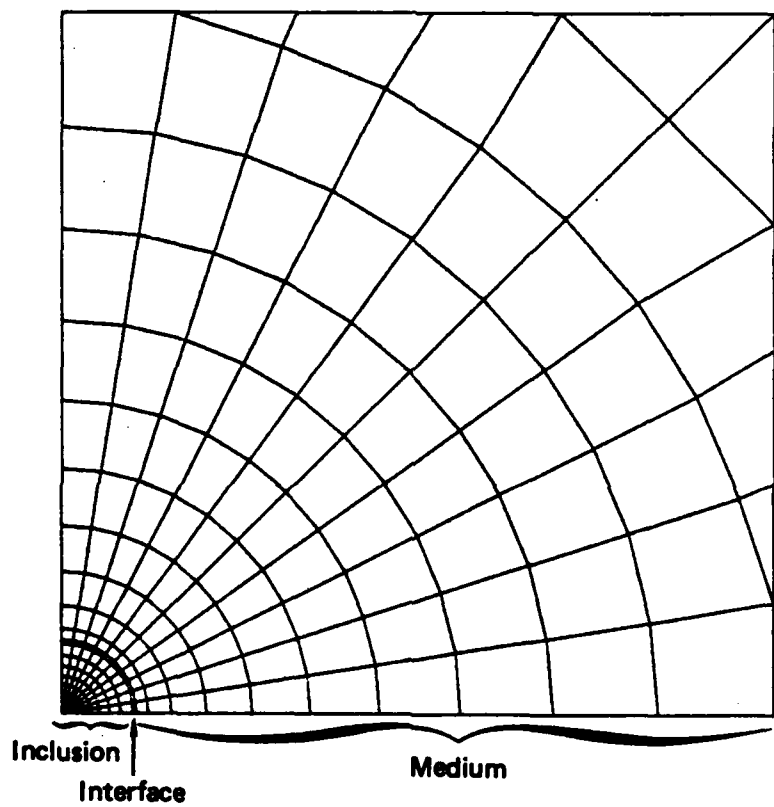
Figure 3 shows the two gage planes for measuring the free-field stress components  $p_x$  and  $p_y$ . Because of symmetry, only the first quadrant needs to be modeled. Stresses  $\sigma_x$  and  $\sigma_y$  are calculated in the inclusion along the radii on the  $y$  and  $x$  axes, respectively. The inclusion effect of the gage itself is not considered in these borehole calculations, and the stresses  $\sigma_x$  and  $\sigma_y$  along the  $y$  and  $x$  axes are taken to be the stresses acting on the two gages for comparison with the uniform free-field stresses.

The analyses were performed with the finite element code NIKE.<sup>2</sup> The finite element grid was extended to 10 times the inclusion radius, as shown in Figure 4. Four node plane-strain quadrilateral elements were used.



JA-317583-100

Figure 3. Gage locations in borehole.



JA-317522-87

Figure 4. Finite element grid.

Three inclusion-medium interface conditions are investigated. These include perfectly bonded, free-sliding, and frictional sliding conditions. The perfectly bonded and free-sliding interfaces provide bounds on the more realistic frictional sliding interface. The bonded interface transfers compressive, tensile, and shearing loads. The free-sliding interface transfers compressive loads only. The frictional sliding interface transfers compressive loads and limits the amount of shearing load that can be transferred.

The perfectly bonded interface requires no special modeling technique because the usual finite element node-element connectivity describes this condition.

The free- and frictional sliding interface capabilities are based on a finite element penalty function formulation. The interface geometry is defined by a list of nodal point numbers lying along both sides of the interface. One side of the contact surface is referred to as the master surface, and the other side is referred to as the slave surface. In a region of contact and sliding friction, interface springs are used to preclude penetration and sliding. Any node that penetrates through or slides away from its respective contact surface causes a linear interface spring to be inserted into the stiffness matrix; this spring couples the penetrating/sliding node to two adjacent nodes on the contact surface. An adjustable penalty parameter is input to scale the stiffness of the interface springs, and a coefficient of friction is input to prescribe the frictional behavior of the interface.

The numerical results treat the effects on the stress distributions acting normal to the gage planes of the:

- Interface conditions (tuff inclusion)
- Material properties (grout inclusion)
- Combined interface conditions and material properties
- Unloading (residual stress)
- Interface separation.

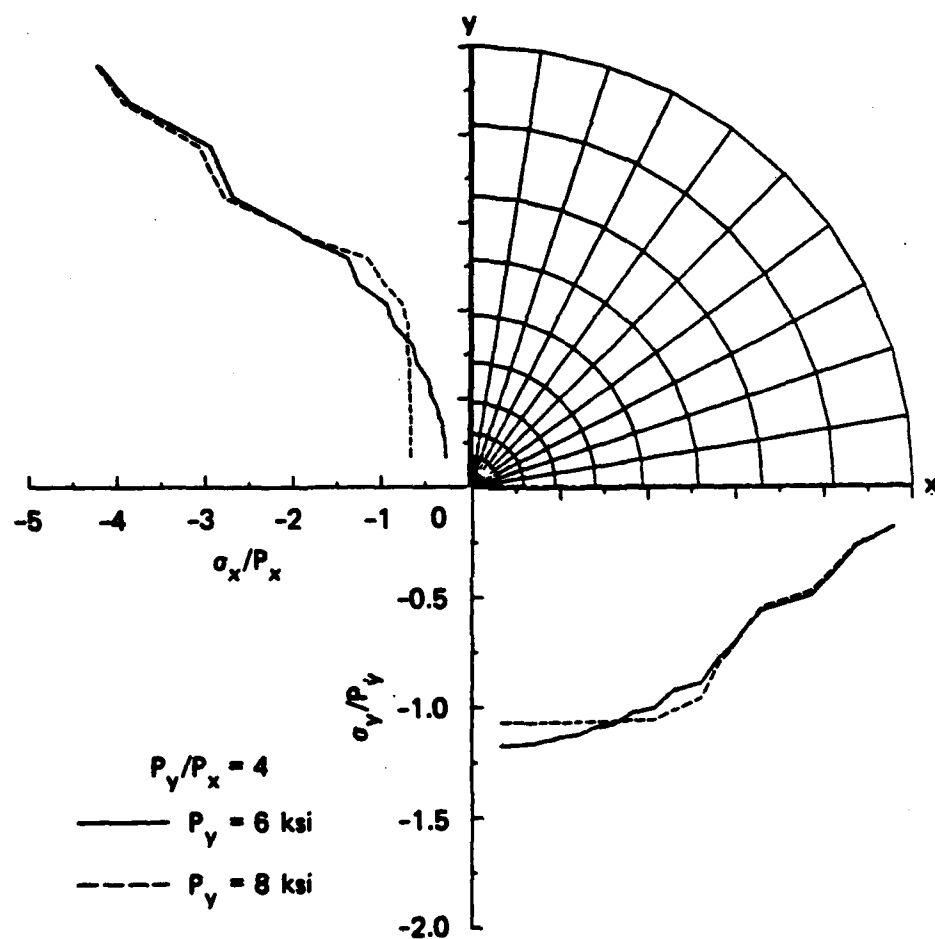
In all but one case, the media were taken to be an elastic-perfectly plastic Von Mises model of tuff. The calculations were made for two or three free-field stress levels, the lowest value in each case providing an entirely elastic response.

## 2.2 INTERFACE CONDITIONS

The ideal borehole inclusion would be perfectly bonded to and match the material properties of the surrounding media. If this state could be achieved, the stress distribution in the borehole would be identical to the free-field stress.

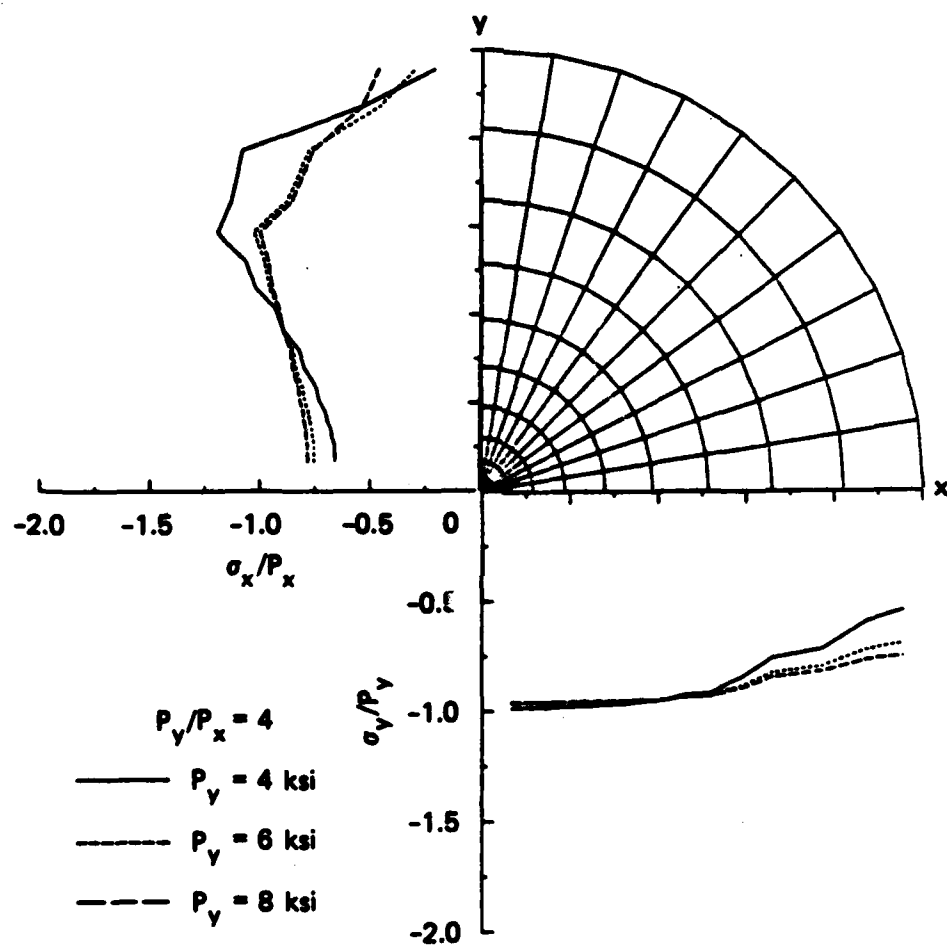
Figure 5 shows the stress distributions in an inclusion that matches the material properties of the media exactly, but allows the inclusion to slip freely along the interface. The stress distributions along the x and y axes are shown for a free-field compressive stress of  $P_y = 6$  and 8 ksi, with a proportional loading ratio of  $P_y = 4P_x$ . A gage along the x or y axis would measure the free-field stress exactly if the ratios of  $\sigma_x/P_x$  and  $\sigma_y/P_y$  are unity. The effect of a slip interface that does not transfer shear stress is to produce a nonuniform stress distribution along both axes. At the lower loading level,  $P_y = 6$  ksi, the tuff inclusion is elastic (solid lines), and at the center of the inclusion, the x and y stress components are 0.27 and 1.17 of their free-field counterparts, respectively. Increasing the free-field loading to 8 ksi causes yielding in the inclusion and flattens the stress distribution at the center, where the stress ratios are closer to unity (dashed lines). Approximate measurement of the large free-field stress,  $P_y$ , is possible if the gage does not occupy more than 50% of the inclusion diameter. Measurement of the smaller free-field component,  $P_x$ , can be regarded only as an estimate, the accuracy of which depends on the free-field stress level.

Figure 6 shows the stress distributions along the x and y axes of a tuff inclusion with a frictional interface with a coefficient of  $\mu = 0.6$  for free-field compressive stresses of  $P_y = 4, 6,$  and 8 ksi, and a loading ratio of  $P_y = 4P_x$ . The effect of including a frictional interface



JA-5877-16

Figure 5. Stress along gage planes for tuff inclusion with slip interface.



JA-5877-17

Figure 6. Stress along gage planes for tuff inclusion with frictional interface  $\mu = 0.6$ .

is to produce more uniform stress distributions than those obtained with a slip interface. The stress ratios (measured/free-field) of the x and y components, respectively, are 0.66 and 0.98 for elastic response and 0.78 and 0.95 for plastic response at  $P_y = 8$  ksi. The accuracy in measurement of both free-field stresses,  $P_x$  and  $P_y$ , increases in going from a slip to a frictional interface. The accuracy of measuring the larger free-field stress,  $P_y$ , would rapidly approach that obtainable for a bonded interface as the coefficient of friction is increased.

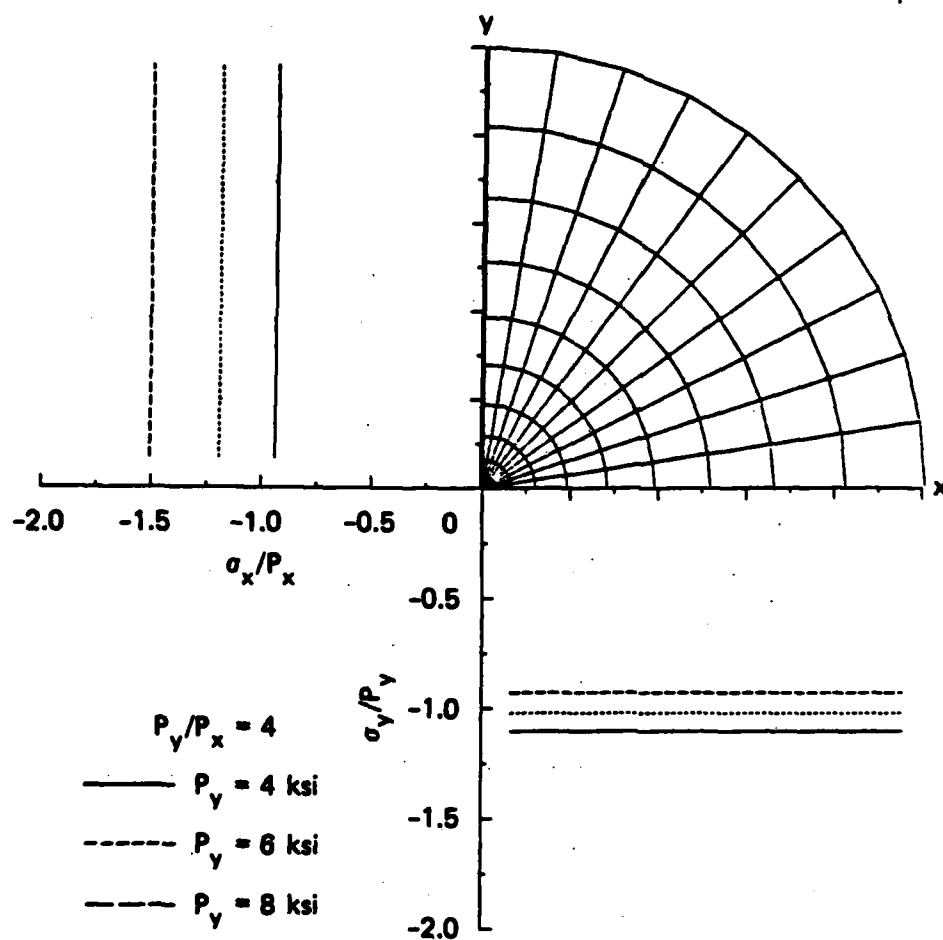
The coefficient of friction,  $\mu = 0.6$ , used in all the frictional interface calculations is an estimate of the sliding friction coefficient for tuff on tuff, based on a survey paper by Byerlee.<sup>3</sup> Methods for measuring the friction coefficients of tuff on tuff and tuff on grout for both sliding friction and bonding strength of a poured interface will be described in a future report.

### 2.3 MATERIAL PROPERTIES

In this section, we investigate the effect of having a borehole with material properties that do not match the surrounding media. The mismatch of a strong tuff and a weak grout (2C4) is intentionally chosen to magnify the effects of poorly matched properties.

Figure 7 shows uniform stress distributions along the x and y axes of a bonded grout inclusion for free-field compressive stresses of  $P_y = 4, 6, \text{ and } 8$  ksi, with a proportional loading ratio of  $P_y = 4P_x$ . The stress ratio for the larger free-field component,  $P_y$ , starts at 1.1 for elastic response and decreases to 0.93 for plastic response of the inclusion at  $P_y = 8$  ksi. Conversely, the smaller free-field stress,  $P_x$ , starts at 0.93 for elastic response and increases to 1.49 for plastic response at  $P_y = 8$  ksi. Because all the points in the inclusion are on the yield surface, this trend in stress ratios would continue with increasing load until a substantial portion of the medium near the borehole also reached the yield surface. When a significant portion of the medium yields, there would be a redistribution of load near the inclusion, which could change the stresses in the borehole. Even with





JA-5877-18

Figure 7. Stress along gage planes for grout inclusion with bonded interface.

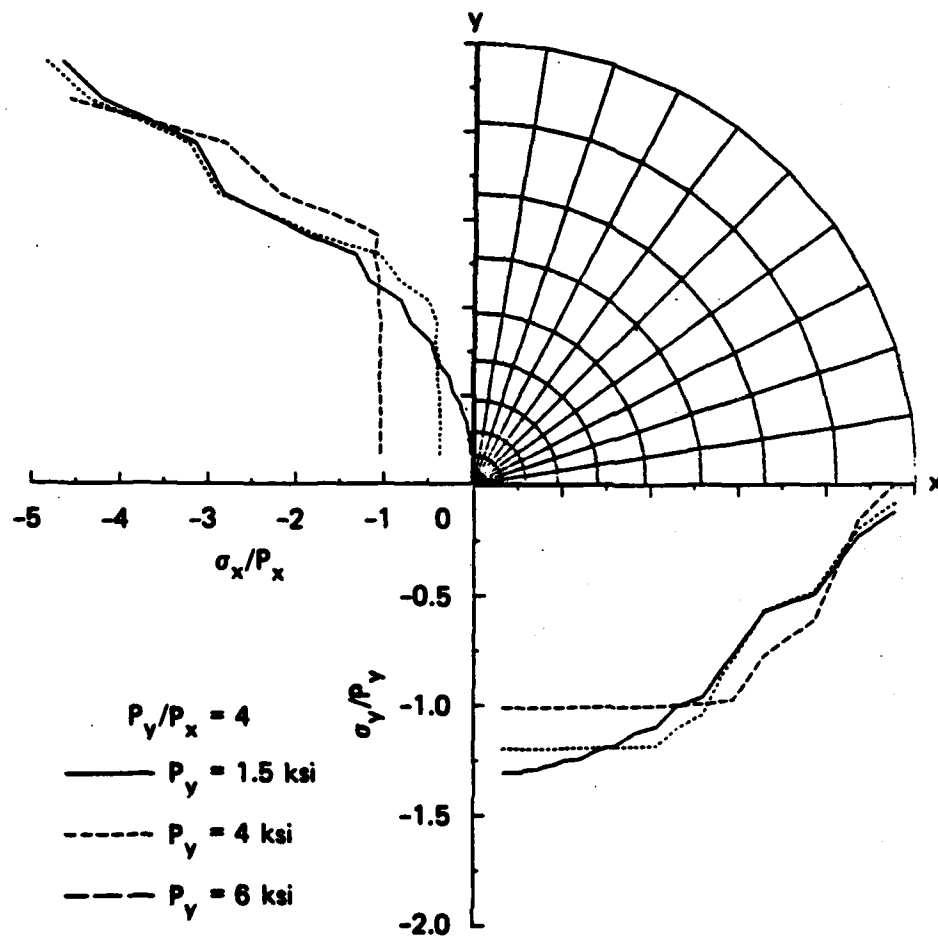
the mismatch of material properties in this example, a reasonably accurate measurement of the larger free-field stress,  $P_y$ , is obtained. The same is true for measurement of the smaller component under elastic or low level plastic loading. As the loading increases to produce more plastic deformations, measurements of  $P_x$  become more inaccurate.

## 2.4 INTERFACE CONDITIONS AND MATERIAL PROPERTIES

Figure 8 shows the stress distributions along x and y axes of a grout inclusion with a slip interface for free-field compressive stresses of  $P_y = 1.5, 4, \text{ and } 6 \text{ ksi}$ , with  $P_y = 4P_x$ . This example represents the worst case considered because it combines the effects of mismatched material properties and the lack of interface bonding. The effect of material mismatch is only significant in measurements of the smaller free-field stress,  $P_x$ , as seen in Figure 7. Comparing Figures 7 (bonded grout inclusion) and Figure 8 (slip grout inclusion), we concluded that the effect of bonding is to produce uniform stress distributions and to increase the accuracy of stress measurements at the lower free-field load levels. These conclusions are also illustrated in Figure 9, which shows the stress distributions along the x and y axes of a grout inclusion with a frictional interface. The results for the frictional interface are bounded by the bonded and slip interface results as expected.

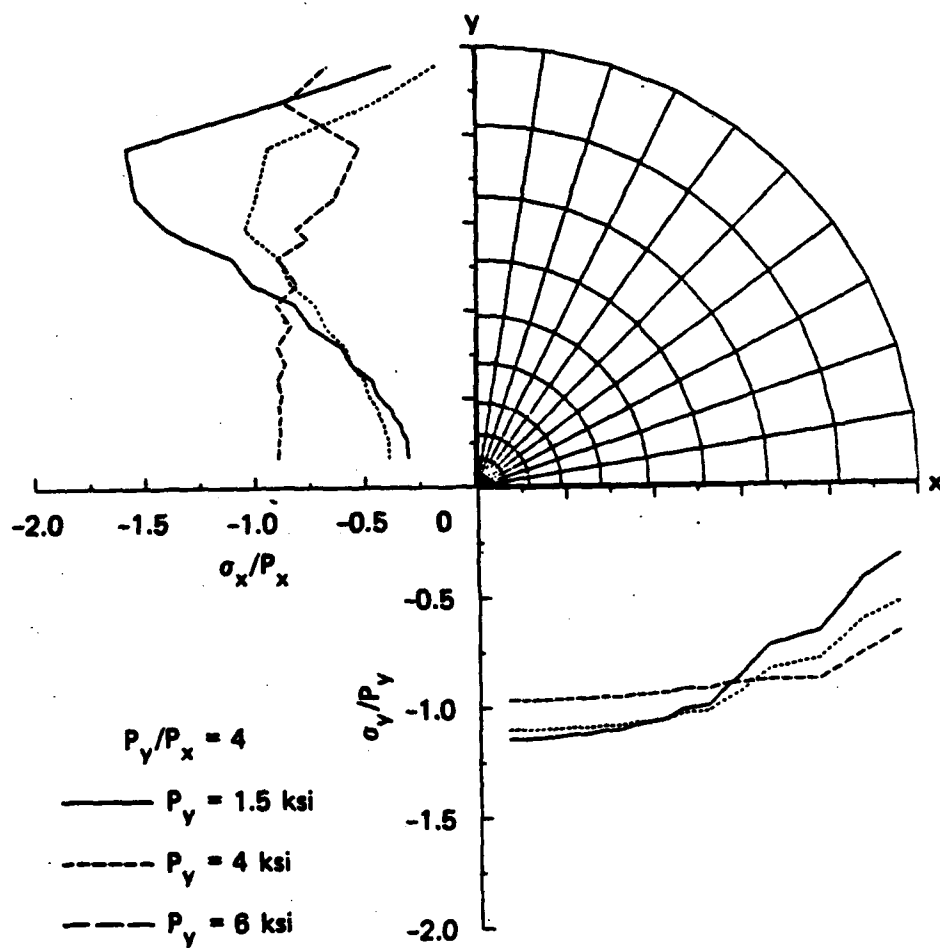
Based on the numerical examples for loading presented in Sections 2.2, 2.3, and 2.4, we conclude the following:

- Borehole material should be well bonded to the medium to ensure a uniform stress distribution.
- Borehole material properties should match the media properties for improved accuracy.
- Multiple stress component measurement is difficult to obtain directly.
- Ratio of borehole stress component to corresponding free field is not constant if slip occurs.
- Uniform ( $\pm 10\%$ ) stress regions exist for  $< 50\%$  of the plane of a gage.



JA-6877-19

Figure 8. Stress along gage planes for grout inclusion with slip interface.



JA-5877-20

Figure 9. Stress along gage planes for grout inclusion with frictional interface  $\mu = 0.8$ .

## 2.5 UNLOADING AND RESIDUAL STRESS

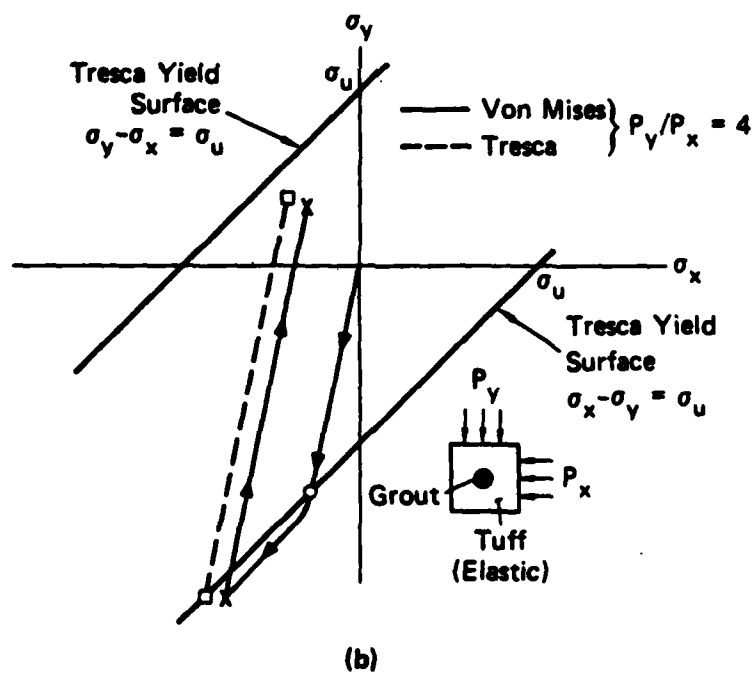
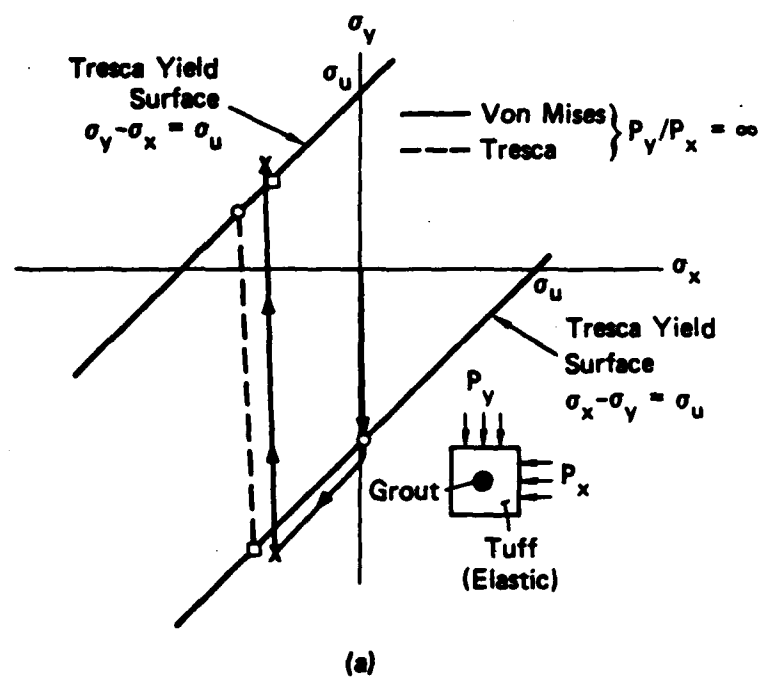
When the material in the borehole inclusion flows plastically before and during unloading, the mismatching of stress and displacement across the borehole interface and the mismatching of borehole material properties will result in a residual stress field. This residual stress field can prevent gage signals from returning to their original baseline and cause inaccurate impulse measurements. In this section, we investigate the magnitude of this problem.

The residual stress field is dependent on the entire history of loading and unloading, including proportional/nonproportional loading, maximum stress attained during loading, material characterization (constitutive model), and proportional/nonproportional unloading. To illustrate these dependencies, we considered a bonded grout inclusion surrounded by tuff that is loaded and unloaded proportionally.

Figure 10 shows the stress space trajectories of any material point in a bonded grout inclusion using Tresca and Von Mises yield criteria with two proportional loading and unloading ratios. Figure 10(a) shows the stress trajectories for the inclusion with a proportional loading and unloading ratio of  $P_y/P_x = \infty$  (i.e.,  $P_x = 0$ ) for Tresca (dashed line) and Von Mises (solid line) yield criteria. Figure 10(b) uses the same notation for the proportional loading ratio  $P_y/P_x = 4$ .

The Von Mises yield stress trajectory passes through the Tresca yield surface until it intersects the Von Mises yield surface. (Note: in the  $\pi$ -plane, the Von Mises yield surface is a circle that circumscribes the Tresca regular hexagon). Yielding continues along each of the yield surfaces until the larger free-field stress,  $P_y$ , reaches 8 ksi. The tuff media are then unloaded using the same ratio of  $P_y/P_x$  as in the loading phase. The unloading curves are parallel to the original elastic loading curves unless reverse yielding occurs on unloading, as it does along the Tresca trajectory in Figure 10(a).

The beginning and ending of the unloading trajectories are indicated by X's for the Von Mises yield criteria and squares for the



JA-5877-21

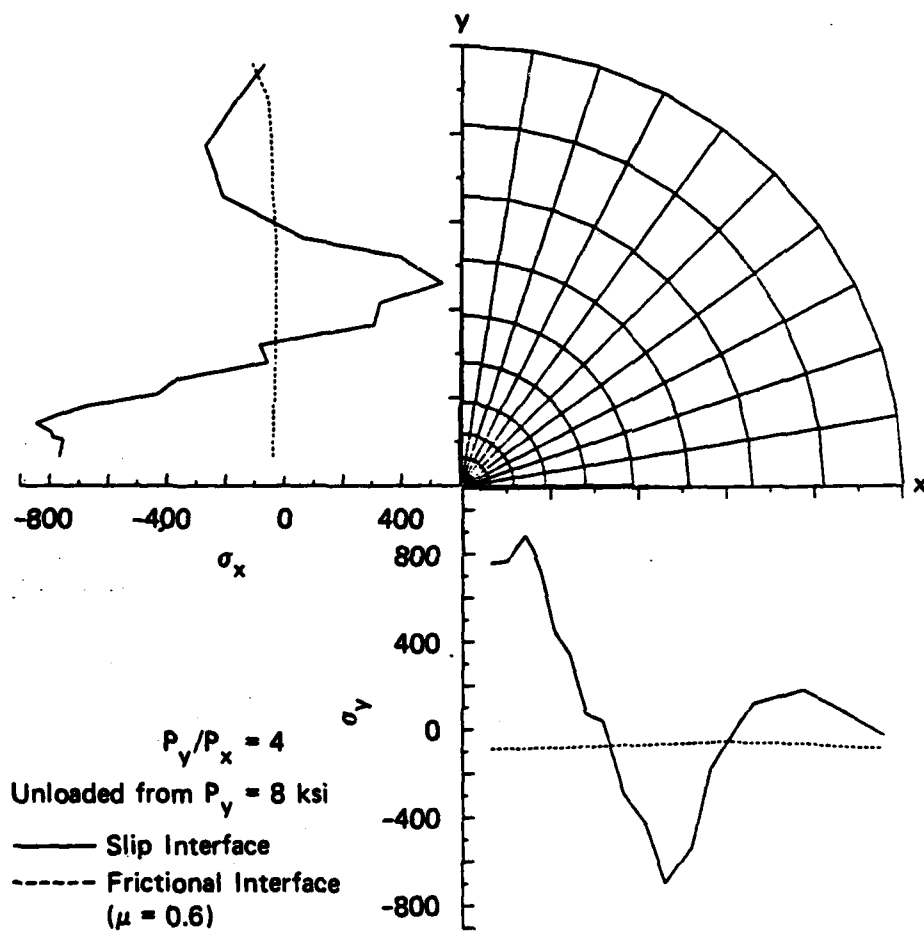
Figure 10. Stress trajectories in a bonded grout inclusion for Von Mises and Tresca yield criteria.

Tresca yield criteria in Figure 10. The final stress states for the two Von Mises trajectories are 1275 psi apart; the Tresca points are 582 psi apart. Comparison of the final stress states shows that in Figure 10(a) for the loading/unloading ratio of  $P_y/P_x = \infty$ , the Von Mises and Tresca states are 308 psi apart, and in Figure 10(b) for  $P_y/P_x = 4$ , the two points are 447 psi apart. From these results, we conclude that residual stress distributions are more dependent on loading and unloading ratios than constitutive relation. The choice of constitutive relation is probably more significant for rocks with higher friction angles where Mohr-Coulomb type yield criteria are appropriate and the mean pressure affects the residual stress field.

#### Effect of Interface Conditions on Residual Stress

Figure 11 shows the residual stress distributions in a tuff inclusion that was loaded to a free-field stress of  $P_y = 8$  ksi with a loading ratio of  $P_y/P_x = 4$ . The residual stress distributions are plotted for a slip interface (solid lines) and a frictional interface (dashed lines). The bonded interface does not result in a residual stress distribution. The resulting residual stress distributions have the same dependency on the interface condition that was found in the loading examples. Frictional interfaces produce low level uniform residual stress distributions, whereas slip interfaces produce large residual stresses that depend on location in the inclusion. The difference in residual stress distributions for the frictional and slip interfaces is that for bonding or high friction, all material points in the inclusion are at the same stress state. In the frictional interface inclusion, all points also unload uniformly and distribute the residual stress uniformly. The slip interface causes a distinct elastic-plastic zone to develop within the inclusion during loading, and hence causes differing amounts of residual stress during unloading.

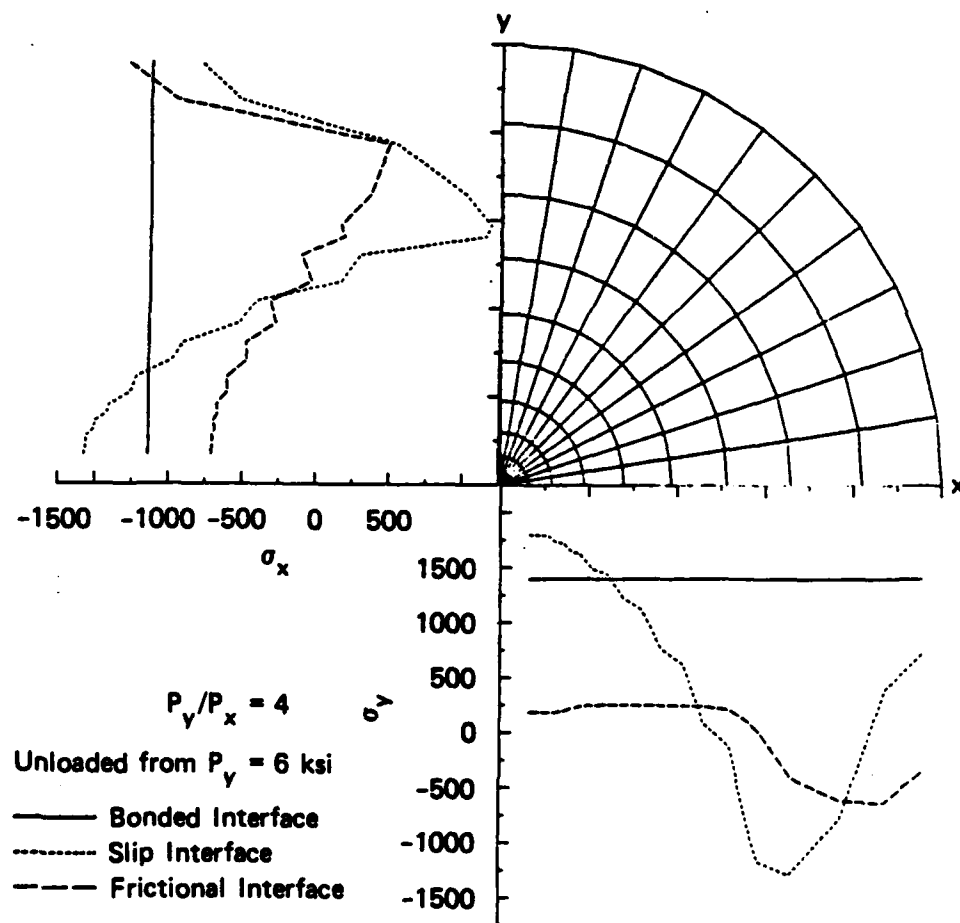
Figure 12 shows the residual stress distributions for a grout inclusion that has been loaded to a maximum free-field stress of  $P_y = 6$  ksi with  $P_y = 4P_x$ . The residual stress distributions for three



JA-5877-22

Figure 11. Residual stress along gage planes with tuff inclusion.





JA-5877-23

Figure 12. Residual stress along gage planes with grout inclusion.

interface conditions are plotted: bonded interface (solid lines), slip interface (short dashes), and frictional interface (long dashes). The bonded interface results in a large uniform residual stress distribution. The slip interface results in a residual stress field with the same distribution as that calculated for the tuff inclusion. The frictional interface produces the lowest level of residual stress and has a distribution similar to the slip interface.

The results presented in this section confirm some of the conclusions presented for the loading examples:

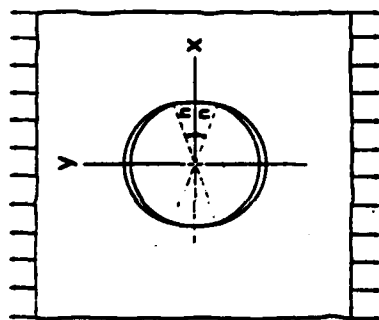
- Borehole material should be bonded to the media to ensure uniform stress distributions.
- Borehole material properties should match the media properties for minimal residual stress.
- Multiple stress component measurement is difficult to achieve directly.

## 2.6 INTERFACE SEPARATION

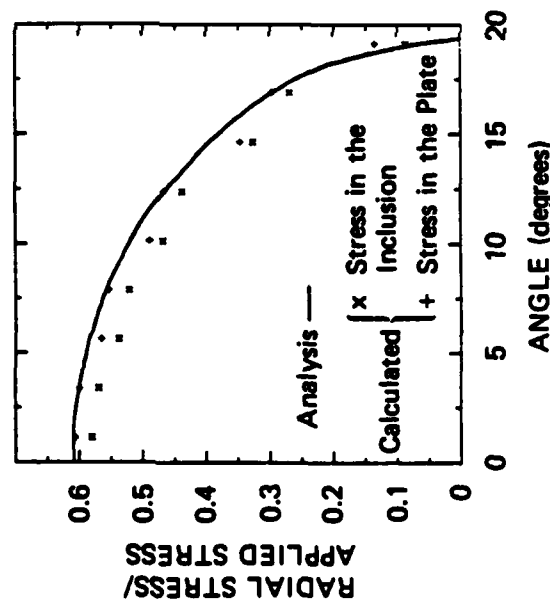
### Interface Separation Formulation

Clearly, stress measurements will be affected if the inclusion separates from the media. When elastic conditions prevail, the ratios of the free-field stress components that cause radial tension across the inclusion/medium interface can be determined explicitly. In the more general case of elastic-plastic loading and unloading, numerical algorithms will be needed to determine the stress distributions. The numerical separation algorithm was verified by simulating a sample problem whose analytical solution is known.

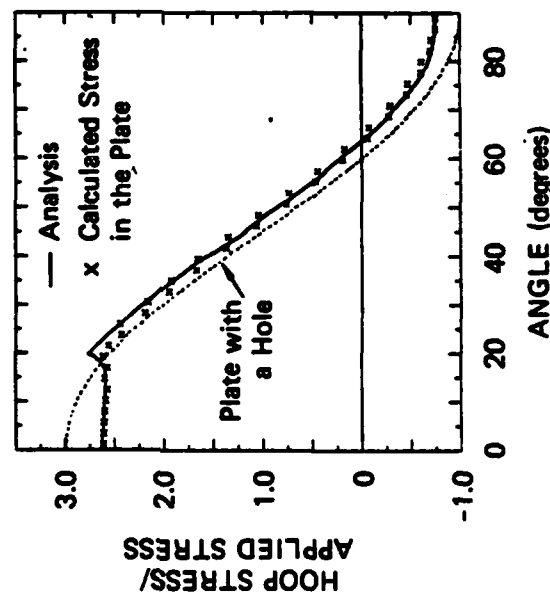
The example considers the plane-strain elastic contact between a circular disk and a circular hole in an infinite plate. The disk is smooth, and the diameter of the disk and the hole are identical in the unstressed state. A uniaxial stress is applied to the plate at infinity, resulting in a separation along a portion of the boundary between the plate and disk as indicated in Figure 13(a). The analytical solution for the arc of contact and the stress distribution along this arc are given in Reference 4.



(a) Contact Between Plate and Disk



(b) Compressive Radial Stress



(c) Circumferential Stress

JA-6877-24

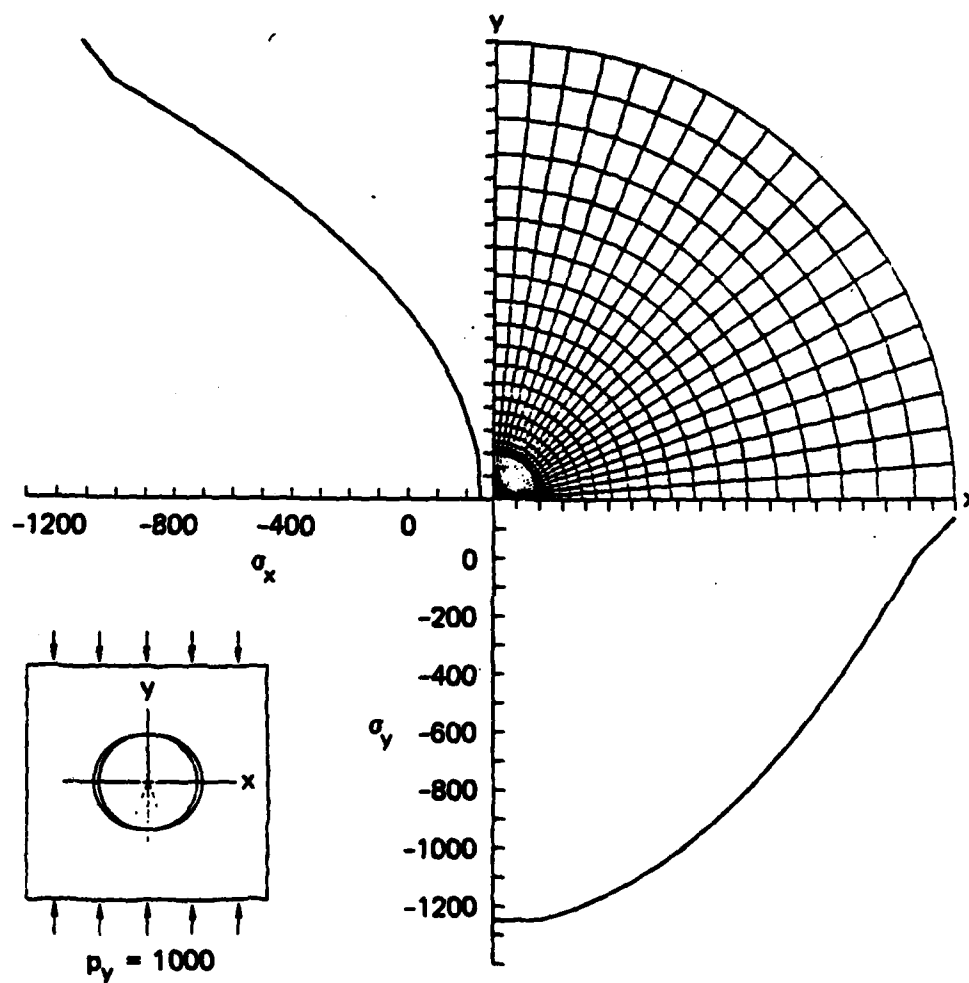
Figure 13. Contact/separation of a smooth disk in an infinite plate — analytical and computational solutions.

Figure 13(b) shows the radial stress distribution along the contact arc, an angle of  $19.62^\circ$ , for the analytical solution (solid line) and the calculated values in the plate (+'s) and in the inclusion (X's). The numerical results are in good agreement with the analysis and probably could be improved by refining the computational mesh.

Figure 13(c) shows analytical solutions of the hoop stress around the hole in an infinite plate for the contact of a smooth disk with a circular hole in an infinite plate (solid line); for comparison, an infinite plate with a circular hole—that is, no disk (dashed line) is shown. The computed hoop stress for the contacting disk (X's) shown in Figure 13(c) is in very good agreement with the analysis of the contacting disk.

#### Stress Distributions

If we let the uniaxial free-field stress be compressive so that  $\sigma_y = -p_y$  ( $p_y > 0$ ,  $\sigma_x = 0$ ), as shown in Figure 14 (lower left), the contact regions are centered on the y axis. The compression  $p_y$  was chosen at a value of 1000 stress units. As long as the material remains elastic, the stress distributions remain the same relative to this free-field compressive stress. Figure 14 shows the stress distributions  $\sigma_y$  and  $\sigma_x$  along the planes  $y = 0$  and  $x = 0$ , that is, along the gage planes. The stress distributions are nonuniform, being qualitatively parabolic in shape. The main stress component of interest,  $\sigma_y$ , is just over 20% high near the center of the borehole fill, but stress measurement is still useful if the gage is confined to the central half of the fill diameter.



JA-5877-38

Figure 14. Stress along the gage planes for the uniaxial compression of a smooth elastic disk in an infinite plate.

## SECTION 3

### STATIC ANALYSIS OF INCLUSIONS

#### 3.1 INTRODUCTION

We have obtained formulas for the stresses in elliptic and circular inclusions under plane strain conditions. The results apply when the inclusion and medium remain elastic, and we obtained them by performing analyses or adapting known analyses to solve our particular problems. The purposes of the analytic treatment are to validate the finite element code and to facilitate parametric investigations in the elastic regime. The elliptic inclusion results assist the study of the installation inclusion formed when the gages are inserted in slots from a trench wall. These results are also useful in developing stress gages of ytterbium foil in shear compliant material for laboratory applications, such as in DNA containment research.<sup>5</sup> The circular inclusion results apply to the inclusion formed by borehole fill.

The specific inclusion problems addressed are:

- Bonded general ellipse
- Bonded slender ellipse
- Bonded circle
- Unbonded circle (no interface shear)
- Separation conditions
- Residual stress in bonded circle (elastic-plastic inclusion)
- Rigid line inclusion.

The complex variable method of Muskhelishvili<sup>6</sup> is used to obtain the solutions, except when the circular inclusion becomes plastic during the residual stress investigation.

### 3.2 BONDED ELLIPTIC INCLUSIONS

Figure 15 shows an elliptic inclusion under plane strain conditions in a medium with far-field principal stresses  $\sigma_x = -p_x$ ,  $\sigma_y = -p_y$ . For a perfectly bonded interface, the stress distribution in the inclusion is uniform and equal to

$$\begin{aligned}\sigma_x &= 2A_1 - B_1 \\ \sigma_y &= 2A_1 + B_1\end{aligned}\quad (1)$$

where

$$A_1 = \frac{\alpha k_2 [\{\alpha k_2 - (\alpha - 1)(1 + m^2)\}C_1 - (\alpha - 1)m G_1]}{k_1 [\alpha k_2 - (\alpha - 1)(1 - m^2)] + 2(\alpha - 1)(1 - m^2)[\alpha k_2 - (\alpha - 1)]}$$

$$B_1 = \frac{-[k_1 + 2(\alpha - 1)]A_1 + \alpha k_2 C_1}{(\alpha - 1)m}$$

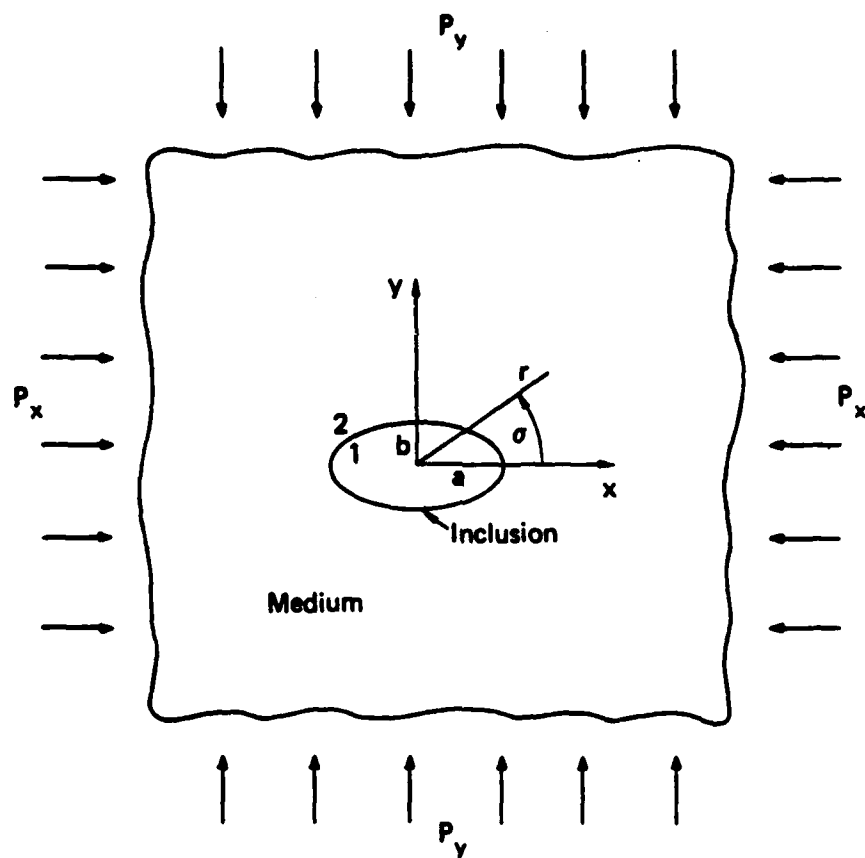
$$C_1 = -\frac{1}{4}(p_y + p_x) \quad G_1 = -\frac{1}{2}(p_y - p_x)$$

$$m = \frac{a - b}{a + b} \quad \alpha = \mu_1/\mu_2$$

$$k_1 = 4(1 - \nu_1) = 2 \frac{4 + \frac{3K_1}{\mu_1}}{1 + \frac{\mu_1}{3K_1}} \quad k_2 = 4(1 - \nu_2) = 2 \frac{4 + \frac{3K_2}{\mu_2}}{1 + \frac{\mu_2}{3K_2}}$$

The subscript 1 refers to properties within the inclusion, and the subscript 2 refers to properties within the medium.  $K_1$  and  $K_2$  are the bulk moduli,  $\mu_1$  and  $\mu_2$  are the shear moduli, and  $\nu_1$  and  $\nu_2$  are Poisson's ratios.

We use the above result to determine the stresses in a bonded slender ellipse and in a bonded circle for the study of a gage package and a borehole fill inclusion, respectively.



JA-6877-1

Figure 15. Elliptic inclusion under biaxial stress.



### 3.3 BONDED SLENDER ELLIPTIC INCLUSION

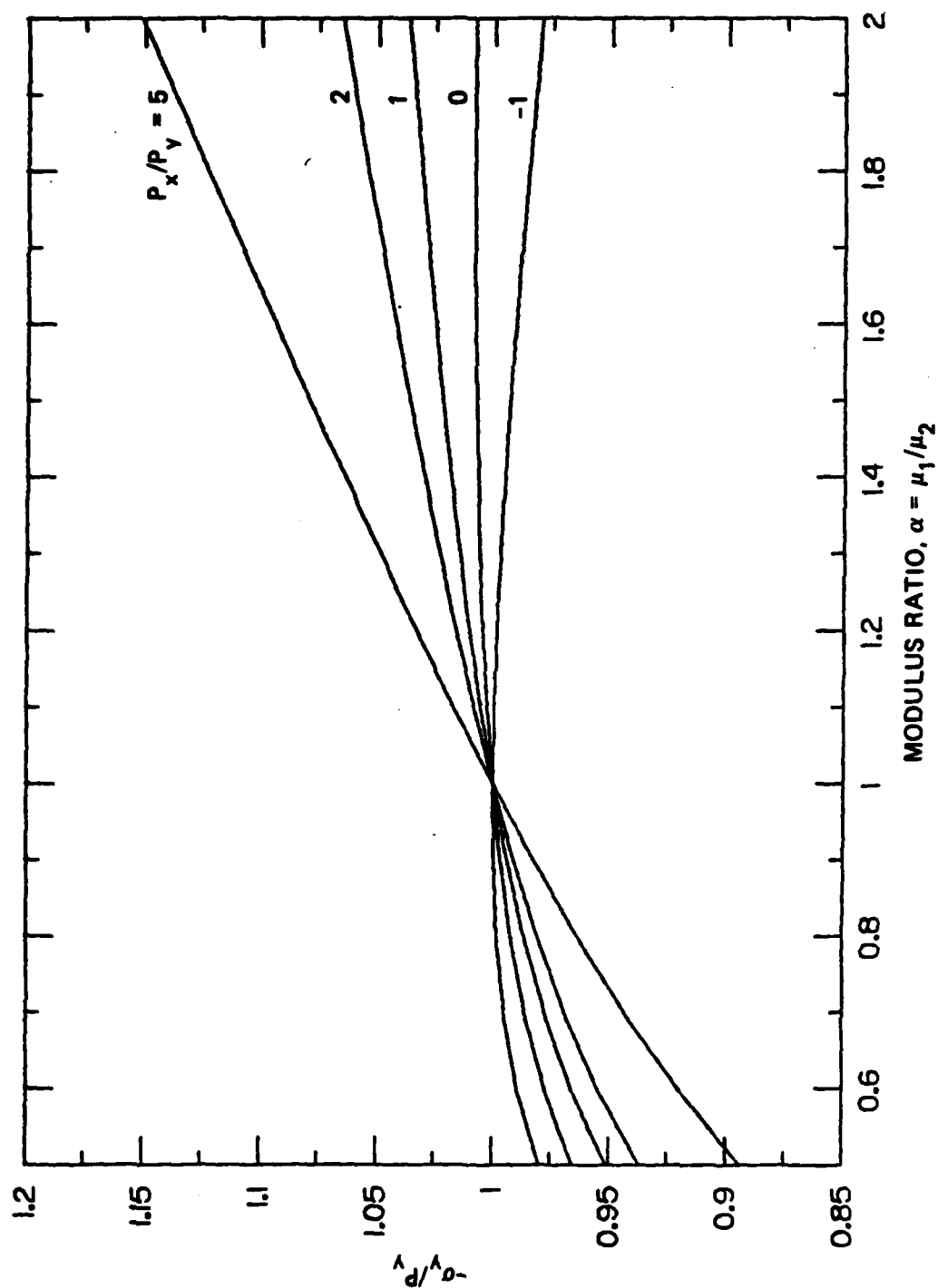
The slender elliptic inclusion is of interest because it represents an overall elastic behavior of a flatpack and the elastic behavior of a laboratory stress gage with an ytterbium foil embedded in fluid or a shear compliant material such as silicone.

Let the ratio of the minor and major axes be  $b/a = \epsilon$ , where  $\epsilon$  is a small number defining the slenderness ratio. Substitute  $m = (1 - \epsilon)/(1 + \epsilon)$  in Equation (1) and neglect terms in  $\epsilon$  higher than the first order. Then we obtain for the stress  $\sigma_y$  the formula

$$\frac{\sigma_y}{p_y} = -1 + \epsilon \left[ 1 - \frac{\alpha k_2 - 6(\alpha - 1)}{k_1} - \frac{4(\alpha - 1)}{\alpha k_2} - \frac{8(\alpha - 1)^2}{k_1 \alpha k_2} \right] + \epsilon \left[ 1 - \frac{\alpha k_2 - 2(\alpha - 1)}{k_1} \right] \frac{p_x}{p_y} \quad (2)$$

The stress within the inclusion is dependent upon the aspect ratio of the ellipse,  $\epsilon = b/a$ ; the material properties,  $\nu_1, \nu_2$ , and  $\alpha = \mu_1/\mu_2$ ; and the free-field stress ratio  $p_x/p_y$ . When the material in the inclusion is the same as the medium ( $\alpha = 1, k_1 = k_2$ ), Equation (2) gives  $\sigma_y = -p_y$ , as it should.

As the aspect ratio of the ellipse becomes small ( $\epsilon \rightarrow 0$ ), Equation (2) gives  $\sigma_y \rightarrow -p_y$ . If the ellipse can be made very slender, it does not matter whether or not the material elastic properties in the inclusion match those in the medium. Figure 16 shows how the ratio  $-\sigma_y/p_y$  varies with the property ratio  $\alpha = \mu_1/\mu_2$  and loading ratio  $p_x/p_y$  for an ellipse of aspect ratio  $\epsilon = 0.1$ . As in the case of grout and tuff, we assume that the values of the Poisson's ratio,  $\nu$ , are comparable, so for simplicity we have chosen  $\nu = 0.3$ , the average of the values in Table 1. Over the range  $1/2 < \mu_1/\mu_2 < 2$ , whenever  $|p_x/p_y| \leq 1$ , we see that the inclusion stress component  $-\sigma_y$  is within 5% of the free-field stress component  $p_y$ . When the inclusion material is weaker than the medium ( $1/2 < \mu_1/\mu_2 < 1$ ), the inclusion stress is lower than the free-field stress. When the inclusion material is stronger ( $1 < \mu_1/\mu_2$ ), the inclusion stress is higher than the free-field stress.



JA-5877-28

Figure 16. Stress in a bonded slender elliptic inclusion ( $\nu_1 = \nu_2 = 0.3$ ;  $\epsilon = 0.1$ ).

In summary, if we wish to measure  $p_y$ , the slender elliptic inclusion allows us to do this with acceptable accuracy unless the lateral component  $p_x$  becomes too large, say  $|p_x/p_y| > 2$ .

In one design of stress gage, the ytterbium foil is surrounded by a material that may be considered a fluid, that is,  $\mu_1 \approx 0$  and  $\nu_1 \approx 1/2$  ( $\alpha \approx 0$ ,  $k_1 \approx 2$ ). The pressure in the fluid inclusion is determined by Equation (2) as

$$-\frac{\sigma_y}{p_y} = 1 + \epsilon \frac{1 - 2\nu_2}{1 - \nu_2} \left[ 1 - \frac{3}{2(1 + \nu_2)} \frac{K_2}{K_1} \right] \quad (3)$$

Equation (3), to the first order in  $\epsilon$ , shows that the inclusion pressure is independent of the free-field stress component,  $p_x$ . Figure 17 shows the variation of the inclusion pressure with the medium Poisson's ratio,  $\nu_2$ , and the ratio of the bulk moduli,  $K_1/K_2$ . The curves show that the inclusion pressure is within 5% of the free-field stress,  $p_y$ , when the fluid bulk moduli is greater than the medium bulk modulus by up to a factor of three. They also show that the fluid modulus should not be less than half the medium bulk modulus, based on about a 90% accuracy when  $\nu_2 \approx 0.3$ .

### 3.4 BONDED CIRCULAR INCLUSION

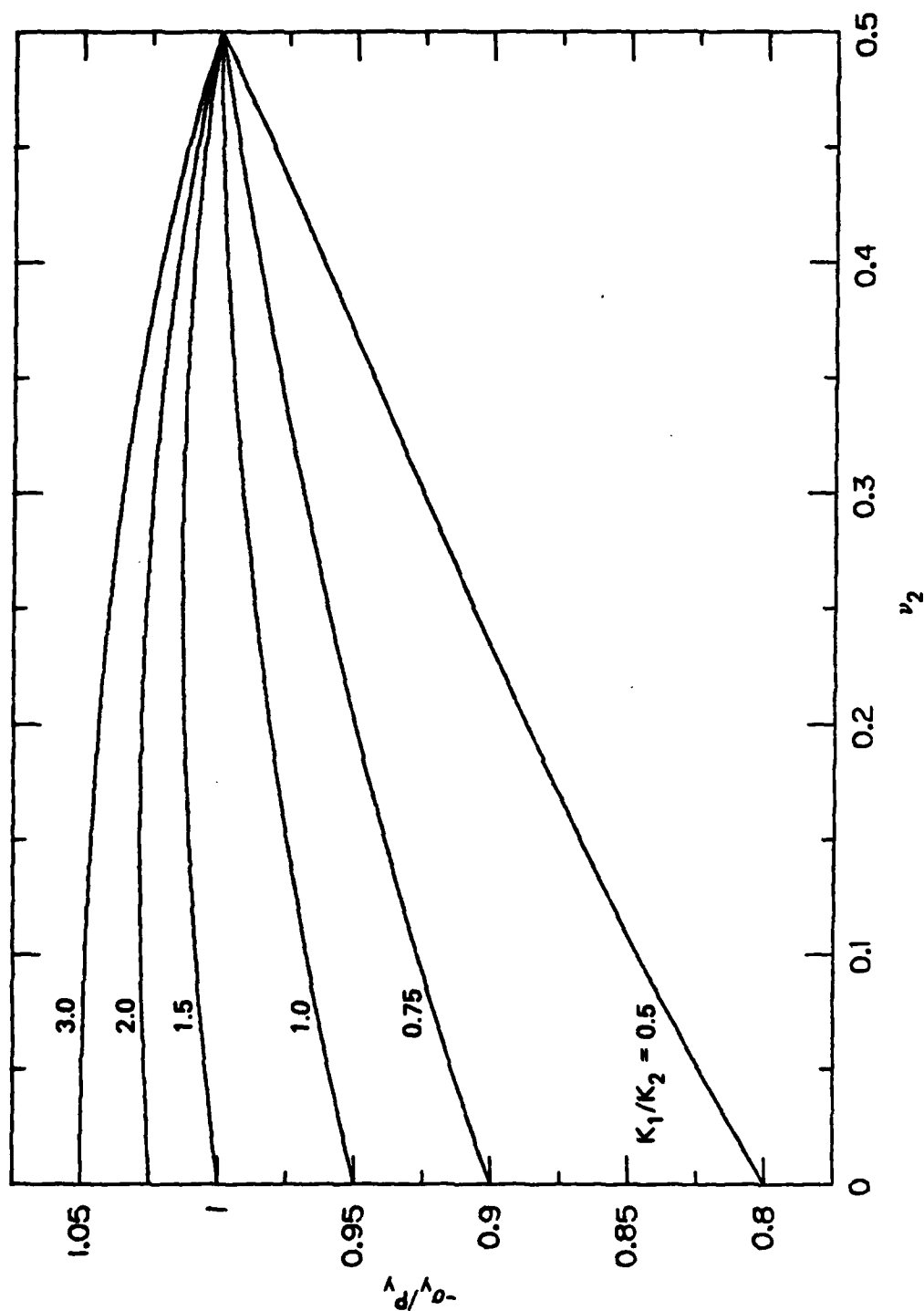
The stress  $\sigma_y$  in a bonded circular inclusion representing the borehole fill is obtained by specializing Equation (1) to the case  $m = 0$ , giving  $a = b$ . This process leads to

$$\frac{\sigma_y}{p_y} = -\frac{1}{2} \left( \frac{p_x}{p_y} + 1 \right) \beta + \frac{1}{2} \left( \frac{p_x}{p_y} - 1 \right) \delta \quad (4)$$

where

$$\beta = \frac{\alpha k_2}{k_1 + 2(\alpha - 1)}$$

$$\delta = \frac{\alpha k_2}{\alpha k_2 - (\alpha - 1)}$$



JA-6877-27

Figure 17. Pressure in a slender elliptic fluid inclusion ( $\epsilon = 0.1$ ).

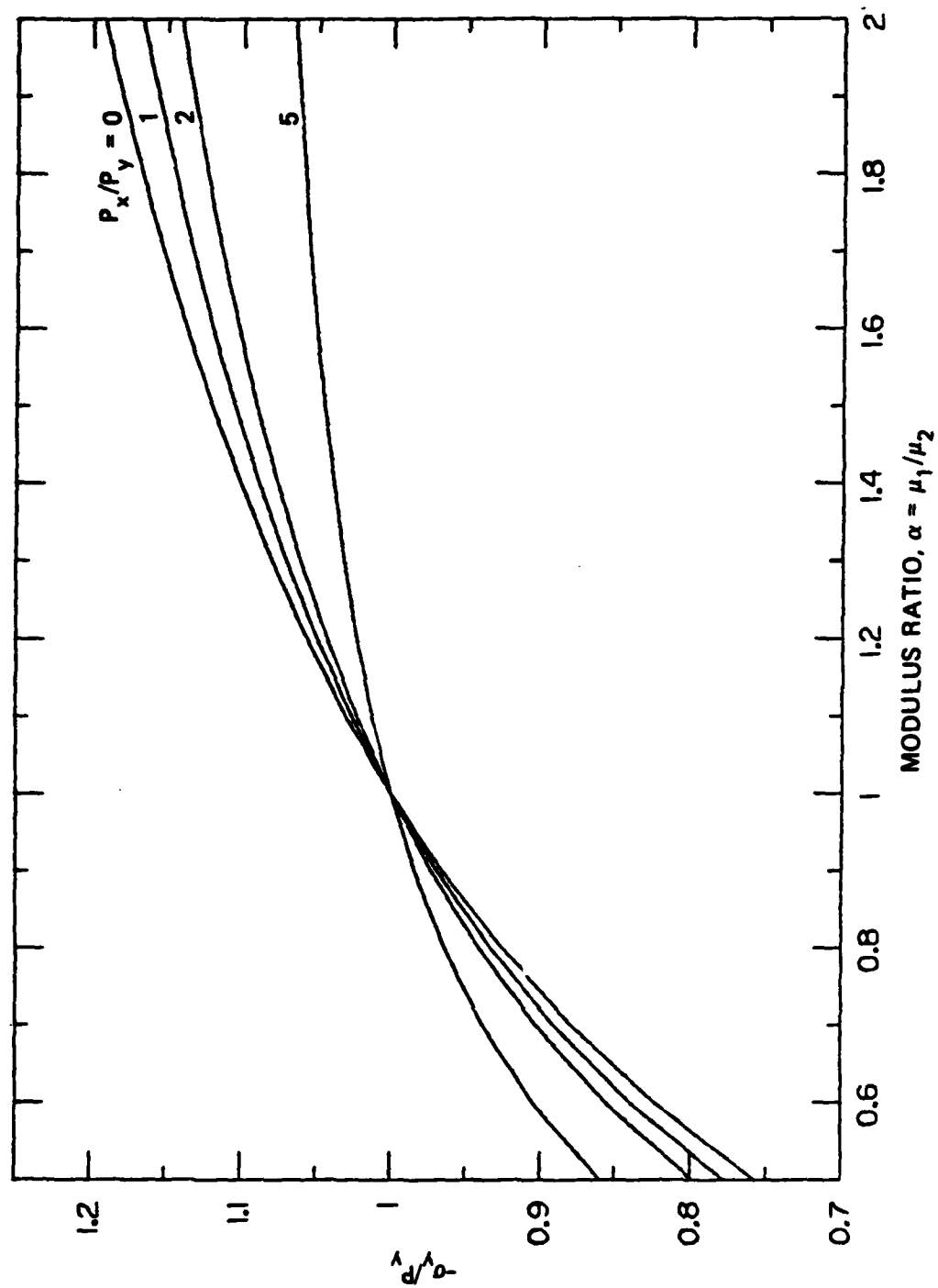
and where again  $\alpha = \mu_1/\mu_2$ ,  $k_1 = 4(1 - \nu)$ , and  $k_2 = 4(1 - \nu_2)$ . The degree to which the stress,  $\sigma_y$ , measured within the inclusion matches the free-field stress component,  $p_y$ , depends on the ratio  $\alpha$  of the shear moduli, Poisson's ratio  $\nu_1$  and  $\nu_2$ , and the ratio  $p_x/p_y$  of the free-field stress components. For the special case in which the inclusion and medium are the same material ( $\alpha = 1$ ,  $k_1 = k_2$ ), Equation (4) gives  $\sigma_y = -p_y$ , as it should.

Figure 18 shows how the ratio  $-\sigma_y/p_y$  varies with the property and loading ratios  $\mu_1/\mu_2$  and  $p_x/p_y$ . As in the case of grout and tuff, we assume that the values of the Poisson's ratio,  $\nu$ , are comparable, so for simplicity we have chosen  $\nu = 0.3$ , the average of the values in Table 1. The curves pass through the point (1,1) representing the case of identical inclusion and medium materials (or no inclusion). When the inclusion is stiffer than the medium ( $\mu_1/\mu_2 > 1$ ), the stress measured in the inclusion is high ( $-\sigma_y/p_y > 1$ ). For  $\mu_1 = 2\mu_2$  and  $p_x = 0$ , the measurement is about 20% high; the accuracy improves as  $p_x$  increases. When the inclusion is more compliant than the medium ( $\mu_1/\mu_2 < 1$ ), the stress measured in the inclusion is low ( $-\sigma_y/p_y < 1$ ). For  $\mu_1 = \mu_2/2$  and  $p_x = 0$ , the measurement is about 25% low; again, the accuracy improves as  $p_x$  increases.

Figure 18 illustrates that when elastic behavior dominates, it is good practice to match the medium modulus with an inclusion modulus to within about 20% if lower than the medium modulus and about 40% if higher.

### 3.5 UNBONDED CIRCULAR INCLUSION

If the gage installation procedure results in a bond between the borehole fill inclusion and the medium that is weak in shear strength, the loading may cause slip to occur along the interface. The slip radically alters the stress distribution in the inclusion. In the extreme case of an interface with no shear strength, this stress distribution is



JA-5877-28

Figure 18. Stress in a bonded circular inclusion ( $\nu_1 = \nu_2 = 0.3$ ).

$$\begin{aligned}\frac{\sigma_y}{p_y} &= -\frac{1}{2} \left( \frac{p_x}{p_y} + 1 \right) \beta + \frac{1}{2} \left( \frac{p_x}{p_y} - 1 \right) \delta \left( 1 - \frac{2x^2}{a^2} \right) \\ \frac{\sigma_x}{p_x} &= -\frac{1}{2} \left( \frac{p_y}{p_x} + 1 \right) \beta + \frac{1}{2} \left( \frac{p_y}{p_x} - 1 \right) \delta \left( 1 - \frac{2y^2}{a^2} \right)\end{aligned}\quad (5)$$

where

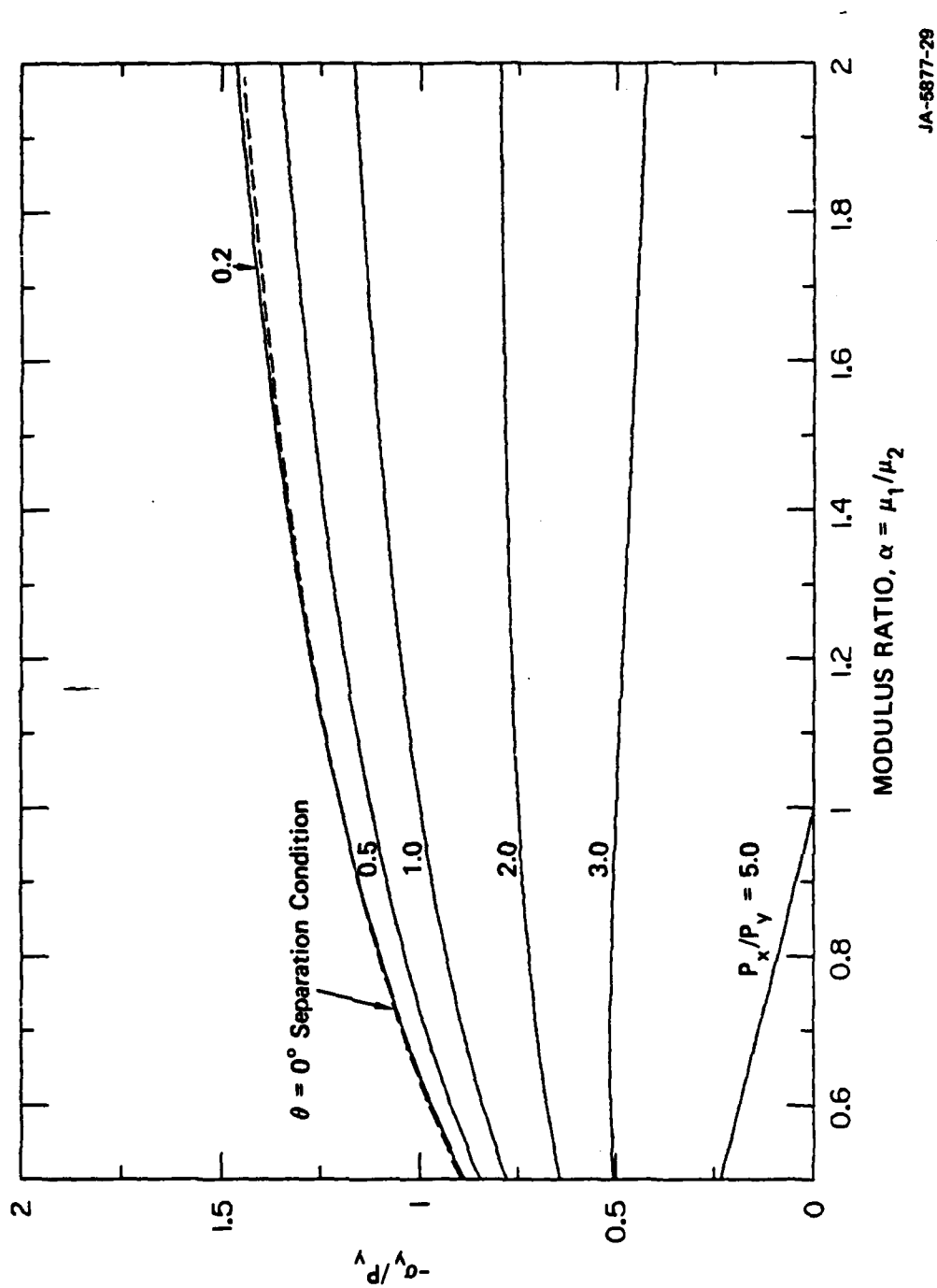
$$\beta = \frac{\alpha k_2}{k_1 + 2(\alpha - 1)} \quad \text{and} \quad \delta = \frac{6\alpha k_2}{k_1 + 3\alpha k_2 - 2(\alpha - 1)}$$

$$\alpha = \mu_1/\mu_2 \quad k_1 = 4(1 - \nu_1) \quad k_2 = 4(1 - \nu_2)$$

Equation (5) shows that the inclusion stress depends on the material properties through Poisson's ratios  $\nu_1$  and  $\nu_2$  and the ratio  $\alpha$  of the shear moduli, and on the loading ratio  $p_x/p_y$ , as in the case of the bonded interface. However, in stress distribution of each component is no longer uniform, but is parabolic in the Cartesian coordinate system.

A stress gage located on the  $x$  axis for measuring the stress  $\sigma_y$  would be subjected to a parabolic stress distribution with a maximum compressive stress at the center ( $x = 0, y = 0$ ) when  $p_y > p_x$ . (Note that the parameters  $\beta$  and  $\delta$  are positive.) For the same case, a stress gage located on the  $y$  axis for measuring the stress  $\sigma_x$  would be subjected to a parabolic stress distribution with a minimum compressive stress at the center.

Figure 19 shows the variation of  $-\sigma_y/p_y$  with the shear modulus ratio,  $\alpha$ , and the loading ratio  $p_x/p_y$  when  $\nu_1 = \nu_2 = 0.3$ , a value appropriate for NTS tuff. The stress values are for the center of the inclusion; we set  $x = 0$  in Equation (5). As stated above, if  $p_x/p_y < 1$ , Figure 19 shows the maximum compressive stress, and if  $p_x/p_y > 1$ , Figure 19 shows the minimum compressive stress. If  $p_x = p_y$ , the stress distribution is, of course, uniform. If the gage occupies a small enough portion of the diameter on the  $x$  axis, the influence of the parabolic distribution will be reduced and, as an approximation, the gage stress will be determined by Figure 19. We see immediately that stress measurement is reasonable only when  $p_y > p_x$ , although estimates are possible for values of  $p_x$  in the range  $p_y < p_x < 3p_y$ .



JA-5877-29

Figure 19. Stress in an unbonded circular inclusion ( $\nu_1 = \nu_2 = 0.3$ ;  $x = 0$ ).



As a final comment on Figure 19, when values of the loading ratio  $p_x/p_y$  are less than about 0.5 and greater than about 5 (depending on the shear modulus ratio), the inclusion and medium can separate if the interface bond has negligible tensile strength. Separation will affect the stress distribution. The upper curve indicates that separation will occur at  $\theta = 0$  for low values of the lateral loading  $p_x$ . Separation will occur at  $\theta = 90^\circ$  for high values of the lateral stress when the  $p_x/p_y$  curve intersects the abscissa, the  $\alpha$  axis.

Figure 20 shows the variations of  $-\sigma_y/p_y$  with the loading ratio,  $p_x/p_y$ , at several points along the positive  $x$  axis in the inclusion when the inclusion and medium are 2C4 grout and tuff with the elastic properties listed in Table 1 ( $\mu_1/\mu_2 = 1.63$ ). At each radius, given by  $x/a$ , the curves are straight lines in accordance with Equation (5). The farther the values of the loading ratio are from unity, the more pronounced is the parabolic stress distribution along the  $x$  axis, and the parabola inverts as we pass through  $p_x/p_y = 1$ .

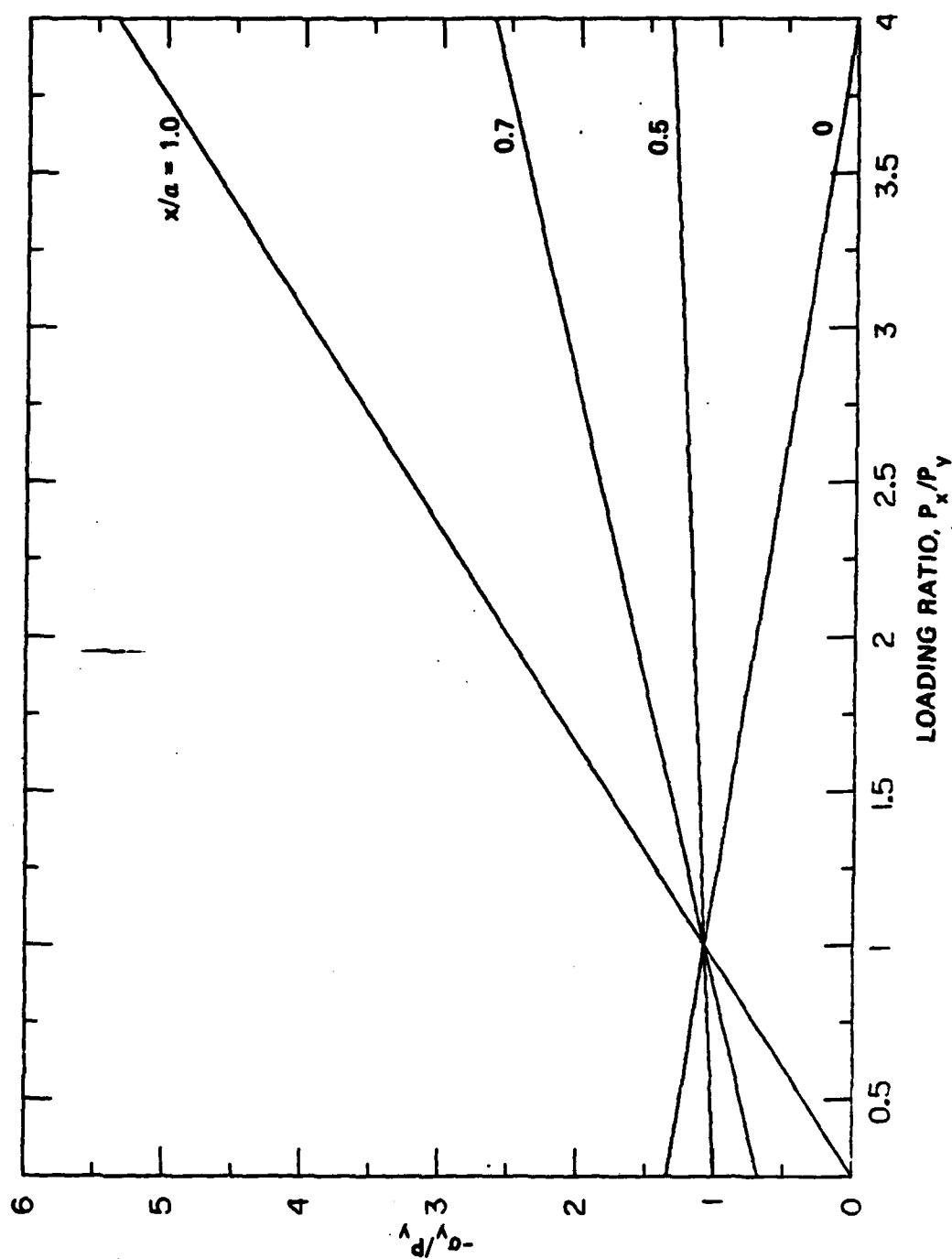
Figure 21 shows the variation of  $-\sigma_y/p_y$  with the loading ratio,  $p_x/p_y$ , at the center and midradius of an inclusion of 2C4 grout in a tuff medium, again with the elastic properties listed in Table 1. The third line (dashed) is bonded interface according to Equation (4); for the bonded case, the stress  $\sigma_y$  applies throughout the entire inclusion. The lines indicate the importance of bonding when measuring stresses in the elastic regime, as indicated by the departures from the desired value of unity for  $-\sigma_y/p_y$ .

### 3.6 SEPARATION AT THE INTERFACE

By examining Equation (5) for the unbonded interface, we have seen that separation can occur at the interface. In this section, we present the separation conditions for the bonded and unbonded interfaces with no tensile strength.

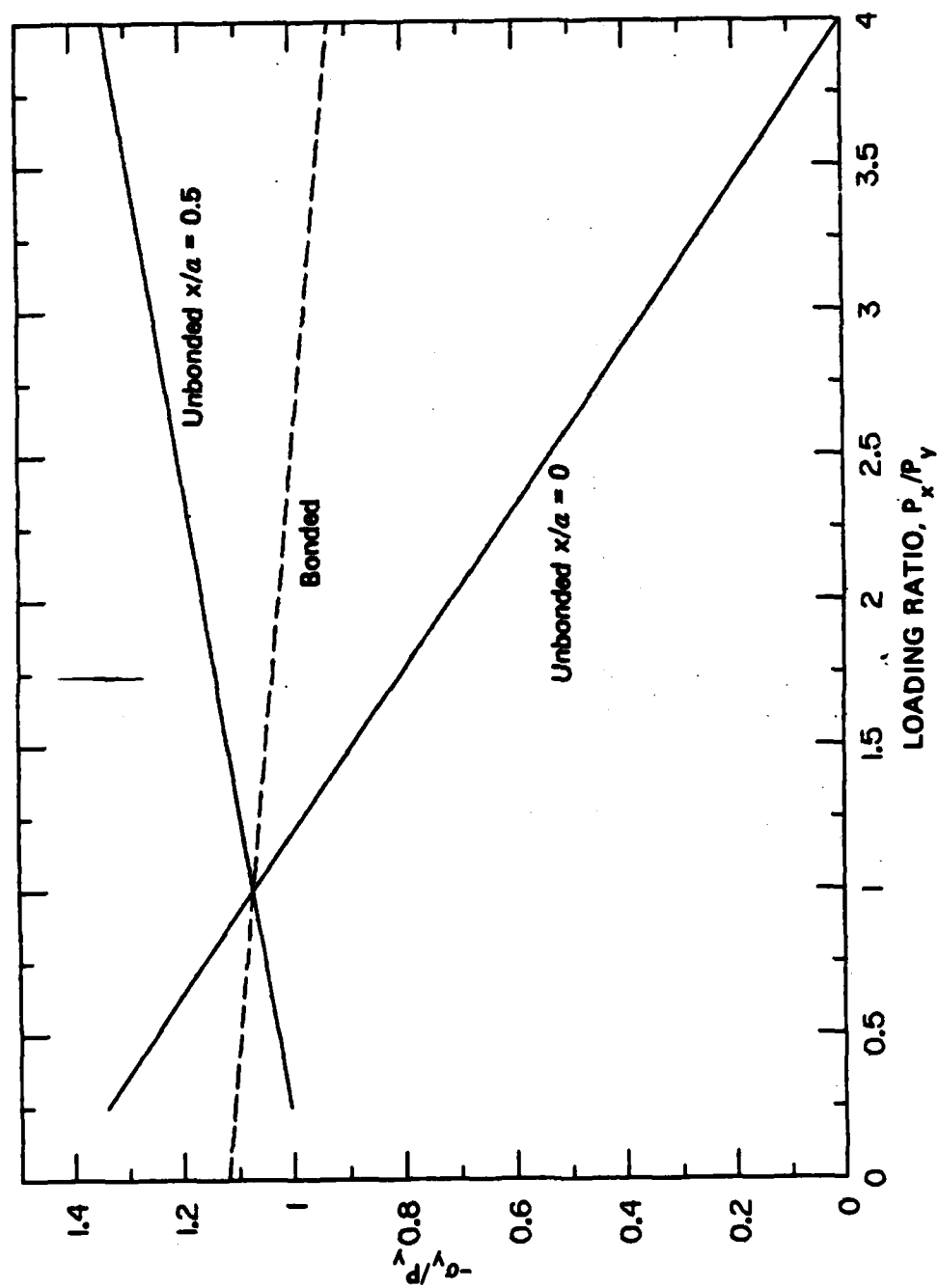
The radial component of stress is

$$\sigma_r = -\frac{1}{2} (p_x + p_y) \beta - \frac{1}{2} (p_x - p_y) \delta \cos 2\theta \quad (6)$$



JA-5877-30

Figure 20. Stress in unbonded 2C4 grout circular inclusion in tuff (properties in Table 1;  $\mu_1/\mu_2 = 1.63$ ).



JA-5877-31

Figure 21. Stresses in bonded and unbonded circular inclusions of 2C4 grout in tuff (properties in Table 1;  $\mu_1/\mu_2 = 1.63$ ).

where

$$\beta = \frac{\alpha k_2}{k_1 + 2(\alpha - 1)} \quad (\text{bonded or unbonded})$$

$$\delta = \frac{\alpha k_2}{\alpha k_2 - (\alpha - 1)} \quad (\text{bonded})$$

or

$$\delta = \frac{6\alpha k_2}{k_1 + 3\alpha k_2 - 2(\alpha - 1)} \quad (\text{unbonded})$$

where  $\alpha = \mu_1/\mu_2$ ,  $k_1 = 4(1 - \nu_1)$ , and  $k_2 = 4(1 - \nu_2)$ . Separation occurs at  $\theta = 0^\circ, \pi$  when

$$\frac{p_y}{p_x} > \frac{\delta + \beta}{\delta - \beta} \quad (7a)$$

and at  $\theta = \pi/2, 3\pi/2$  when

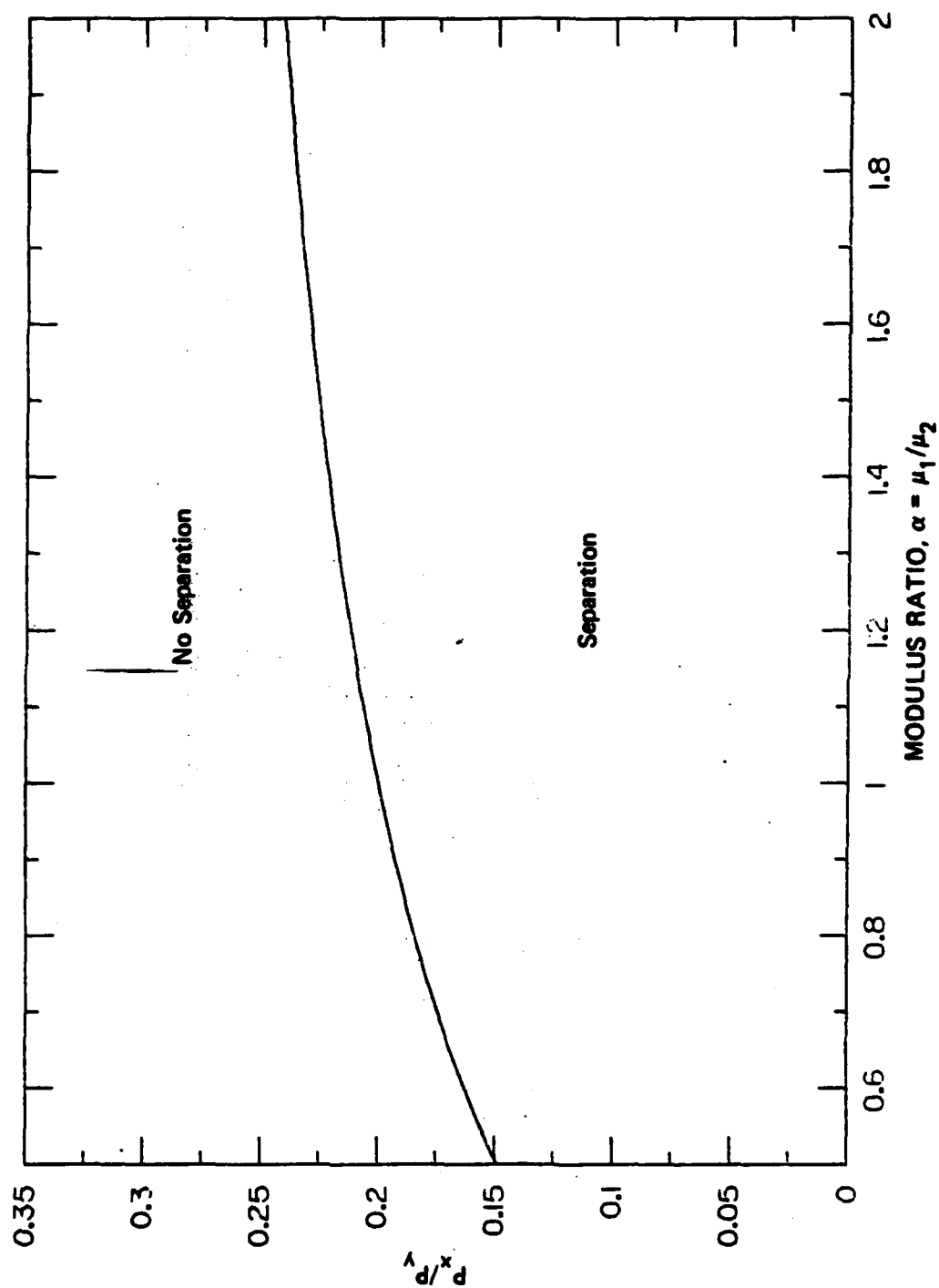
$$\frac{p_y}{p_x} < \frac{\delta - \beta}{\delta + \beta} \quad (7b)$$

To illustrate the influence of the shear modulus ratio  $\alpha$ , we have chosen  $\nu_1 = \nu_2 = 0.3$  and have plotted Equations (7a) and (7b) as equalities in Figure 22(a)-(d). The curves then give the values of the loading ratio  $p_y/p_x$  that cause separation.

### 3.7 RESIDUAL STRESS IN A BONDED CIRCULAR INCLUSION

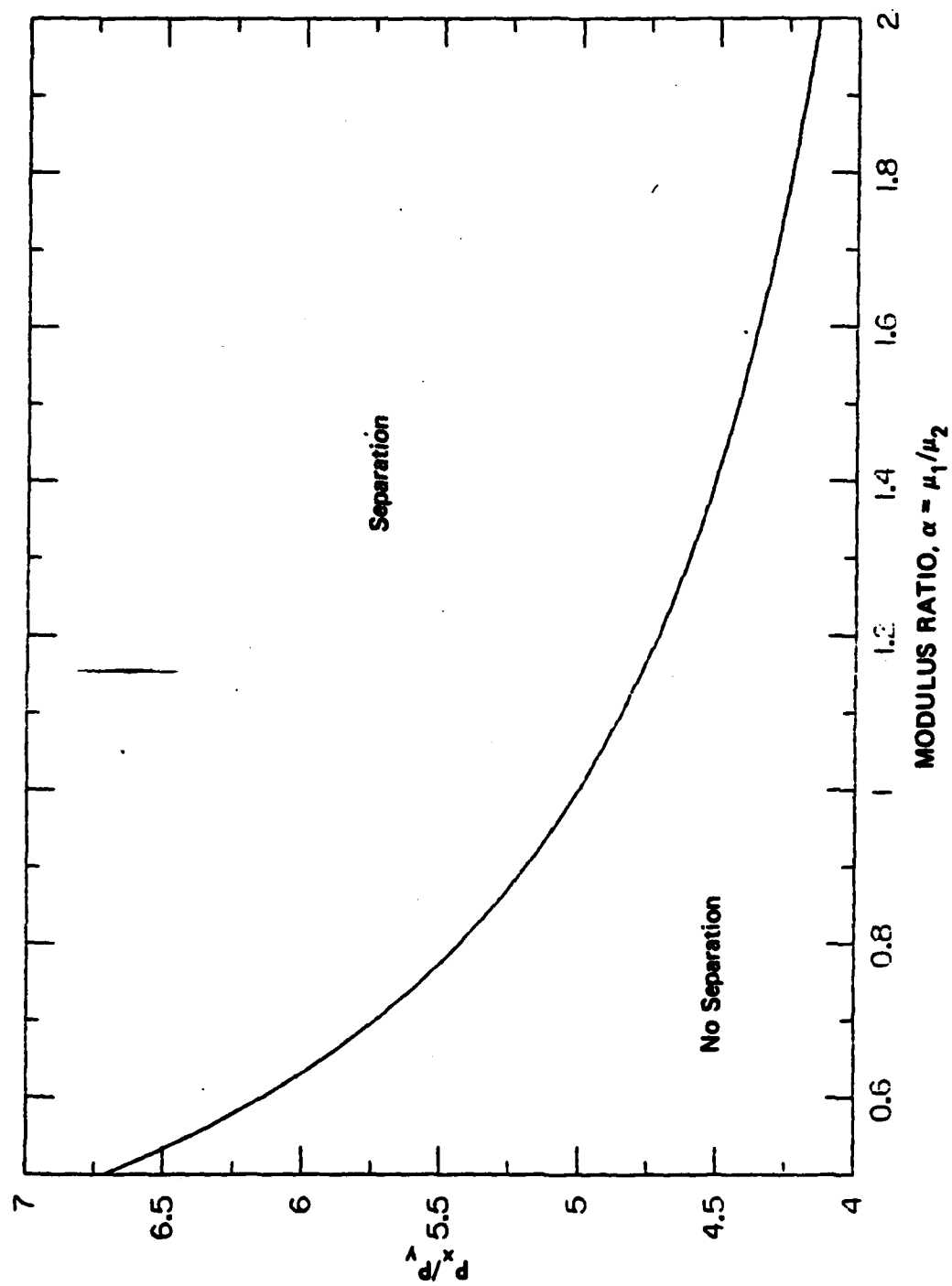
When the stresses are high enough to cause plastic deformation in the inclusion, stresses remain in and around the inclusion after unloading. In the case of the borehole fill inclusion, a stress gage will therefore record stress even after the loading from the stress wave has passed. If the residual stress acting on a flatpack is compressive, the signal will not return to the baseline.

We have performed a residual stress analysis for the case of an elliptic inclusion under plane strain conditions subject to the



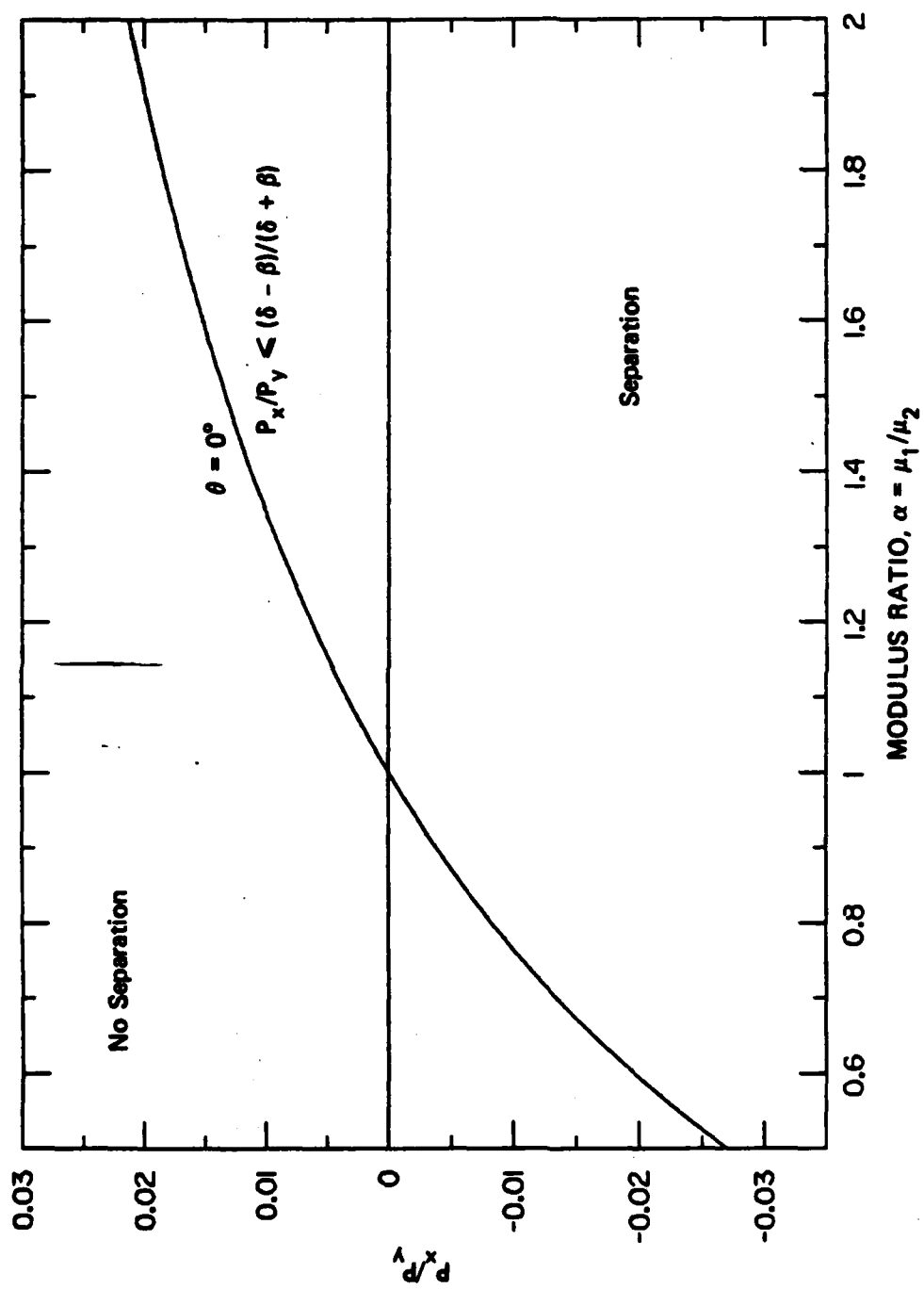
JA-6877-32

Figure 22a. Unbonded circular inclusion separation conditions at  $\theta = 0^\circ$  ( $\nu_1 = \nu_2 = 0.3$ ).



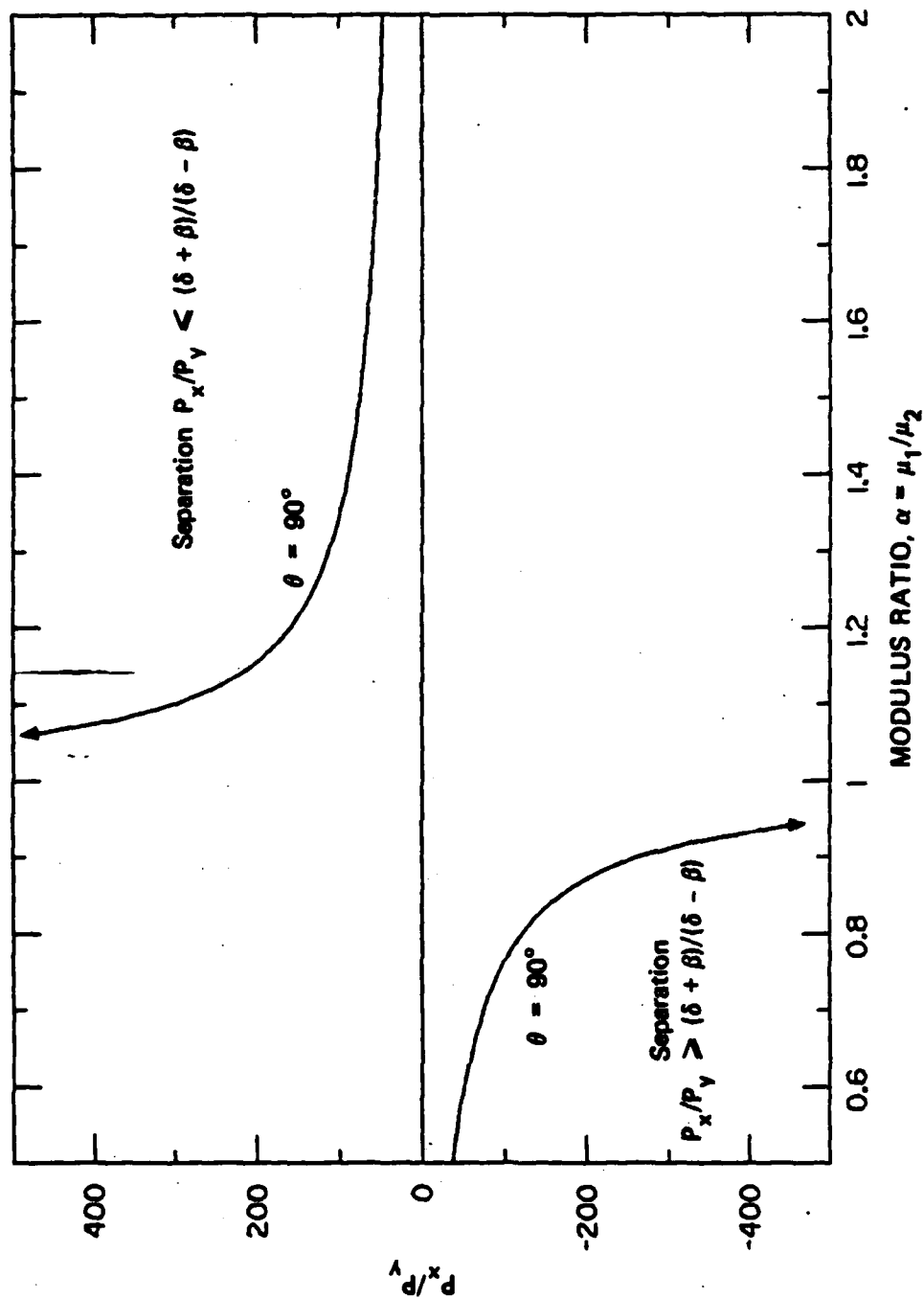
JA-8877-33

Figure 22b. Unbonded circular inclusion separation conditions at  $\theta = 90^\circ$  ( $\nu_1 = \nu_2 = 0.3$ ).



JA-6877-34

Figure 22c. Bonded circular inclusion separation conditions at  $\theta = 0^\circ$  ( $\nu_1 = \nu_2 = 0.3$ ).



JA-6877-36

Figure 22d. Bonded circular inclusion separation conditions at  $\theta = 90^\circ$  ( $\nu_1 = \nu_2 = 0.3$ ).



following simplifying assumptions:

- The inclusion is elastic-plastic, whereas the medium remains elastic.
- The plastic behavior is governed by the Mohr-Coulomb yield condition and its associated flow rule.
- The loading is proportional ( $p_x = \lambda p_y$ ).
- The inclusion/medium interface is bonded.

We illustrate the results by confining ourselves to the case of a circular borehole fill inclusion with yielding of the grout in accordance with the Tresca condition and the associated flow rule.

The elastic loading creates the inclusion stress field

$$\begin{aligned}\sigma_x &= [1 (1 + \lambda) \beta + (1 - \lambda) \delta] p_y / 2 \\ \sigma_y &= [- (1 + \lambda) \beta - (1 - \lambda) \delta] p_y / 2\end{aligned}\quad (8)$$

where  $\lambda = p_x/p_y$  is the far-field loading ratio, and the elasticity parameters  $\beta$  and  $\delta$  are those of the bonded circular inclusion given in Equation (4). For  $\lambda < 1$ , the appropriate Tresca criterion is

$$\sigma_y - \sigma_x = -\sigma_c \quad (9)$$

where  $\sigma_c > 0$  is the grout crush strength. Substituting the stresses of Equation (8) in Equation (9) gives the yield loading

$$\tilde{p}_y = \sigma_c / (1 - \lambda) \delta \quad (10)$$

We have shown that further loading, which causes plastic flow, creates the inclusion stress field

$$\begin{aligned}\sigma_x &= -\frac{1}{2} (1 + \lambda) \beta p_y + \frac{1}{2} \sigma_c \\ \sigma_y &= -\frac{1}{2} (1 + \lambda) \beta p_y - \frac{1}{2} \sigma_c\end{aligned}\quad (11)$$

in which  $p_y > \tilde{p}_y$ . Let the maximum loading be  $\bar{p}_y$ . Substituting of  $\bar{p}_y$  for  $p_y$  in Equation (11) gives the inclusion stress field  $(\bar{\sigma}_x, \bar{\sigma}_y)$  at maximum loading. Elastic unloading by an amount  $p'_y$  gives the stress reduction  $(\sigma'_x, \sigma'_y)$  given directly by Equation (8). The stresses when the loading is  $\bar{p}_y - p'_y$  are therefore  $\bar{\sigma}_x - \sigma'_x$  and  $\bar{\sigma}_y - \sigma'_y$ . If complete unloading can be performed elastically, we set  $p'_y = \bar{p}_y$  in Equation (8) and subtract the result from Equation (11) to get the residual stresses

$$-\sigma_x = \sigma_y = \left( \frac{\bar{p}_y}{\tilde{p}_y} - 1 \right) \frac{\sigma_c}{2} \quad \tilde{p}_y < \bar{p}_y < 2\tilde{p}_y \quad (12)$$

The upper bound  $2\tilde{p}_y$  on the maximum loading expressed in Equation (12) is required to avoid reverse yielding according to the criterion

$$\sigma_y - \sigma_x = \sigma_c \quad (13)$$

Substitution of Equation (12) in Equation (13) shows that reverse yielding occurs when  $\bar{p}_y > 2\tilde{p}_y$ .

If the maximum loading is greater than twice the yield loading,  $\bar{p}_y > 2\tilde{p}_y$ , the stresses after elastic unloading are

$$\begin{aligned} \sigma_x &= -\frac{1}{2} (1 + \lambda) \beta (\bar{p}_y - 2\tilde{p}_y) - \frac{1}{2} \sigma_c \\ \sigma_y &= -\frac{1}{2} (1 + \lambda) \beta (\bar{p}_y - 2\tilde{p}_y) + \frac{1}{2} \sigma_c \end{aligned}$$

Complete unloading then leads to the simple result

$$-\sigma_x = \sigma_y = \frac{1}{2} \sigma_c \quad 2\tilde{p}_y < \bar{p}_y \quad (14)$$

The residual stresses of Equations (12) and (14) would thus leave two stress gages measuring  $p_x$  and  $p_y$  in compression and tension, respectively. The results of this analysis were used for comparison with our code results in Figure 10 (Section 2).

## SECTION 4

### STATIC CALCULATIONS OF STRESS GAGE INCLUSIONS

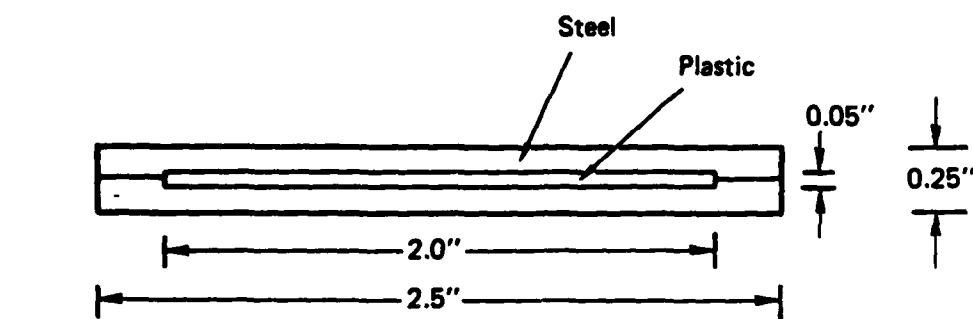
#### 4.1 INTRODUCTION

In this section, we present the results of a finite element calculation for a typical flatpack stress gage embedded in 2C4 grout. The purpose of the calculation is to compare the normal stress experienced by the ytterbium sensing foil to the free-field stress to be measured. Following these calculations is the result of a basic elastic analysis in which the flatpack is idealized as a rigid line. The purpose of the analysis is to examine the influence of the bonding on the stress normal to the line.

The results indicate excellent performance by the flatpack under the static loading, if the ytterbium foil is confined to the central 60% of the flatpack midplane width. The midplane stress was not sensitive to the bonding condition at the steel/grout interface. The idealized line gage analysis indicated that the unbonded condition provided more accurate stress measurement.

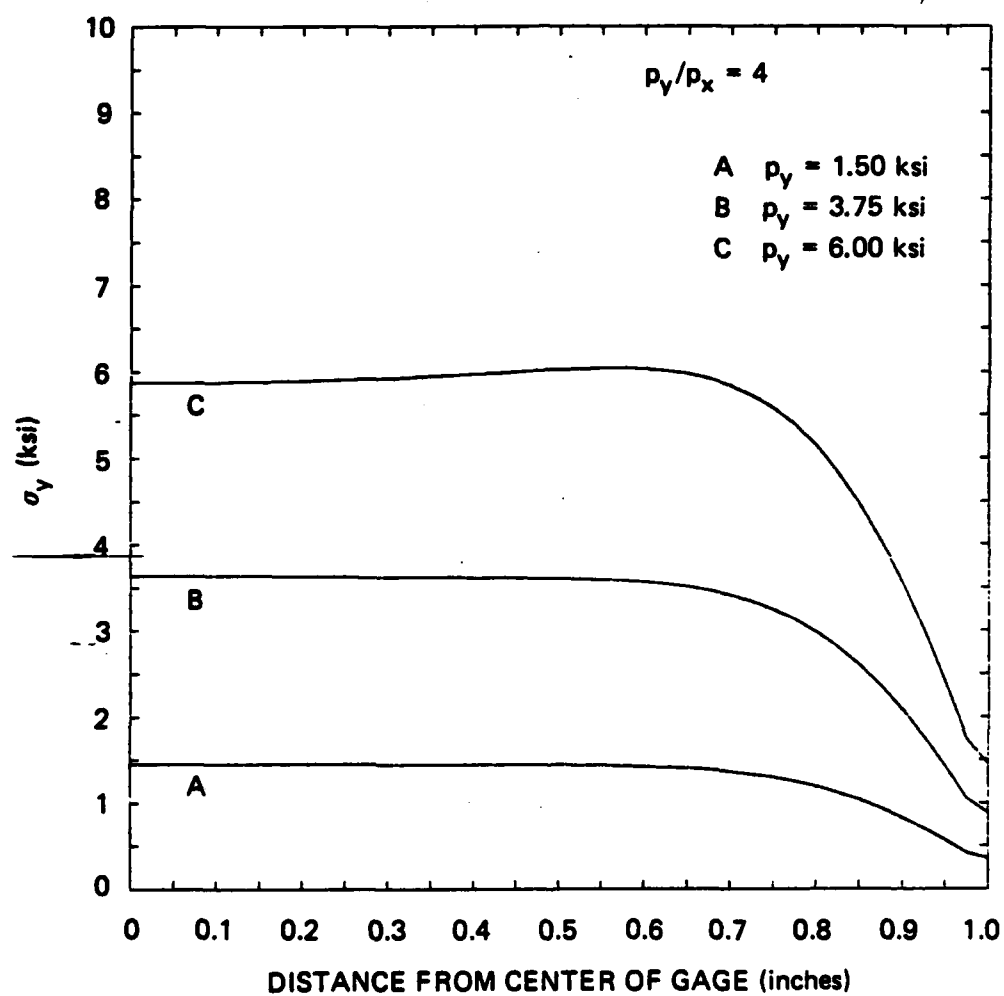
#### 4.2 FLATPACK STRESS GAGE INCLUSION

A cross section through a typical flatpack stress gage is shown in Figure 23. The ytterbium foil sensing element is not shown, but it occupies the midplane. We performed a finite element calculation with the flatpack embedded in 2C4 grout and subjected to free-field stresses  $\sigma_x = -p_x$  and  $\sigma_y = -p_y$  of increasing levels while keeping the ratio constant at  $p_y/p_x = 4$ . Plane strain conditions are imposed. The result of interest is a comparison of the stress  $\sigma_y$  at the midplane in the plastic, which is the stress the ytterbium foil measures, and that of the free-field compressive stress  $p_y$ . Figure 24 shows the midplane stress distributions for three different free-field stress levels--A, B, and C. Accuracy is obtained if the ytterbium foil does not occupy more than the central 60% of the midplane.



JA-5877-40

Figure 23. The flatpack stress gage.



JA-5877-39

Figure 24. Stress along the gage plane for a gage package bonded in a grout media.

### 4.3 LINE INCLUSION

As an initial investigation into the effect on the measured stress of the bonding of a flatpack stress gage with the surrounding medium, we have idealized the thin steel strip in two different ways. In both cases, we have replaced the gage cross section by a line of finite length. In one case, the line is unbonded to the medium and supports no shear traction along the surface. In the other case, the line is inextensible and bonded to the medium.

Figure 25 shows the two line problems that we solved using the method of linear relationship described by Muskhelishvili.<sup>6</sup> Only the solutions for the stress,  $\sigma_y$ , normal to the line will be given here.

When the line is unbonded and we essentially have a slot under compression that sustains no shear traction, we obtain the stress normal to the line as

$$\sigma_y = -\frac{1}{2} (p_1 + p_2) + \frac{1}{2} (p_1 - p_2) \cos 2\theta \quad (15)$$

where  $\theta$  is the angle between the direction of  $-p_1$  in the first quadrant and the x axis (see Figure 25). When  $\theta = 0$ ,  $\sigma_y = -p_2 = -p_y$ . Equation (15) is exactly the y component of stress in the far field; hence if the gage is a perfectly lubricated line, we obtain the correct reading.

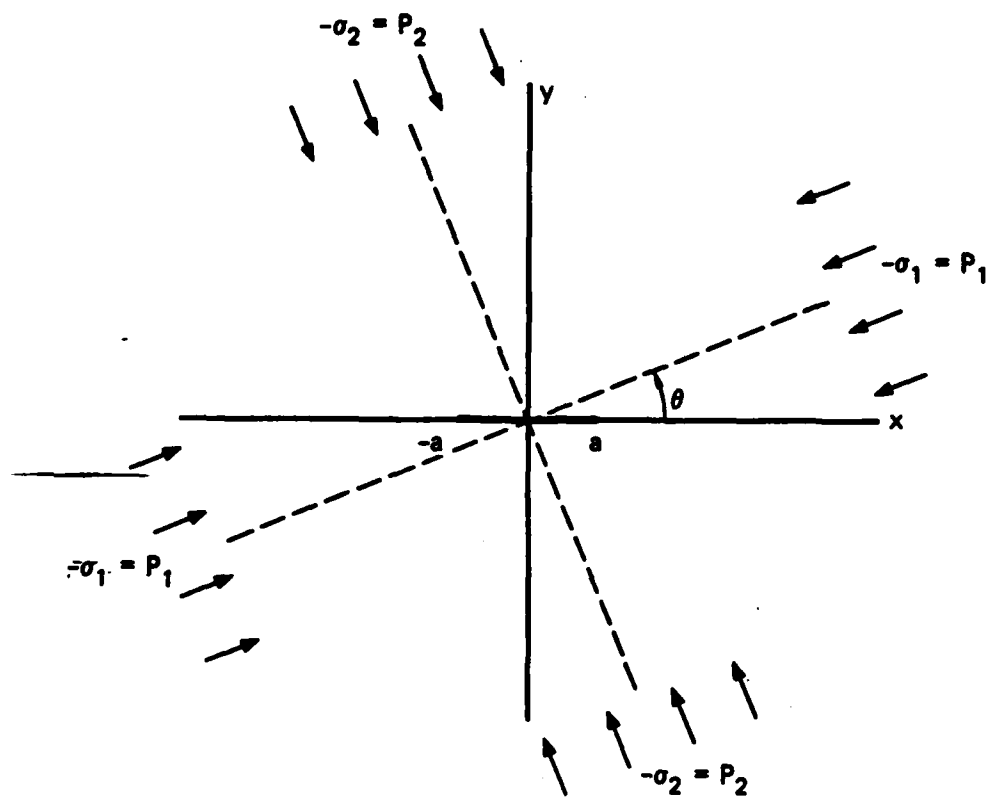
When the line is inextensible and bonded to the medium, we obtain the stress normal to the line as

$$\sigma_y = -\frac{\kappa + 1}{2\kappa} \left[ \frac{\kappa + 1}{2} \frac{1}{2} (p_1 + p_2) - \frac{1}{2} (p_1 - p_2) \cos 2\theta \right] \quad (16)$$

where  $\kappa = 3 - 4\nu$ ,  $\nu$  being Poisson's ratio for the medium. When  $\theta = 0$ ,

$$\sigma_y = -\frac{\kappa + 1}{8\kappa} [(\kappa - 1) p_x + (\kappa + 3) p_y] \quad (17)$$

so  $\sigma_y \neq -p_y$ . Equations (16) and (17) do not give a normal stress equal to the far-field stress to be measured. The normal stress is influenced by the Poisson's ratio for the medium and the loading ratio  $p_x/p_y$ . From



JA-5877-36

Figure 25. Line idealization of flatpack stress gage.

Equation (17), estimates of the measurement error can be obtained if we examine the two numerical examples:

$$v = 1/4 \quad (\kappa = 2) \quad - \frac{\sigma_y}{p_y} = \frac{3}{16} \left( 5 + \frac{p_x}{p_y} \right)$$

$$v = 1/3 \quad (\kappa = 5/3) \quad - \frac{\sigma_y}{p_y} = \frac{1}{15} \left( 14 + 2 \frac{p_x}{p_y} \right)$$

If  $p_x/p_y < 1$ , the errors are acceptable.

Although the gage compliance is omitted from the initial considerations, the indications are that slip on the gage faces should be encouraged.



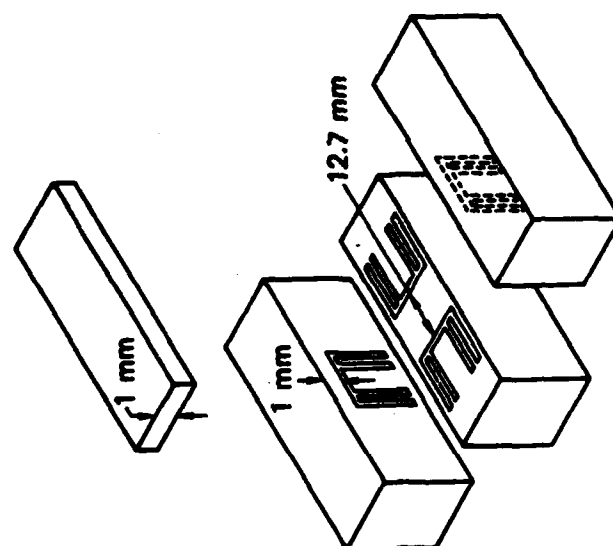
## SECTION 5

### NUMERICAL SIMULATION OF THE DYNAMIC RESPONSE OF A FOIL INCLUSION

#### 5.1 INTRODUCTION

We have numerically simulated the response of a thin foil ytterbium gage in a PMMA matrix subjected to a shock wave. Figure 26 shows the configuration of experiments performed by Y. M. Gupta.<sup>7</sup> The matrix is composed of four parts: a 1-mm cover plate, two side pieces, and a bottom piece. The shock wave is induced by a 3-mm-thick flyer plate that impacts the cover plate. Four foils are embedded in the PMMA: two with the foil plane parallel to the shock front and two with planes perpendicular to the shock front. The present discussion concerns one of the foils that is parallel to the shock front. Figure 27 shows details of the ytterbium foil.

A peak shock wave stress in the PMMA of 8.5 kbar is induced by the flyer plate. The tool for modeling the gage-matrix interaction is a two-dimensional code; thus, we must reduce the problem to a plane symmetry case. This is done by assuming that the distance between the legs of the foil is large compared with the foil width and the pulse length. Figure 28 shows the area modeled in the computation. The interface between the foil and the matrix is a slide line with no friction. Separation of the foil and matrix is allowed to occur. The left boundary is at the center of the foil width and forms a symmetry boundary. The right boundary of the matrix will be a symmetry boundary until reflected signals from the gage reach the boundary. The right boundary is modeled as a symmetry boundary all through the calculation. This right boundary is considered far enough from the foil for the foil stresses to be negligibly affected by the assumption of symmetry. The lower boundary is modeled as a continuum boundary. The mathematical model in the code for a continuum boundary is not exact, but it gives a small reflection for a plane shock wave at normal incidence. Note that



JA-5877-8

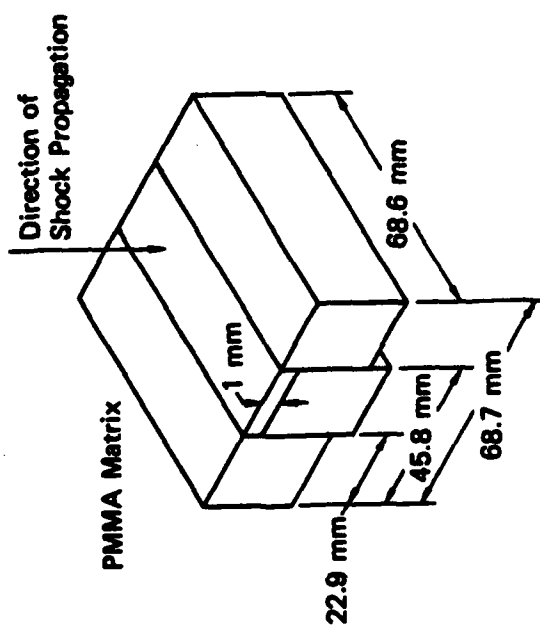


Figure 28. PMMA matrix and blow-ups showing the gage positions.

Yb Gage

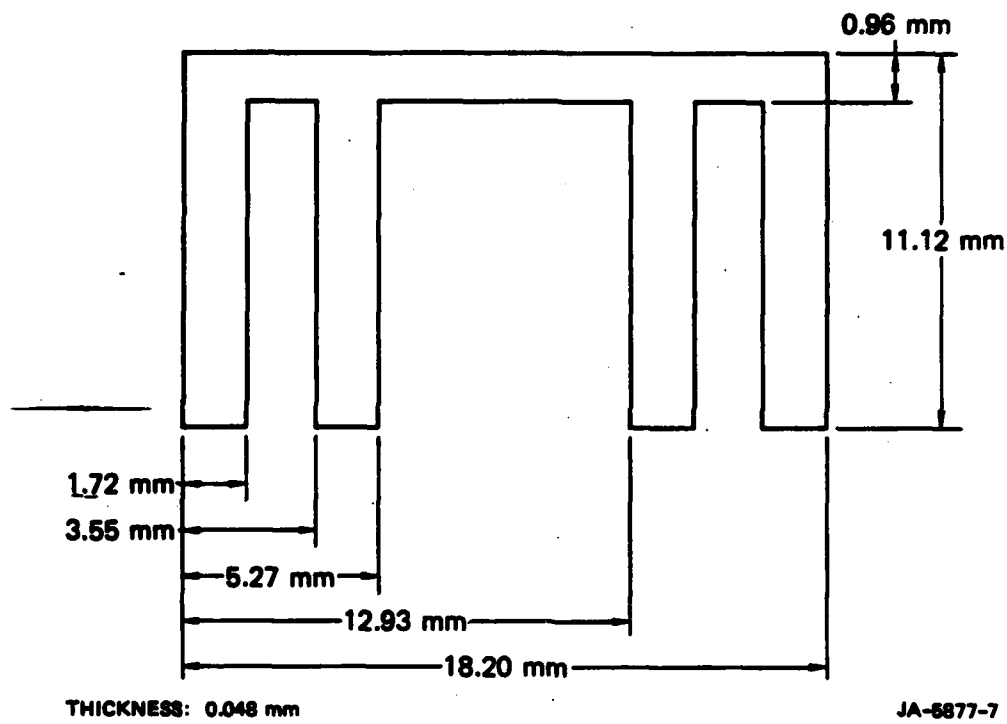
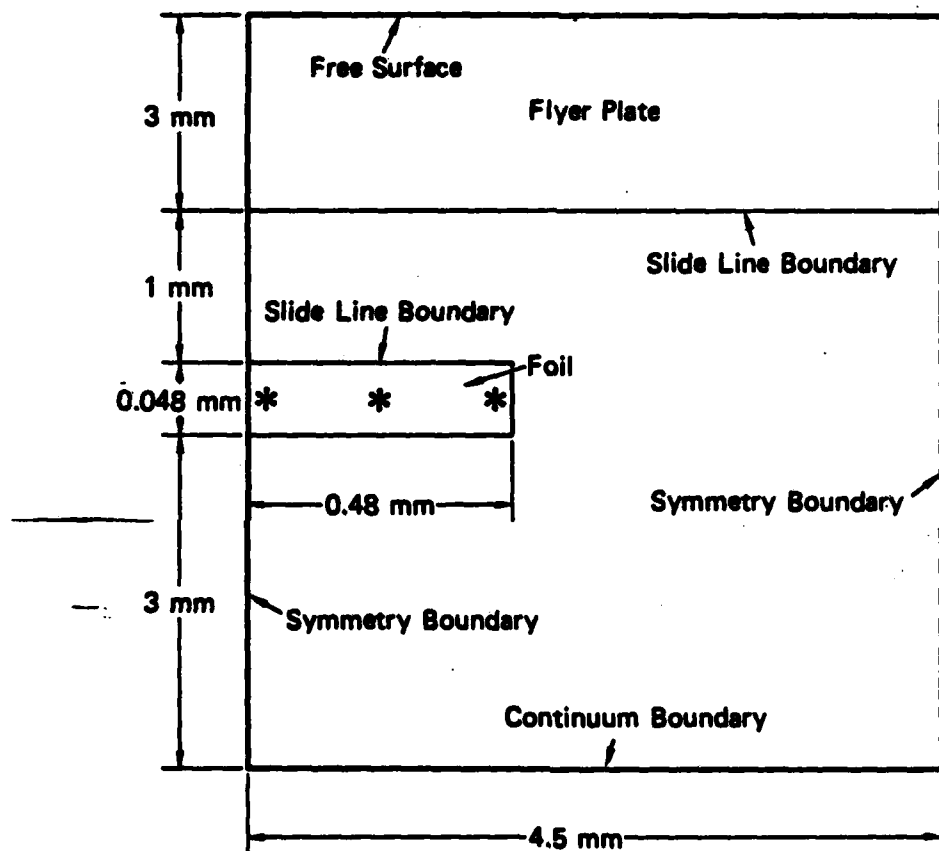


Figure 27. Ytterbium gage foil.



JA-5877-8

Figure 28. Area modeled in the computation.

the signals from both the right and lower boundaries arrive at the gage later than the rarefaction from the top, and therefore do not influence the foil response. The interface between the target and the flyer plate is a slide line with no friction. Finally, the top flyer-plate boundary is a free surface and is modeled as such.

Figure 29 shows the mesh in the neighborhood of the gage. The difference in cell size between the ytterbium and the PMMA should give a correct impedance match of the materials.

## 5.2 MATERIAL MODELS

The constitutive model for PMMA is

$$P = K_1 \mu + K_2 \mu^2 + (\gamma - 1)E \rho \quad (18a)$$

where

$P$  = pressure

$\mu = \rho/\rho_0 - 1$

$\rho$  = density ( $\rho_0$  = initial density)

$K_1 = 0.07243$  Mbar

$K_2 = 0.17515$  Mbar

$E$  = internal energy density

$\gamma = 2.0$

and

$$\dot{s}_{ij} = 2 G \dot{e}_{ij} \quad (18b)$$

where

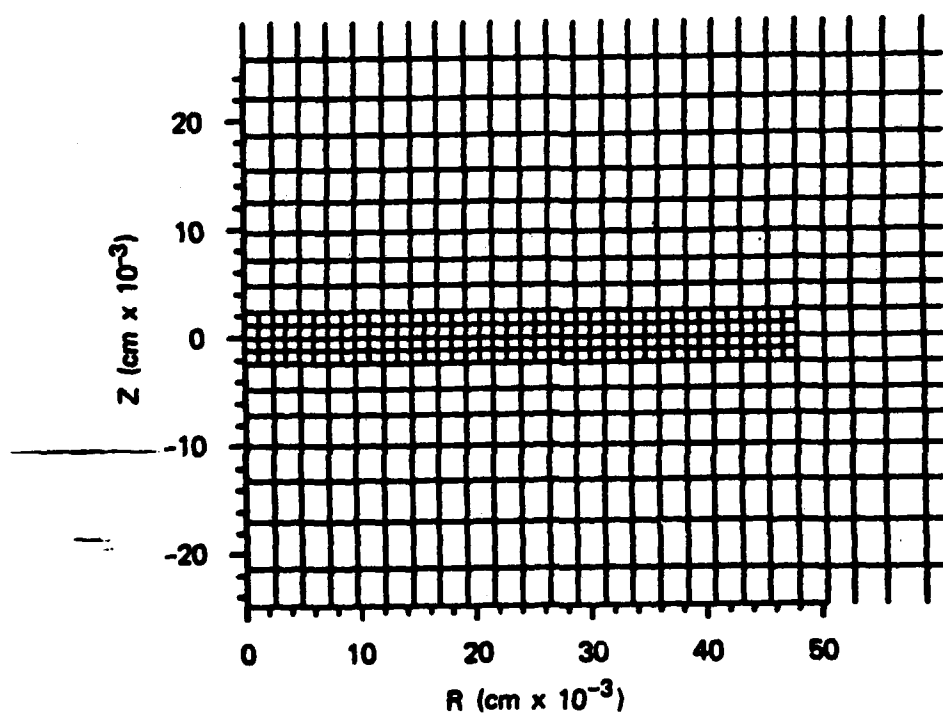
$\dot{s}$  = stress deviator rate

$\dot{e}$  = strain deviator rate

Shear modulus  $G = 0.025$  Mbar

Von Mises yield model with  $Y_0 = 0.0045$  Mbar

Initial density  $\rho_0 = 1.184$  g/cm<sup>3</sup>.



JA-5877-9

Figure 29. Mesh in the neighborhood of the foil.

Some uncertainty exists about the proper yield value of PMMA. It seems reasonable to believe that the present value is somewhat too high. Gupta has obtained the stress deviator in the shock wave direction versus pressure for a uniaxial strain experiment.<sup>8</sup> The stress deviator peaks at 2 kbar for a pressure of 7 kbar and then decreases because of strain softening. If we assume that the material yields at that point, a simple calculation shows that the yield value is 3 kbar.

The constitutive model for ytterbium obtained from Gupta has a different form than the one for PMMA. The PMMA yield model refers the yield value to the yield in simple tension as opposed to the model for ytterbium, which refers yield to the second invariant. The conversion factor is  $3^{0.5}$ . The ytterbium model was converted to the form for PMMA using  $\gamma = 2.0$ ,  $K_1 = 0.148$  Mbar,  $K_2 = 0.0$ , and an initial density of  $6.98 \text{ g/cm}^3$ . The stress-strain deviator relationship is similar with a shear modulus of 0.0725 Mbar, but the flow rule is different:

$$(I_2')^{0.5} - Y_0 - ME^P \leq 0$$

where

$$\begin{aligned} I_2' &= 0.5 s_{ij} s_{ij} \\ E^P &= (0.5 \epsilon_{ij}^P \epsilon_{ij}^P)^{0.5} \\ \epsilon_{ij}^P &= \text{component of the plastic strain} \\ Y_0 &= 0.000473 \text{ Mbar} \\ M &= 0.00454 \text{ Mbar.} \end{aligned}$$

The piezoresistant model for ytterbium is given by Gupta.<sup>9</sup> After specializing to the present symmetry, we have

$$R_s = R_{s_0} + R_{s_0} (A_3 P + B_2 \sigma_{tt} + \eta E^P) \quad (19)$$

where

$$R_{s_0} = \text{initial resistivity}$$

- $P$  = pressure  
 $\sigma_{tt}$  = stress in the direction normal to the plane of symmetry  
 $E^P$  = square root of the second invariant of plastic strain  
 $A$  = 7.84 per Mbar  
 $B$  = 16.43 per Mbar  
 $\eta$  = 1.13 dimensionless.

The resistance (per unit length) for a single cell is  $R = R_s/A_c$ , where  $A_c$  = current area of cell. Similarly, the initial resistance is  $R_0 = R_{s0}/A_0$ . We note that  $E^P$  in Equation (19) represents contributions from the increase in defects and the like; dimensional changes are accounted for by the area term in the formula for the resistance. For the plane symmetry assumed here, Kirchhoff's formula for the summation of parallel resistance is valid (see Appendix):  $1/R = 1/R_1 + 1/R_2 \dots + 1/R_n$ . Assuming  $R_{s0}$  to be the same for all the cells, we obtain after some algebraic manipulations, the following formula for the relative resistance change due to the total cross section change of the ytterbium foil:

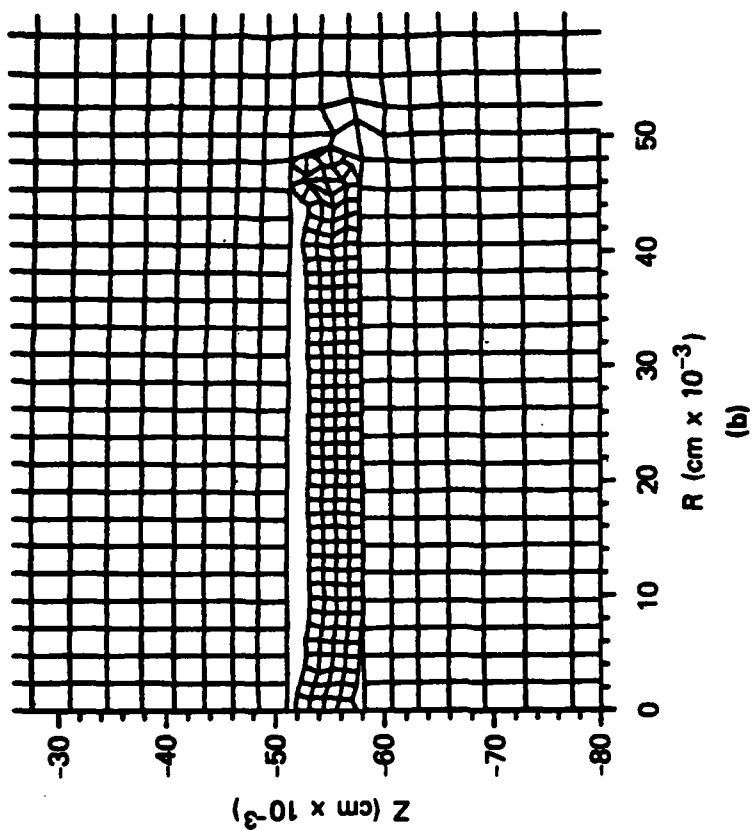
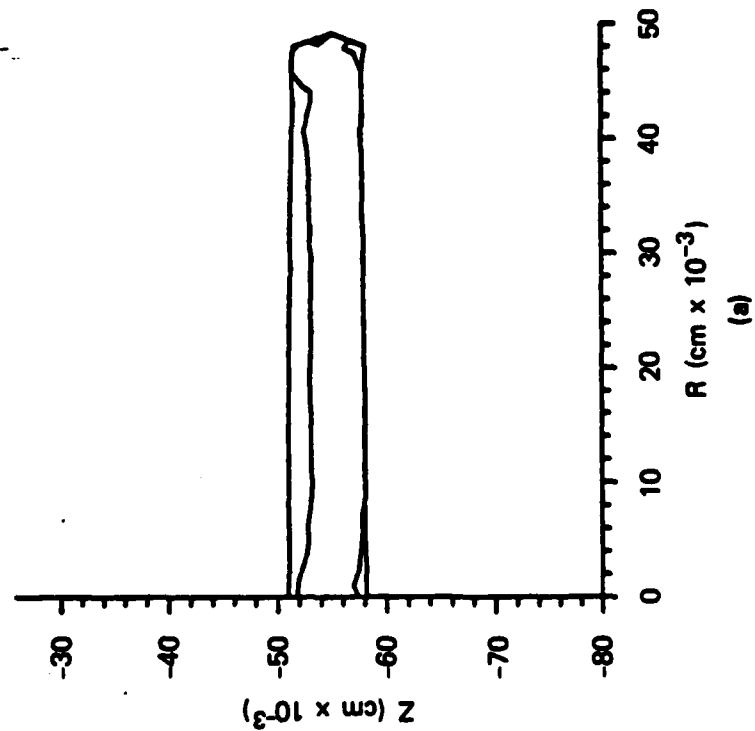
$$(R - R_0)/R_0 = \Sigma A_0 / \{ \Sigma (A_c / Fr) \} - 1 \quad (20)$$

Where  $\Sigma$  stands for summation over the cells, and  $Fr = R_s/R_{s0}$ . It is unnecessary to express the dimensional changes with strains because the cell area is directly available in the code calculation. Also, it is not necessary to know the initial resistivity.

### 5.3 RESULTS

The simulation was performed to 3.38  $\mu s$ . The rarefaction from the top of the flyer plate arrives at about 2  $\mu s$ . The stresses have in no way equilibrated (i.e., generally gone to zero) when the calculation stops, but they have decreased nearly two orders of magnitude compared with the initial shock wave stress of 8.5 kbar. Figure 30 shows the





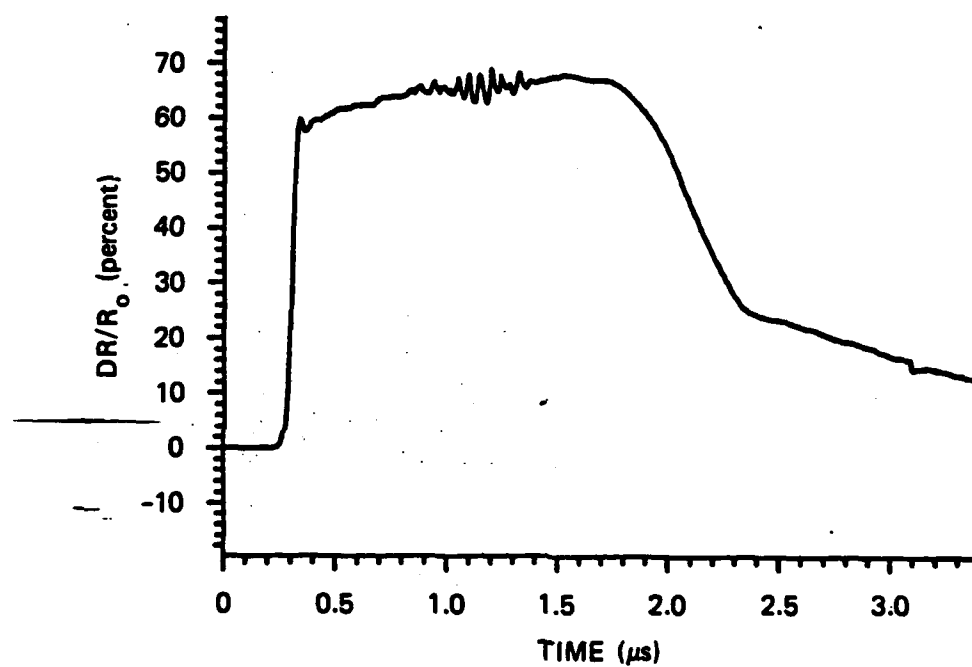
JA-6877-10

Figure 30. Material boundaries (left) and mesh (right) around the foil at 3.38  $\mu$ s.

material boundaries and mesh around the foil at 3.38  $\mu$ s. The gage has separated from the matrix material because the inclusion area in the matrix is larger than it was initially. To see why this happens, it is necessary to consider the motion when the initial shock wave hits the gage. The ytterbium is about six times denser than the PMMA. This density ratio means that the particle motion of the matrix material above the gage decreases, producing a bend in the matrix. No separation appears at this time because the material below the gage and the gage itself expand to fill the void as a result of overpressures. If the yield strength of the matrix is low enough, the material above the gage and immediately to the right will deform plastically, and the deformation will be frozen in when the stresses are removed. This qualitative analysis appears reasonable, considering that the yield stress of PMMA is 4.5 kbar and the shock wave stress is 8.5 kbar.

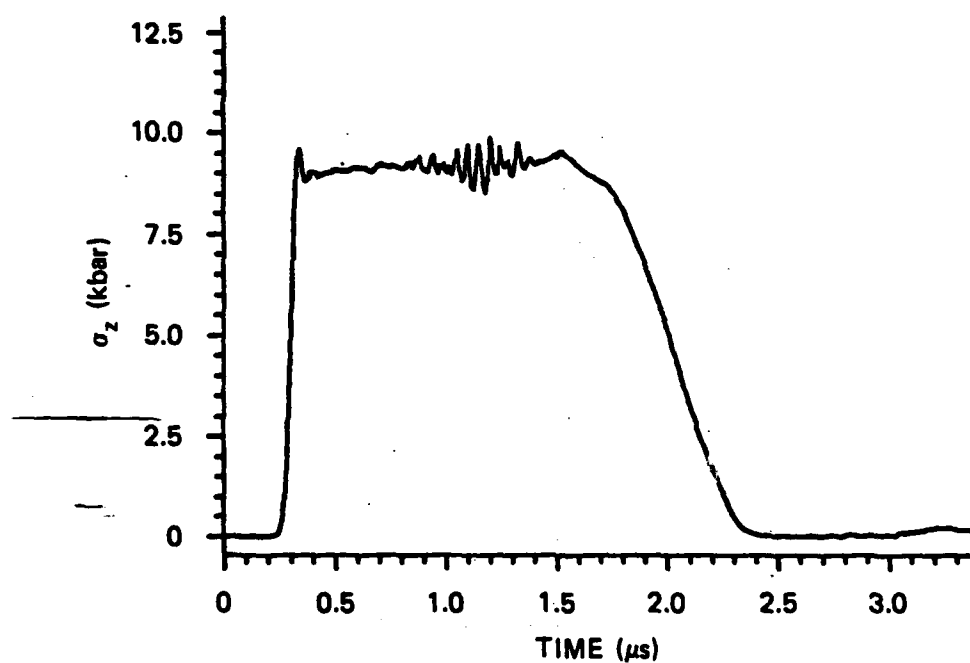
To study separation and shear at the interface between the foil and the matrix, we followed the motion of interface nodes that were at the center part of the foil. The nodes were initially in the same position: one pair on the upper interface and one pair on the lower interface. The results indicate that no significant separation or shear occurred until the stresses started to relax.

We have sampled Lagrangian time histories for the whole ytterbium foil and three single cells (marked with an asterisk in Figure 28) in the foil. For the whole foil, all quantities except the relative resistance change are averaged without weighing. The relative resistance change is calculated with Equation (20). Figure 31 shows relative resistance change versus time for the whole foil. The peak value is 68%, and the residual at 3.38  $\mu$ s is 14%. The experimental values (from uniaxial strain data) are 75% and 15%, respectively. Figure 32 shows stress in the z direction for the whole foil versus time. From the three single cell histories, it is clear that the residual resistance varies significantly between the cells, whereas the z stress is almost zero, as for the whole foil. The resistance curve in Figure 31 is therefore not typical for the individual parts of the foil.



JA-5877-11

Figure 31. Relative resistance change for the foil versus time.



JA-5877-12

Figure 32. Z stress versus time (average for the foil).

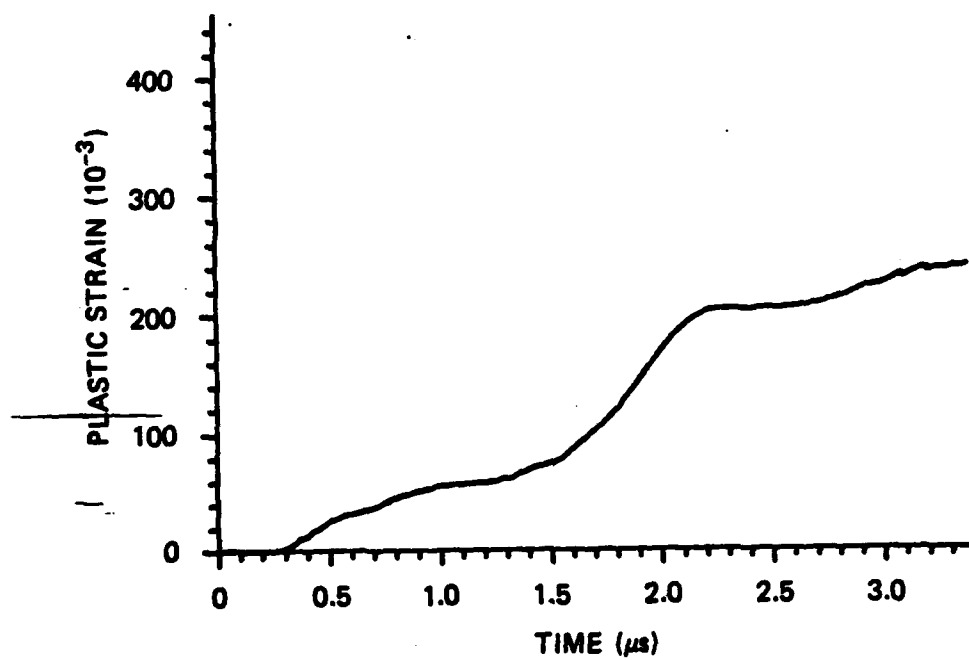
In particular, the right end of the foil has a wildly varying resistance. This is due to the large amount of plastic deformation caused by the complex stress state there.

#### 5.4 DISCUSSION

There are several reasons for the differences in resistance change at peak and unloading between computation and experiment. Possible sources of errors are constitutive models (for ytterbium and PMMA) and the resistivity model of Equation (19); that is, the constants in the models or the models themselves may be in error. A significant difference appears to be due to the plastic strain term in Equation (19). Figure 33 shows average  $E^P$  for the foil versus time. The final value is 0.24; the relative resistance change is 14%. With  $\eta = 1.13$  in Equation (19), one would expect a residual of about 27%. This disagreement is explained by a residual change in the cross section area.

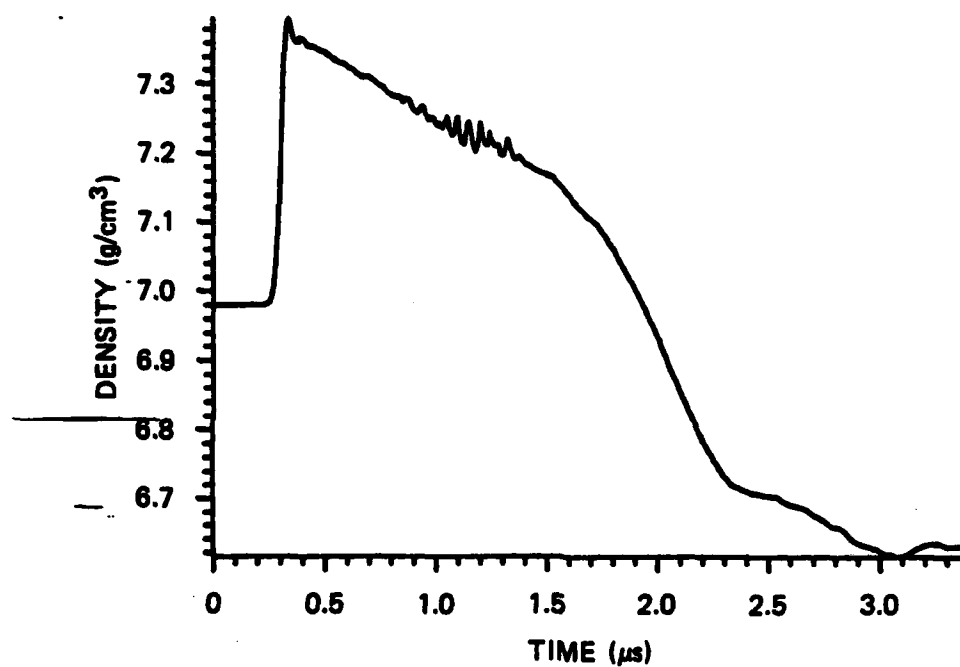
Figure 34 presents average density for the foil versus time. As shown, a net expansion of about 7% is obtained, which for our plane symmetry implies the same increase in area. A certain residual stress also exists, but the main effect comes from the residual in the area. Using the resistivity formula (19), we can calculate the relative resistivity  $F_r = R_s/R_{s0} = 1 + n * E_p = 1 + 1.13 * 0.24 = 1.27$ , where the stresses are assumed to be zero. The relative resistance change for the foil is from (20)  $(R - R_0)/R_0 = A_0/(A_c/F_r) - 1 = 1/1.07 * 1.27 - 1 = 19\%$ . This does not agree with the above value of 14% that was calculated by using electrical circuit theorems viewing each cell as an electrical wire; however, this lack of agreement is reasonable because the use of average values is simply not accurate. It must be noted that the plastic strain, and thereby the resistivity, varied considerably along the cross section of the foil.

More troublesome is the comparatively large increase in cross section area. From the pressure relationship [Equation (18a)], it is clear that a 7% increase in area would generate a tension of several kilobars, which is not found in the actual calculation. Originally, it



JA-5877-13

Figure 33. Plastic strain versus time (average for the foil).



JA-5877-14

Figure 34. Density versus time (average for the foil).

was assumed that this could be explained by the internal energy term in Equation (18a)—that is, the internal energy increases as a result of the plastic work; however, a hand calculation shows that the internal energy is at least one order of magnitude too small. The reason for this discrepancy is not clear. One possible explanation is that the increase in area cannot be reliably estimated by calculating the average density. A similar point may then hold for our calculation of 0.24 for the average plastic strain. Future calculations will address this problem.

The plastic strain, as currently defined, does not necessarily increase monotonically. The average plastic strain in Figure 30 is monotonic, but this is not true for a single cell. The plastic strain component in Equation (19) includes a contribution from defect production in the material. One expects the number of defects to increase monotonically independent of the direction of the deformation. Both plastic work and Hill's definition of equivalent plastic strain are strictly monotonic. After completing our calculations, we found that Gupta does indeed use Hill's definition for deriving the plastic strain coefficient  $\eta$  in (19). We will use Hill's definition of equivalent plastic strain in future calculations.

## 5.5 CONCLUSIONS

The calculation showed reasonable agreement with experiment. The calculated relative resistance change peaked at 68% versus 75% for the experimentally observed change. The residual was 14% by calculating and 15% by experimental observation.

The residual resistance increase depends not only on the plastic term in Equation (19), but also on a permanent increase in the area of cross section of the foil.



## SECTION 6

### EXPERIMENTAL INVESTIGATIONS

#### 6.1 INTRODUCTION

The experimental investigations address the effects on stress measurement of the inclusions formed by the stress gage package and by the borehole fill. Two types of experiments are envisaged: (1) static triaxial loading of a block of geologic simulant, with and without a borehole, and (2) dynamic uniaxial strain loading of matrices containing gage packages. They will provide known free-field stresses for comparison with gage measurements. They are also designed to provide results for comparison with theoretical predictions so that the mechanics of stress measurement can be studied.

We have designed, constructed, and proof-tested the apparatus for the static experiments. Rather than proceed with experiments to show the effect of borehole fill, we have examined sensors suitable for providing experimental results, such as slip at borehole fill/media interfaces. This work is discussed in Section 6.3.

The design of the dynamic experiment is the result of calculations to determine the feasibility of using a 4-inch-diameter gas gun and reduced-scale flatpack gages to investigate the relationship between free-field and gage stresses. We found that gage-medium equilibrium could not be achieved during pulse durations obtainable from 4-inch-diameter gas gun flyer plates unless the steel armor of the gage were reduced to very thin foils. Because this reduction would alter gage response, we concluded that longer pulses than are achievable in the 4-inch-diameter gas gun would be required. An experiment that fulfills the requirements is described in Section 6.4.

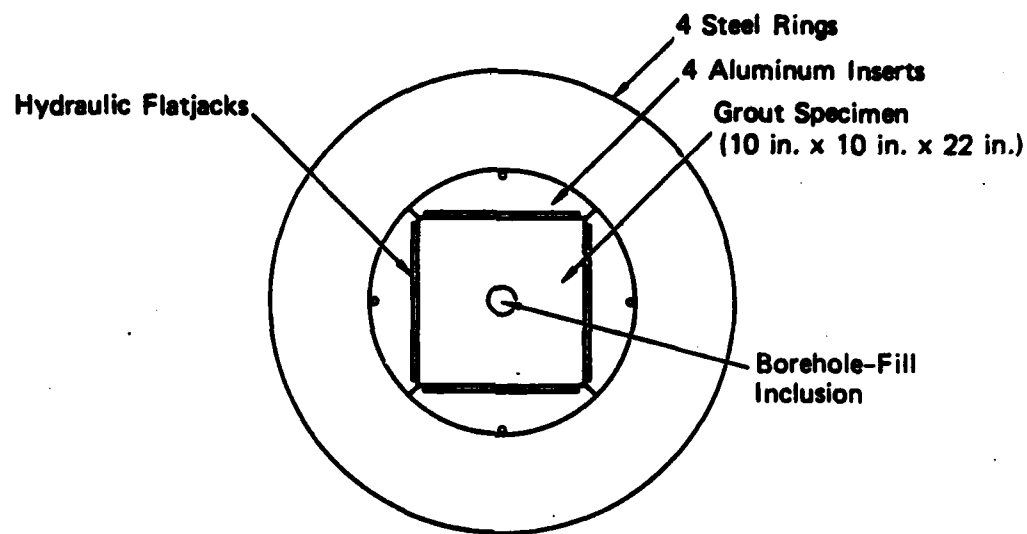
## 6.2 STATIC EXPERIMENTS

Figure 35 shows the experimental apparatus designed to apply a general triaxial stress field to a rectangular block of geologic material or rock simulant. The block (10 x 10 x 22 inches) is confined by inserts within a pressure vessel. The pressure is applied by three pairs of flatjacks on the faces of the block, each pair applying the same pressure. As shown, the block can have a central borehole fill inclusion (2 inches in diameter). The apparatus is designed for a maximum pressure difference of 0.5 kbar and a hydrostatic pressure of 1 kbar. It can also provide plane strain loading for correlation of results with the theoretical predictions of the finite-element technique. The hydraulic system was tested to 2000 psi on a block of rock simulant. Flaws in the flatjack manufacture were corrected.

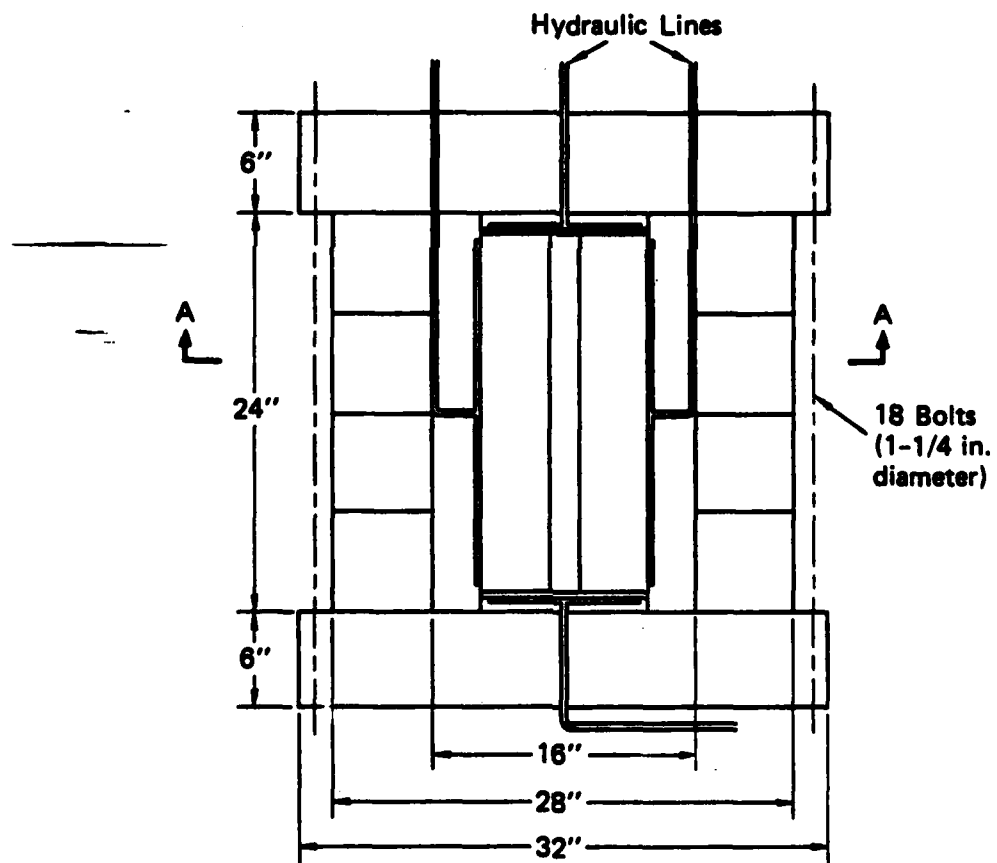
Three basic experiments are planned with rock simulant blocks: (1) no borehole, (2) borehole with unbonded grout fill, and (3) borehole with bonded grout fill. We are currently experimenting with miniature stress and strain gages suitable for embedding in grout while minimizing the inclusion effects of the gages themselves. Sensing elements in thin fluid packages appear to be suitable candidate gages.

## 6.3 GAGE DEVELOPMENT FOR LABORATORY EXPERIMENTS

Two types of gages are being developed for use in our static borehole inclusion experiments. The first type is a miniature stress gage designed to minimize the inclusion effect on stress measurement in small-scale laboratory experiments. The gage is much smaller than the smallest practical flatpack stress gage. It also has a strong potential for measuring stress in dynamic laboratory experiments. The second type of gage is a small inductive or capacitive sensor to measure the separation and relative slip at an interface, such as the interface formed by borehole fill and the surrounding medium. This gage has the potential to be modified for dynamic measurements.



(a) Section A-A



(b) Vertical Cross Section

JA-5877-25

Figure 35. Inclusion apparatus.

### Miniature Stress Gage

The sensing element of the stress gage is a 0.3-mil-thick, 1/4-inch by 1/4-inch grid of ytterbium bonded to a 2-mil-thick layer of Kapton. The leads are 1-mil-thick strips of copper also bonded to the Kapton. These elements were specially prepared for us by Dynasen.\* The resistance is about 50 ohms. The element is located at the midplane of a thin disk of fluid or fluid-like material. The disk is thin enough to be sensitive only to the stress perpendicular to the disk face. Currently, the overall dimensions of the disk are 1 inch for the diameter and 1/10 inch for the thickness, but these can be reduced once a satisfactory design has been achieved. The fluid pressure is approximately equal to the stress to be measured, and the change in resistance of the ytterbium sensor determines the fluid pressure. For our ytterbium, the hydrostatic calibration was 6%/kbar for the resistance change.

Two kinds of stress gages have been tested, the main difference between the designs being the fluid. In one design, we used glycerol enclosed by urethane sheets, whereas in the other we used the fluid-like material, GE silicone (RTV). Results and observations from the testing to date of these two gages are summarized as follows:

- Under hydrostatic pressure the gages in water follow the hydrostatic calibration curve for the ytterbium element.
- The RTV gage measured the axial stress well in alluvium subjected to static uniaxial strain loading, unlike the glycerol gage.
- Both types of gages measured stress changes satisfactorily above 1500 psi (10.33 MPa) in 2C4 grout subjected to static uniaxial stress loading. Below 1000 psi (6.89 MPa), both types of gage provided measurements that were unacceptably low.
- The RTV gage is much simpler to manufacture and is adaptable for installation in geologic specimens.

---

\*Dynasen, Inc., 20 Dean Arnold Place, Goleta, California 93017.

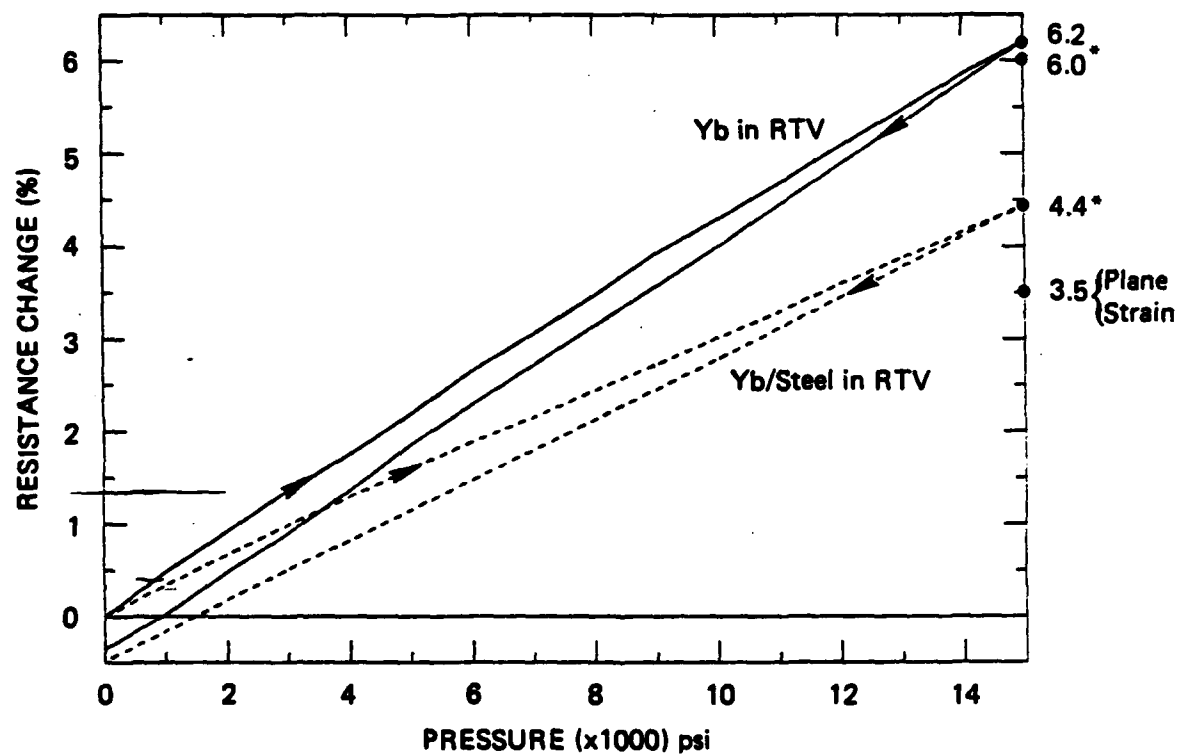
In conclusion, the RTV version of the stress gage was better than the glycerol version in performance, ease of fabrication, and adaptability to geologic materials. The unsolved problem that remains is the measurement of stress below about 1500 psi. It is desirable to have this capability so that the gages can be incorporated in the static plane-strain borehole experiment. If this problem is not solved within a reasonable time, we will measure strain only using miniature rod gages\* embedded and anchored in the 2C4 grout.

Because the RTV version of the stress gage showed more promise than the glycerol version, we continued development work only on the RTV version to address two problems. The first problem occurred when the sand or grout loading caused distortion of the inclusion that involved stretching of the midplane. Although the RTV has a low shear modulus, we found that the combination of high pressure and distortion caused stretching of the ytterbium grid by shear traction. The induced tension dominated the resistance change (a decrease). To suppress this induced tension, we bonded the Kapton tape under the ytterbium grid to a thin steel plate. The resulting gage response was a correct measurement of stress change, except again for an insensitivity at low stresses ( $< 1000$  psi).

The second problem is the applicability of the piezoresistive constants that have been determined for ytterbium foil, to ytterbium that has been vapor deposited, as is the case with our grids. We solved this problem by hydrostatically loading two RTV gages to 1 kbar. In one gage, the ytterbium grid was free and in the other the ytterbium grid was bonded to a thin steel plate. The resistance change was calculated using the piezoresistive coefficients for ytterbium foil and the results were compared with the experimental values. The extent of the agreement is shown in Figure 36, the calculated values of the linear pressure-

---

\*Manufactured by Ailtech, 19535 East Walnut Drive, City of Industry, CA 91748.



JA-5877-41

\* Calculated using Piezo. Coeffts.  $\pi_{11}$ ,  $\pi_{12}$

Figure 36. Loading and unloading of piezoresistive ytterbium under various conditions.

resistance change curves being 6.0%/kbar and 4.7%/kbar for the free and bonded grids. We conclude that the piezoresistive coefficients are applicable to our grids in the pressure range of our investigation ( $< 1$  kbar). We have yet to resolve the observation that the loading and unloading lines in Figure 36 are not the same.

#### Interface Gage

Interface gages are based on the principle that inductive loops or capacitive plates located on either side of an interface will change their mutual inductance,  $M$ , or capacitance,  $C$ , when the interface experiences separation or relative slip. These gages form part of a tank circuit that oscillates at a design frequency. When  $M$  or  $C$  changes, the natural frequency changes. Design calculations indicate that the mutual inductance gage is more sensitive than the capacitance gage because compact ferritic cores with many turns of wire are available to produce high mutual inductances. The resulting gage is about  $1/4$  inch in diameter and  $1/8$  inch thick. The high inductance allows us to use standard electronic equipment and frequencies below 1 MHz.

#### 6.4 LONG-DURATION PLANE WAVE EXPERIMENT

One objective of the dynamic experimental program is to perform well-controlled uniaxial strain impact experiments on matrix materials containing embedded flatpack gages with piezoresistant foil sensors. The results of these experiments are intended to be compared to those from analogous gas gun experiments performed by Gupta, in which the matrix contained bare piezoresistant foils without the surrounding gage package.

The SRI 4-inch gas gun would be a convenient loader for these experiments, if the valid one-dimensional test time (before the arrival of edge effects) is great enough for a scaled down flatpack gage package to come to mechanical equilibrium with the flow in the surrounding matrix material. For a PMMA matrix material, the one-dimensional test time in the 4-inch gas gun is estimated to be about 8-9  $\mu$ s over the

central inch of the target at the stresses of interest. Therefore, we performed a series of calculations with the SRI PUFF one-dimensional finite difference code to determine the response time of thin gage packages to uniaxial strain shock compressions and release.

For these one-dimensional calculations, the gage package is modeled simply as two steel layers surrounding a PMMA layer (at the center of which would be the piezoresistant foil). The package is embedded in a PMMA matrix, and the matrix is impacted by a PMMA flier. The problem is run for 8  $\mu$ s, the estimated maximum valid one-dimensional test time in the 4-inch gas gun. We performed the following series of calculations.

First, we performed thick (1-inch) flier calculations to determine the response to compression only (no rarefaction from the free surface of the impactor for at least 8  $\mu$ s) for two gage package thicknesses. The equilibration time at the center of the package to the compression was determined and the appropriate flier thickness was calculated. We then performed thin flier calculations to determine the response time of these gage packages to step compression and release. We considered three flier velocities, 0.56, 1.0, and 1.56 km/s (the latter being the maximum velocity achievable in this gun), corresponding to PMMA stresses of about 1, 2, and about 3.7 GPa.

We verified that the computational results were not zone size limited by halving the zone size in one calculation. We established baseline computational rise times and numerical oscillation characteristics for use in interpreting the gage package calculations by performing calculations with the same zoning but with all components (target, gage package, and impactor) PMMA.

We computationally examined two gage package thicknesses. In the thicker package, each steel layer was 0.02 inch thick and the PMMA was 0.10 inch thick. In the thinner package, each of these dimensions was halved. Although even thinner packages could conceivably be fabricated, the steel layers would be foils no longer having the characteristics of the full-scale components and the results would not be relevant to real gage packages.



The calculations led to two primary conclusions. First, only the compressional response, not the following release, could be examined on the 4-inch gas gun. Because the unloading response is equally important, the limited duration of planar flow in the 4-inch gas gun is a severe restriction. Second, even in compression, only the thinner package reaches mechanical equilibrium rapidly enough to be tested in the 4-inch gun.

These conclusions pertain only to equilibration in the wave propagation direction (one-dimensional equilibration). The actual package would have to equilibrate in the transverse directions as well. Although the equilibration times for these processes are longer, the magnitude of the nonequilibrium effects are smaller.

Suitable stress pulses for measuring both loading and unloading response in realistic embedded gage packages can be generated by an explosive launcher device that propels flyer plates much larger in diameter and thickness than those used with gas guns. The design of such a launcher is presented below. It produces plane wave pulse durations long enough for an examination of the loading, peak stress, and unloading responses of stress gage packages.

The design presented is specific. Variations to extend the stress or duration range are summarized immediately following the design.

#### Flyer Plate/Target Characteristics

We choose the plastic PMMA as the flyer plate material because it is light and the properties are known. We choose the rock simulant 2C4 for the target material because the stress gage package can be cast in place and again the properties are known. For planar impact at a velocity small compared with shock velocities, the stress induced in the target is approximately

$$\sigma = \frac{\rho_1 c_1 \rho_2 c_2}{\rho_1 c_1 + \rho_2 c_2} v \quad (21)$$

where

$\rho_1$  = flyer plate density

$c_1$  = flyer plate shock velocity

$\rho_2$  = target density

$c_2$  = target shock velocity

$V$  = impact velocity

$\sigma$  = stress in target.

For a flyer plate of PMMA and a target of 2C4, we have

$$\rho_1 = 1.18 \text{ g/cm}^3 \quad c_1 = 3.5 \text{ mm}/\mu\text{s} \quad \rho_2 = 2.15 \text{ g/cm}^3 \quad c_2 = 3.3 \text{ mm}/\mu\text{s}$$

and when  $V = 100 \text{ m/s}$ , the stress in the target is

$$\sigma = 2.6 \text{ kbar.} \quad (22)$$

The particle velocity in the 2C4 is

$$v = \frac{\rho_1 c_1}{\rho_1 c_1 + \rho_2 c_2} V = 0.37V = 37 \text{ m/s.} \quad (23)$$

For a flyer plate of PMMA, the stress pulse duration,  $T$ , is twice the transit time through the thickness,  $h_1$ ; that is,  $T = 2h_1/c_1$ . If  $h_1 = 4 \text{ in. (10.16 cm)}$ ,

$$T = 58 \mu\text{s.} \quad (24)$$

The minimum diameters of flyer plate and target are determined by the duration of the stress pulse. To allow examination of the stress gage package response to known unloading, rarefaction waves from the edge of the flyer and target plates must not reach the gage before the pulse ends. If the gage is located on the common axis of the plates near the impact surface and if the velocity of the rarefaction wave is approximated by the shock velocity, the minimum diameter is  $D = 2 \max(c_1, c_2) \cdot T$ . For a 4-inch-thick PMMA flyer plate striking a 2C4

AD-A159 458

INCLUSION EFFECTS ON STRESS GAGE MEASUREMENTS IN ROCK  
AND SOIL(U) SRI INTERNATIONAL MENLO PARK CA  
A L FLORENCE ET AL. 01 MAY 84 DNR-TR-84-210

2/2

UNCLASSIFIED

DNR001-83-C-0279

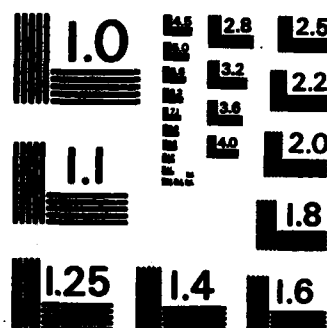
F/G 8/7

NL

END

FILMED

DTIC



MICROCOPY RESOLUTION TEST CHART  
NATIONAL BUREAU OF STANDARDS-1963-A

target, we have  $\max(c_1, c_2) = c_1 = 3.5 \text{ mm}/\mu\text{s}$  and  $T = 58 \mu\text{s}$ , so  $\min D = 16 \text{ in. (40.6 cm)}$ .

In our design we choose  $D = 21 \text{ inches}$  to ensure that the arrival time of the edge rarefaction (i.e.,  $76 \mu\text{s}$ ) is well past the pulse unloading time.

The minimum thickness of the 2C4 is similarly chosen to allow an adequate unloading. With 5 inches of 2C4 behind the gage package, the rarefaction from the near face of the target will arrive at  $77 \mu\text{s}$ .

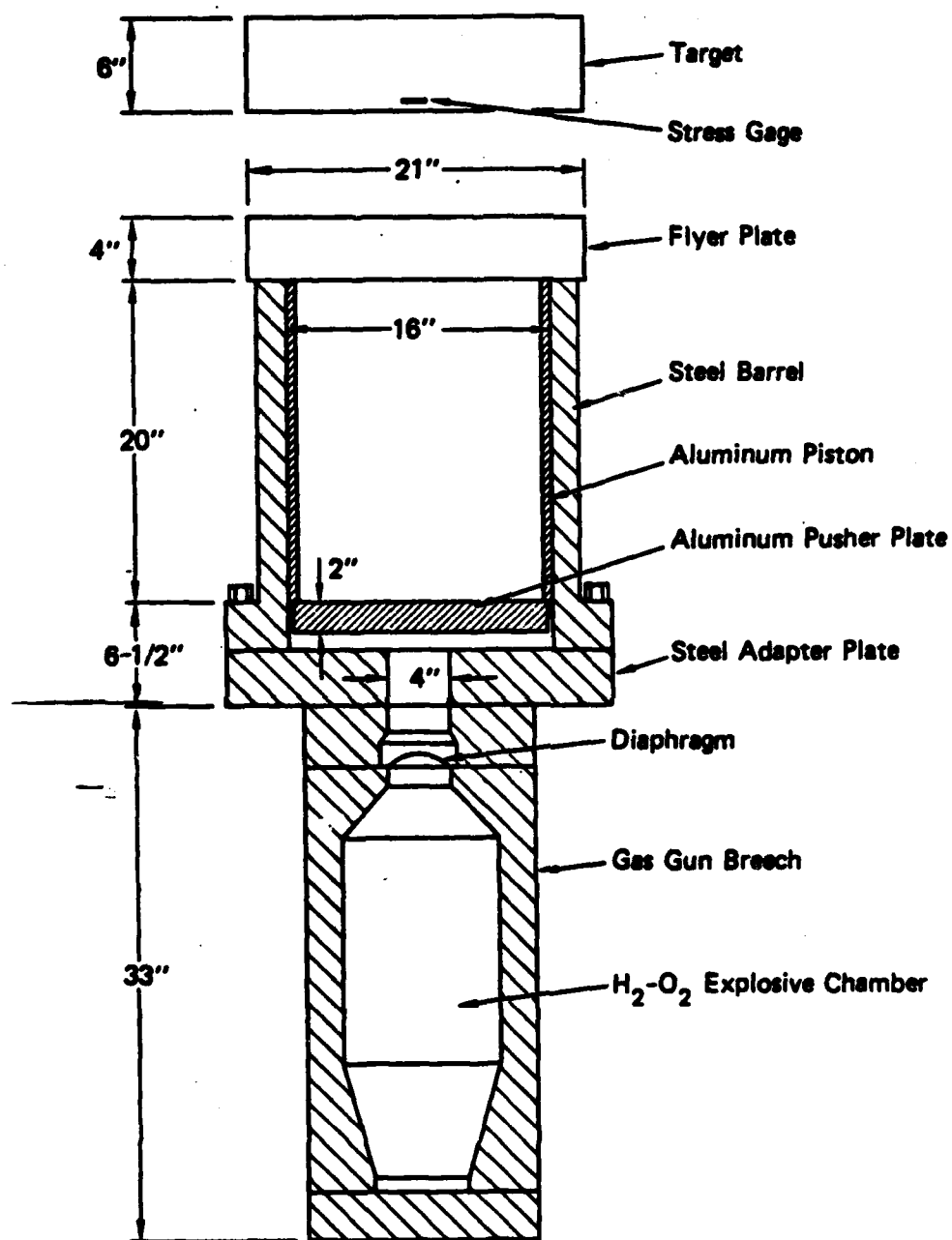
### Launcher Dynamics

Figure 37 shows schematically the launcher, flyer plate, and target. A steel pressure vessel is filled with a stoichiometric mixture of hydrogen and oxygen at some specified pressure, and the mixture is held by a diaphragm. Detonation of this gaseous mixture increases the pressure, which causes the diaphragm to rupture, and the expanding steam drives a piston with an attached flyer plate along a short tube toward a target.

The pressure vessel with its diaphragm arrangement is the vessel used to launch turbine missiles at reinforced concrete barriers in our past industrial safety experiments.<sup>10</sup> We found this energy source to be reliable, reproducible, versatile, and economical.

Our design is based on launching a 16-inch-diameter piston capable of carrying a 21-inch-diameter flyer plate of 4-inch-thick PMMA. The flyer plate may be thicker and larger in diameter if longer pulses are required.

Let the piston assembly consist of three main parts: a 16-inch-diameter, 2-inch-thick aluminum pusher plate; a 16-inch-diameter, 1/2-inch-thick, 20-inch-long aluminum tube; and the 21-inch-diameter, 4-inch-thick PMMA flyer plate. The masses of these parts are approximately 17.8, 22.2, and 26.8 kg, respectively, giving a total piston mass of 66.8 kg. We use a mass of  $M = 70 \text{ kg}$  in our design calculations to take into account any additional mass from attachments, oversizing, and the like.



JA-6677-37

Figure 37. Large flyer plate experiment.

If we design for an impact velocity of  $V = 100$  m/s, the piston kinetic energy to be supplied by gas work is

$$K = \frac{1}{2} MV^2 = 3.5 \times 10^5 \text{ Nm} \quad (25)$$

for  $M = 70$  kg. An equation of state appropriate for steam at the pressures in our launcher ( $< 300$  bar) is the perfect gas law  $pv^\gamma = \text{constant}$ , with  $\gamma = 1.14$ . The maximum gas work available when the initial pressure and volume are  $p_0$  and  $v_0$  is

$$W_{\infty}^{(0)} = \frac{p_0 v_0}{\gamma - 1} \quad (26)$$

Our pressure vessel has a volume of  $v_0 = 0.0287 \text{ m}^3$ , which, with a constant volume pressure following detonation of  $p_0 = 3250$  psi (224 bars), gives the gas work as

$$W_{\infty}^{(0)} = 45.9 \times 10^5 \text{ Nm} \quad (27)$$

This work is more than 13 times the kinetic energy required. The pressure of the hydrogen/oxygen mixture before detonation that is required to produce a constant volume pressure of 224 bars is 21 bars (300 psi, ratio of 10.8). After the diaphragm splits, the gas expands to a volume of  $v_1 = 0.0332 \text{ m}^3$  before it starts to move the piston. The expansion comprises the orifice volume (4 inches in diameter, 6 inches long) and a 1-inch space behind the piston for a smoother launch. When  $v = v_1$ , the pressure is  $p_1 = 2810$  psi (194 bars), and the work done on the piston when the steam has increased in volume from  $v_1$  to  $v_2$  is

$$W = W_{\infty}^{(1)} \left[ 1 - \left( \frac{v_1}{v_2} \right)^{\gamma-1} \right] \quad (28)$$

where

$$W_{\infty}^{(1)} = \frac{p_1 v_1}{\gamma - 1} = 45.9 \times 10^5 \text{ Nm}$$

The value of  $v_2$  when the gas work,  $W$ , equals the required kinetic energy of  $K = 3.5 \times 10^5 \text{ Nm}$  is therefore

$$v_2 = v_1 \left[ 1 - \frac{K}{W_{\infty}} \right]^{-\frac{1}{\gamma-1}} = 1.76 v_1 \quad (29)$$

Because  $v_1 = 0.0332 \text{ m}^3$ , we have  $v_2 = 0.0584 \text{ m}^3$ ; hence the increase in volume caused by piston motion is  $v_2 - v_1 = 0.0252 \text{ m}^3$ . The 16-inch-diameter piston cross-sectional area is  $A = 0.13 \text{ m}^2$ ; thus the piston travel before it attains a velocity of 100 m/s is  $L = 0.19 \text{ m}$  (7.5 inches). When the steam has expanded to the volume  $v_2$ , the pressure has decreased from  $p_1 = 194 \text{ bars}$  to  $p_2 = 102 \text{ bars}$ .

An upper bound estimate for the duration of piston travel is obtainable by approximating the pressure in the equation of motion

$$M\ddot{x} = pA \quad (30)$$

by

$$p = p_1 - (p_1 - p_2) \frac{x}{L}$$

Integration then leads to the expression for the duration of piston motion

$$t = \left[ \frac{ML}{(p_1 - p_2)A} \right]^{1/2} \cos^{-1} \frac{p_2}{p_1} \quad (31)$$

For  $M = 70 \text{ kg}$ ,  $L = 0.19 \text{ m}$ ,  $A = 0.13 \text{ m}^2$ ,  $p_1 = 194 \text{ bars}$ , and  $p_2 = 102 \text{ bars}$ , we obtain  $t = 3.4 \text{ ms}$ .

### Structural Design

In calculating the mass of the piston, we assumed that a 2-inch-thick, 16-inch-diameter piston pusher plate of aluminum alloy would be strong enough to withstand the gas pressure. When the pusher plate is considered as an elastic, simply supported circular plate under a static



uniform pressure  $p_1$ , the maximum stress at the center is

$$\sigma = \frac{3(3 + \nu)a^2 p_1}{8h^2} \quad (32)$$

where  $a$  is the radius,  $h$  the thickness, and  $\nu$  is Poisson's ratio. For  $a = 8$  inches,  $h = 2$  inches, and  $\nu = 0.34$ , we have  $\sigma = 20 p$ . If  $p_1 = 194$  bars (2810 psi), we have  $\sigma = 56,370$  psi, which implies yielding for most aluminum alloys, especially since the load is applied suddenly. Because the piston is not reusable, some yielding is acceptable. The static plastic collapse pressure of the plate is

$$p = \frac{3h^2}{2a^2} \sigma_y = \frac{3}{32} \sigma_y \quad (33)$$

where  $\sigma_y$  is the yield stress. If  $\sigma_y = 66,000$  psi (7075-T6 alloy), the static collapse pressure is 6,188 psi (427 bars), which is well above  $p_1$ . Thus, without further analysis we may say that a 2-inch-thick plate will probably be adequate. A 3-inch-thick plate will certainly be adequate, but it increases the piston mass and is more expensive.

The 20-inch-long tubular portion of the piston (Figure 37) is designed to be longer than the diameter for smooth travel along the steel launcher tube. The maximum thrust on the piston, which occurs at the start of motion, is  $25.2 \times 10^5$  N. If the wall thickness is 1/2 inch, the maximum "static" axial stress is 23,200 psi (1,600 bars), which is well below the yield stress for most aluminum alloys, and the radius-to-thickness ratio of 16 is small enough to preclude buckling under these loading conditions.

The flyer plate is stressed by inertial forces, which are greatest at the start of motion when the thrust on the piston is  $F = 25.2 \times 10^5$  N. For a piston mass of  $M = 70$  kg, the initial acceleration is  $\alpha = F/M = 36,000$  m/s<sup>2</sup>. A 4-inch-thick PMMA flyer plate has an areal density of  $m = 12$  g/cm<sup>2</sup>; hence, the uniformly distributed inertial pressure is  $m\alpha = 43.2$  bars (626 psi).

An elastic circular plate of radius  $r_1$  on a circular support ring of radius  $r_0$  subjected to a uniform pressure  $p_\alpha$  has its extremum bending moments at the center  $r = 0$  and over the support ring  $r = r_0$ . These are

$$m_r(0) = \frac{p_\alpha r_0^2}{16} \kappa_1 \quad m_r(r_0) = \frac{p_\alpha r_0^2}{16} [\kappa_1 - (3 + \nu)] \quad (34)$$

where

$$\kappa_1 = 2(1 - \nu) + (1 + 3\nu)\beta^2 - 2(1 + \nu)\beta^2 \ln \beta^2, \quad \beta = r_1/r_0$$

For our flyer plate we have  $r_1 = 10.5$  inches and  $r_0 = 7.75$  inches, so  $\beta = 1.35$ . For PMMA, Poisson's ratio  $\nu = 0.35$ ; thus  $\kappa_1 = 2.083$  and  $\kappa_1 - (3 + \nu) = -1.267$ , giving  $m_r(0) = 7.82 p_\alpha$  and  $m_r(r_0) = -4.76 p_\alpha$ . The fiber stress  $\sigma_b$  is related to the bending moment by  $\sigma_b = 6 m_r/h^2$ , where  $h$  is the plate thickness (4 inches). Hence,  $\sigma_b(0) = 2.93 p_\alpha$  and  $\sigma_b(r_0) = -1.79 p_\alpha$ . For an inertial pressure of  $p_\alpha = 626$  psi,

$$\sigma_b(0) = 1,834 \text{ psi} \quad \sigma_b(r_0) = 1,121 \text{ psi} \quad (35)$$

which are well below the PMMA tensile strength of 8,000 psi. Thus, the PMMA flyer plate will not fracture during launching because of its overall structural response.

The steel tube for guiding the piston and containing the steam is designed to withstand an internal pressure of  $p_1 = 2,810$  psi. The hoop stress is  $\sigma_\theta = a/h p_1$ . If the tube thickness is chosen to be  $h = 2$  inches giving  $a = 9$  inches we have a safe working stress of  $\sigma_\theta = 12,645$  psi.

#### Overall Piston-Target Impact

Assuming the impact of the piston on the target to be plastic so that they both move together as a single mass allows us to estimate the combined velocity after impact. For a 6-inch-thick 2C4 target, 21 inches in diameter, the mass is  $M_T = 74$  kg. Our piston has a total mass of  $M_p = 70$  kg; thus the combined velocity after impact is

$$V_{PT} = \frac{M_P}{M_P + M_T} V_P = 0.486 V_P$$

When the piston strikes the target at  $V_P = 100$  m/s, we get  $V_{PT} = 49$  m/s.

#### Characteristics of Various Flyer Plate Materials

In the preceding discussion, flyer plate/target characteristics were presented for the specific case of a plastic PMMA flyer impacting a grout target. The plastic PMMA flyer induced a stress of  $\sigma = 2.6$  kbar in the grout target. The stress induced in the target may be extended by appropriate choice of flyer plate materials. Table 2 compares the flyer plate/target characteristics of 4-inch-thick aluminum, grout, and plastic PMMA flyers impacting a grout target. For an impact velocity of  $V = 100$  m/s, the stress induced in the target increases to 5 kbar for an aluminum flyer plate and 3.6 kbar for a grout flyer plate. Note, however, that the aluminum flyer plate produces a pulse duration that is just over half of the pulse duration produced by the plastic PMMA flyer. A thicker aluminum plate could be used to increase the pulse duration. Also tabulated are the launch length until impact,  $L$ , and the launch time until impact,  $T$ .

Table 2. Flyer Plate/Target Characteristics

<u>4-Inch Flyer</u>	<u>(kbar)</u>	<u>V (m/s)</u>	<u>Pulse T ( s )</u>	<u>Launch L<sup>a</sup> (m)</u>	<u>Launch T (ms)</u>
PMMA	2.6	100	58	0.19	3.4
Aluminum	5.0	100	32	0.35	5.7
Grout <sup>b</sup>	3.6	100	62	0.29	4.8

---

<sup>a</sup>The launch distances for aluminum and grout flyer plates can be reduced by increasing the initial hydrogen/oxygen pressures.

<sup>b</sup>The grout flyer must be reinforced because of its low tensile strength (500 psi).

## REFERENCES

1. J. Thomas Rosenberg, "Dynamic In Situ Free-Field Stress Measurement Program," Appendix to Final Report, DNA Contract DNA002-82-C-0248, SRI International, Menlo Park, California (in progress).
2. J. O. Hallquist, "NIKE2D: An Implicit, Finite Deformation, Finite-Element Code for Analyzing the Static and Dynamic Response of Two Dimensional Solids," University of California, Lawrence Livermore National Laboratory, Report UCRL-52678 (1979).
3. J. Byerlee, "Friction of Rocks," Proceedings of Conference II - Experimental Studies of Rock Friction with Application to Earthquake Prediction, USGS (1977).
4. M. Stippes, H. B. Wilson, Jr., and F. N. Krull, "A Contact Stress Problem for a Smooth Disk in an Infinite Plate," Proceedings of the Fourth U.S. National Congress of Applied Mechanics, Vol. 2, pp. 799-806 (1962).
5. J. C. Cizek and A. L. Florence, "Laboratory Investigation of Containment of Underground Explosions," Proceedings of the Monterey Containment Symposium, LA-92LL-C, Vol. 1 (August 1981), pp. 7-29.
6. N. I. Muskhelishvili, Some Basic Problems of the Mathematical Theory of Elasticity (P. Noordhoff Ltd., Groningen-Holland, 1953).
7. Y. M. Gupta, Washington State University, private communication (1983).
8. Y. M. Gupta, "Determination of the Impact Response of PMMA Using Combined Compression and Shear Loading," J. Appl. Phys., 51(10), 1980, pp. 5352-5361.
9. Y. M. Gupta, "Analysis and Modeling of Piezoresistance Response," Final Report, DNA 5451F, SRI International, Menlo Park, California (1980).
10. C. M. Romander and A. L. Florence, "Scale Model Tests of Turbine Missile Containment by Reinforced Concrete," SRI Final Report to EPRI, No. NP-2747 (March 1983).

## Appendix

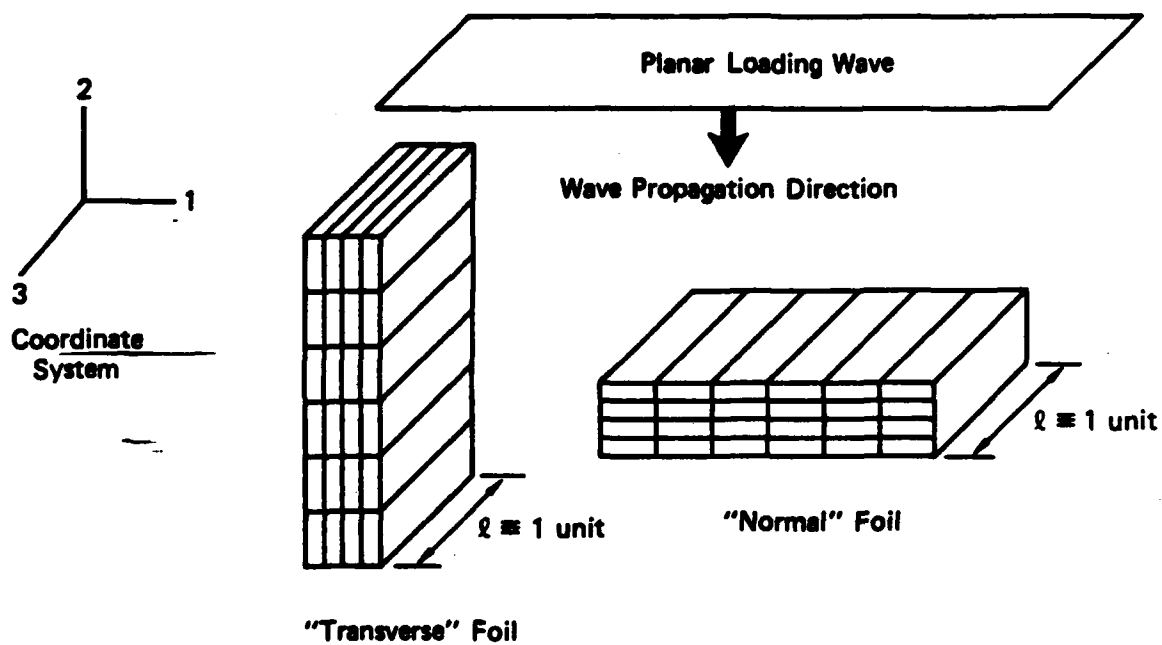
### COMPARISON OF RESISTANCE AVERAGING WITH MECHANICAL AVERAGING FOR CALCULATING THE RESISTANCE CHANGE OF A PIEZORESISTANCE FOIL IN PLANE STRAIN

In this appendix, we examine the equivalence of calculating the stress-induced change in total resistance of a piezoresistant foil in plane strain deformation by two methods: resistance and mechanical averaging. In resistance averaging, we convert the stresses and strains induced in the foil by a stress wave to cell quantities, determine the resistance of each cell, and then calculate the total resistance change from a network circuit analysis. In mechanical averaging, we calculate an average value over the foil for each component of stress and strain and use these to calculate the total resistance change of the foil. Both methods use the piezoresistance formulation of Y. Gupta expressing the vector resistance in terms of the mechanical state variables at a point:

$$\frac{R_i}{R_0} = [1 + \alpha (\sigma_1 + \sigma_2 + \sigma_3) + 2 \beta \sigma_i + \eta W_p] \frac{1 + \epsilon_i}{(1 + \epsilon_j)(1 + \epsilon_k)} \quad (A.1)$$

where  $R_i$  is the resistance to current flowing in the  $i$  direction,  $R_0$  is the initial value of this (and the other) resistance components,  $\sigma$  is stress,  $\epsilon$  is strain,  $W_p$  is a plastic work function, and  $\alpha$ ,  $\beta$  and  $\eta$  are piezoresistance coefficients.

The basic problem we wish to calculate, the resistance change to constant current flow in the length direction of a foil as it is loaded by a normally incident planar wave, is shown schematically in Figure A.1, along with the foil configurations. The length direction of the foil has been arbitrarily chosen along the 3-axis and the incident plane wave is propagating in the 2-direction. The figure shows the two foil orientations, normal and transverse, of practical interest and includes the type of zoning appropriate for plane strain calculations. (For



JA-5877-42

Figure A1. Piezoresistant foil configurations.

notational convenience, throughout this Appendix we have set the length equal to one unit as indicated in the figure.)

By modeling the internal deformation of the foil as two-dimensional plane strain (a good approximation, usually, since real foils are normally much longer than they are wide or thick), we have imposed the implicit constraint that the foil "faces" (cross sections perpendicular to the indicated length dimension) remain parallel to the 1-2 plane. This constraint is important for the resistance averaging calculations. Below we describe the specific resistance and mechanical averaging approaches used for the special cases considered in this appendix, formulate a particularly simple test problem, and apply resistance averaging and mechanical averaging to the test problem to demonstrate and compare the two methods.

#### Resistance Averaging

We assume that (1) steady state conditions exist for the current distributions and potential distributions, (2) resistance is the only source of potential differences, and (3) fringing can be neglected. With these assumptions and a plane strain representation, the "faces" of the foils are equipotential surfaces. Therefore, the electrical field  $\vec{E}$  and current density  $\vec{j}$  vectors are in the 3-direction at the foil faces. Since each "face" is an equipotential surface, since mechanical variations are not permitted in the 3-direction, and since the separation of the faces is arbitrary, then the potential vectors within each cell are also in the 3-direction only and the cells behave as independent resistors in parallel.

Thus, in resistance averaging the total resistance in the 3-direction,  $R_{TOT,3}$ , of the conductor is obtained by first calculating  $R_j^j/R_0$  for each cell,  $j$ , from equation (A.1) using the calculated stresses and strains in the cell and the initial resistance, and then summing these resistances in parallel according to

$$R_{TOT,3} = \left[ \sum_j \frac{1}{R_j^j} \right]^{-1} \quad (A.2)$$



### Mechanical Averaging

In this approach, we determine a single average value for each stress and strain component within the foil, as well as for the plastic work. We then use these in equation (A.1) to find the total resistance change.

Principal engineering strains are adequate for our purposes. We obtain average values by summing over external boundaries of exterior cells,  $k$ , as indicated below:

$$\bar{\epsilon}_i = \frac{\sum_k X_i^k - X_i^0}{X_i^0} \quad (\text{A.3})$$

where  $X_i^k$  is the length of the external boundary of cell  $k$  in the  $i$  direction and  $X_i^0$  is the total length of the undeformed foil in the  $i$  direction.

To obtain average stresses, we sum external forces and divide by the area of external faces:

$$\bar{\sigma}_i = \frac{\sum_k \sigma_i^k A_i^k}{\sum_k A_i^k} \quad (\text{A.4})$$

To obtain the average plastic work, we average over the mass or volume of all the cells,  $j$ :

$$\bar{W}_p = \frac{\sum_j W_p^j R_j}{\sum_j R_j} \quad (\text{A.5})$$

where  $R_j$  is the mass or volume of cell  $j$ .

### Test Problem

Consider the uniaxial strain dynamic deformation induced by a constant amplitude planar shock in a foil composed of just two cells, as

shown in Figure A.2. Since cross-sectional dimensions are arbitrary, this can be either a transverse or normal foil; a transverse foil is shown. We wish to calculate the resistance by the two methods when the deformational wave has reached the boundary between cells.

Without loss of generality, we set all initial linear cell dimensions and all initial cell resistances to unity. Furthermore, we postulate that the foil material is hydrodynamic so that within a cell,  $\sigma_1 = \sigma_2 = \sigma_3$ . We also select it to have hydrostatic piezoresistive response,  $\beta = \eta = 0$ , so that equation (A.1) becomes

$$\frac{R_3}{R_0} = [1 + \alpha (\sigma_1 + \sigma_2 + \sigma_3)] \frac{1 + \epsilon_3}{(1 + \epsilon_1)(1 + \epsilon_2)} \quad (\text{A.6})$$

#### Resistance Averaging Applied to Test Problem

Consider cell 1. The stresses and strains are

$$\epsilon_1 = \epsilon_3 = 0, \quad \epsilon_2 \equiv \epsilon$$

$$\sigma_1 = \sigma_3 = \sigma_2 \equiv \sigma$$

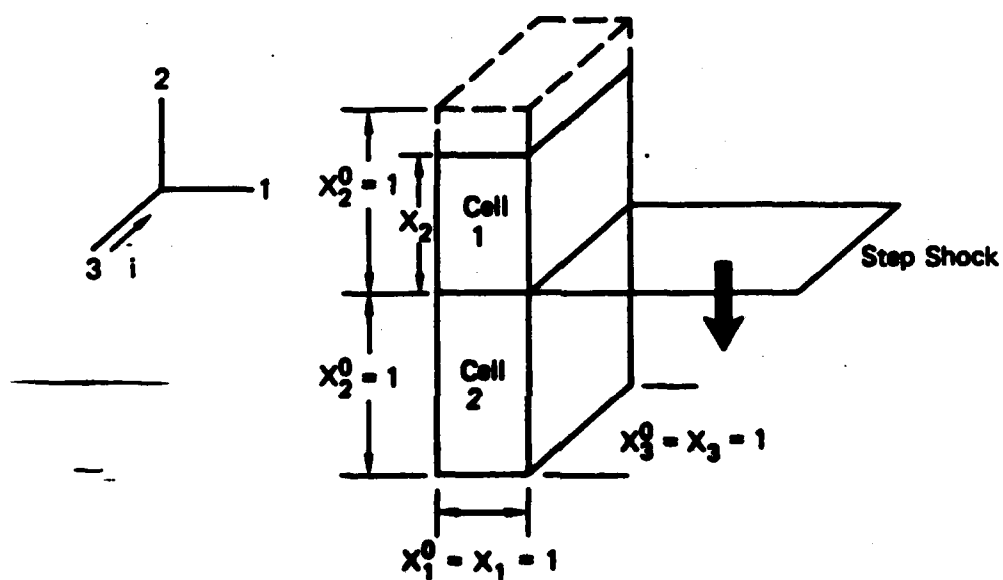
Therefore, by equation (A.6), the relative resistance in this cell is

$$\frac{R_3^1}{R_0} = \frac{R_3^1}{R_3^1} = (1 + 3 \alpha \sigma) \frac{1}{1 + \epsilon}$$

For cell 2;

$$\frac{R_3^2}{R_0} = 1$$

Therefore, by equation (A.2), resistance averaging gives the total foil resistance in the 3-direction as



JA-6877-43

Figure A2. Uniaxial strain two-cell test problem. Front of step shock is at boundary between cells 1 and 2. Current flow is in the 3 direction.

$$\begin{aligned}
R_{TOT,3} &= \frac{R_3^{(1)} R_3^{(2)}}{R_3^{(1)} + R_3^{(2)}} \\
&= \frac{(1 + 3 \alpha \sigma)/(1 + \epsilon)}{[(1 + 3 \alpha \sigma)/(1 + \epsilon)] + 1} \\
&= \frac{1 + 3 \alpha \sigma}{2 + 3 \alpha \sigma + \epsilon}
\end{aligned}$$

and the relative resistance as

$$\frac{R_{TOT,3}}{R_0} = \frac{R_{TOT,3}}{2} = \frac{1}{2} \left( \frac{1 + 3 \alpha \sigma}{2 + 3 \alpha \sigma + \epsilon} \right) \quad (A.7)$$

#### Mechanical Averaging Applied to Test Problem

First, consider the strains. Within each cell the transverse strains are zero, so

$$\bar{\epsilon}_1 = \bar{\epsilon}_3 = 0$$

The average axial strain from equation (A.3) is

$$\begin{aligned}
\bar{\epsilon}_2 &= \frac{[x_2^1 + x_2^2] - [(x_2^1)^0 + (x_2^2)^0]}{[(x_2^1)^0 + (x_2^2)^1]} \\
&= \frac{[(1 + \epsilon) + 1] - [1 + 1]}{[1 + 1]} \\
&= \frac{\epsilon}{2}
\end{aligned}$$

Now consider the stresses. Since the foil material is hydrostatic, the three principal stresses within either cell are equal. However, the average stresses over the whole foil may not be equal and are therefore treated separately. Consider first the average transverse stresses,  $\bar{\sigma}_1$  and  $\bar{\sigma}_3$ . By symmetry  $\bar{\sigma}_1 = \bar{\sigma}_3$ . Now evaluate  $\bar{\sigma}_1$  from equation (A.4).

$$\bar{\sigma}_1 = \frac{\sigma_1^1 A_1^1 + \sigma_1^2 A_1^2}{A_1^1 + A_1^2} \quad (\text{A.8})$$

where, as usual, the subscript denotes the coordinate axis and the superscript denotes the cell. Remember that  $\sigma_1^1 = \sigma$ ,  $\sigma_1^2 = 0$ ,  $A_1^1 = (1 + \epsilon)$  and  $A_1^2 = 1$ . Therefore,

$$\bar{\sigma}_1 = \sigma \frac{1 + \epsilon}{2 + \epsilon} = \bar{\sigma}_3 \quad (\text{A.9})$$

Now consider the average axial stress,  $\bar{\sigma}_2$ . Although the cells are not in mechanical equilibrium in this direction, we obtain, by formally applying equation (A.4),

$$\begin{aligned} \bar{\sigma}_2 &= \frac{\sigma_2^1 A_2^1 + \sigma_2^2 A_2^2}{A_2^1 + A_2^2} \\ &= \frac{\sigma}{2} \end{aligned}$$

Thus the average stresses in the foil do not satisfy the hydrodynamic postulate with this averaging method except in the limit as  $\epsilon \rightarrow 0$ .

Substituting these average stresses and strains into equation (A.6), we find that the total relative resistance change in the 3-direction, by mechanical averaging, is

$$\begin{aligned} \frac{R_{\text{TOT},3}}{R_0} &= [1 + \alpha (\bar{\sigma}_1 + \bar{\sigma}_2 + \bar{\sigma}_3)] \frac{1 + \bar{\epsilon}_3}{(1 + \bar{\epsilon}_1)(1 + \bar{\epsilon}_2)} \\ &= [1 + \alpha \{2\sigma \left(\frac{1 + \epsilon}{2 + \epsilon}\right) + \frac{\sigma}{2}\}] \frac{1}{1 + \epsilon/2} \\ &= \frac{2 + \alpha [2\sigma \frac{2(1 + \epsilon)}{2 + \epsilon} + \sigma]}{(2 + \epsilon)} \quad (\text{A.8}) \end{aligned}$$

## Conclusions

The simple two-cell transient response calculations considered above show that resistance and mechanical averaging are not equivalent, in general, since equations (A.7) and (A.8) are unequal. Resistance averaging was derived from basic principles, whereas mechanical averaging was simply postulated and is not considered to be physically realistic. Therefore, in plane strain calculations of the type considered here, we conclude that piezoresistance effects should be calculated by resistance averaging, treating the current carrying cells in the length direction of the foil as independent parallel variable resistors.

## DISTRIBUTION LIST

### DEPARTMENT OF DEFENSE

Assistant to the Secretary of Defense  
Atomic Energy  
ATTN: Executive Assistant

Defense Intelligence Agency  
ATTN: DB-4C2, C. Miehle  
ATTN: RTS-2B

Defense Nuclear Agency  
ATTN: RAEV  
ATTN: SPAS  
ATTN: SPTD  
ATTN: STRA  
ATTN: STSP  
4 cy ATTN: STTJ-CA

Defense Technical Information Center  
12 cy ATTN: DO

Field Command, DNA, Det 2  
Lawrence Livermore National Lab  
ATTN: FC-1

Field Command, DNA, Det 3  
Los Alamos National Lab  
ATTN: NS-635 FC-2

Field Command, Defense Nuclear Agency  
ATTN: PCT  
ATTN: PCTT  
ATTN: PCTT, M. Summa  
ATTN: PCTXE

Joint Chiefs of Staff  
ATTN: J-5 Nuclear Division/Strategy Div

Office of the Sec of Defense  
Net Assessments  
ATTN: Document Control

Under Secy of Def for Resch & Engrg  
ATTN: Offcen & Space Sys (OS)  
ATTN: Strat & Space Sys (OS)

### DEPARTMENT OF THE ARMY

Assistant Secretary of the Army  
Research, Development & Acquisition  
ATTN: Deputy Assistant Secretary, RAO

BMD Systems Command  
ATTN: BMDSC-HW, R. DeKalb  
ATTN: BMDSC-LEE, R. Webb

Dep Ch of Staff Ops & Plans  
ATTN: DAHD-MC, Nuc Chem Dir

Harry Diamond Laboratories  
ATTN: DELHD-MH-P, J. Swaltney, 20240  
ATTN: DELHD-TA-L, 81100, Tech Lib

US Army Materiel Command  
ATTN: ONCNC, Nuc-Chem Ofc

US Army Nuclear & Chemical Agency  
ATTN: Library  
ATTN: MONA-ME  
ATTN: MONA-ME, Maj Myers

### DEPARTMENT OF THE ARMY (Continued)

USA Engr Waterways Exper Station  
ATTN: B. Welch  
ATTN: K. Ingram

### DEPARTMENT OF THE NAVY

Assistant Secretary of the Navy  
Research Engineering & Systems  
ATTN: Dep Asst Sec, Res & Adv Tech

Naval Electronic Systems Command  
ATTN: PDE-110-K1, B. Kruger

Naval Plant Representative Office  
Strategic Systems Project Office  
ATTN: Doc Con Off for SPL325, M. Renner

Naval Surface Weapons Center  
ATTN: J. Forbes

Naval Surface Weapons Center  
ATTN: Tech Library & Info Svcs Br

Ofc of the Deputy Chief of Naval Ops  
ATTN: MOP 095, Ofc of Nav Warf

Strategic Systems Project Office  
ATTN: MSP-272  
ATTN: MSP-273  
ATTN: MSP-43, Tech Lib

### DEPARTMENT OF THE AIR FORCE

Air Force Systems Command  
ATTN: DLN

Air Force Weapons Laboratory  
ATTN: D. Cole  
ATTN: H. Bowley  
ATTN: NT  
2 cy ATTN: SUL

Ballistic Missile Office/DAA  
ATTN: EN  
ATTN: ENSN  
ATTN: MBEN, E. Furbee

Deputy Chief of Staff  
Research, Development, & Acq  
ATTN: AF/RDQI

### DEPARTMENT OF ENERGY

Department of Energy  
Office of Military Application  
GTR  
ATTN: ONA, DP-22

### OTHER GOVERNMENT AGENCY

Central Intelligence Agency  
2 cy ATTN: Tech Library

### DEPARTMENT OF ENERGY CONTRACTORS

University of California  
Lawrence Livermore National Lab  
ATTN: L-018, D. Nowak  
2 cy ATTN: Technical Info Dept Library

DEPARTMENT OF ENERGY CONTRACTORS (Continued)

Los Alamos National Laboratory

ATTN: D. Scammon  
ATTN: MS D406, D. Eilers, ESS  
ATTN: MS P218, D. Bergen  
ATTN: MS P669, M. Henderson, X-5  
ATTN: MS 948, A. Charnatz, MX-11  
2 cy ATTN: MS P364 Reports Library

Sandia National Laboratories

ATTN: Library & Security Classification Div

Sandia National Laboratories

ATTN: C. Smith  
ATTN: Org 7110, C. Broyles  
ATTN: Org 7112, A. Chabal  
ATTN: Org 7112, C. Mohl  
ATTN: Org 7112, J. Plimpton  
ATTN: Tech Lib 3241

DEPARTMENT OF DEFENSE CONTRACTORS

Aerospace Corp

ATTN: Library Acquisition M1/199  
ATTN: T. Digiacomo

Cushing Associates

ATTN: V. Cushing

General Research Corp

ATTN: E. Steele

JAYCOR

ATTN: R. Bonn

JAYCOR

ATTN: R. Poll

Kaman Sciences Corp

ATTN: F. Shelton  
ATTN: Library  
ATTN: W. Rich

Kaman Sciences Corp

ATTN: E. Conrad

Kaman Tempo

ATTN: DASIAC

Kaman Tempo

ATTN: DASIAC

Lockheed Missiles & Space Co., Inc

ATTN: L. Chase

Lockheed Missiles & Space Co., Inc

ATTN: J. Wilson  
ATTN: S. Taimuty, Dept. 81-74/154

Pacific-Sierra Research Corp

ATTN: F. Thomas  
ATTN: M. Brode, Chairman SAGE  
ATTN: L. Schlessinger

DEPARTMENT OF ENERGY CONTRACTORS (Continued)

Physics International Co

ATTN: D. Oliver  
ATTN: F. Davies

R&D Associates

ATTN: P. Field  
ATTN: J. Lewis  
ATTN: P. Haas  
ATTN: Technical Information Center

Rand Corp

ATTN: P. Davis

Rand Corp

ATTN: B. Bennett

S-CUBED

ATTN: C. Dismukes  
ATTN: C. Peterson  
ATTN: D. Grine  
ATTN: K. Pyatt  
ATTN: Library  
ATTN: P. Coleman

Science & Engrg Associates, Inc

ATTN: J. Cramer

Science & Engrg Associates, Inc

ATTN: J. Stockton

Science Applications Intl Corp

ATTN: K. Sites

Science Applications Intl Corp

ATTN: L. Scott

Science Applications Intl Corp

ATTN: W. Layson

SRI International

ATTN: A. Florence  
ATTN: D. Kaough  
ATTN: G. Abrahamson  
ATTN: J. Rosenberg  
ATTN: L. Schuer  
ATTN: T. Cooper

Tech Raps, Inc

ATTN: R. Holmes

TNM Electronics & Defense Sector

ATTN: M. King  
ATTN: M. Lipner  
ATTN: Technical Information Center

McDonnell Douglas Corp

ATTN: J. Kirby

University of New Mexico

ATTN: N. Baum



**END**

**FILMED**

**10-85**

**DTIC**